8-2015

A Magnetic Actuated Fully Insertable Robotic Camera System for Single Incision Laparoscopic Surgery

Xiaolong Liu
University of Tennessee - Knoxville, xliu57@vols.utk.edu

To the Graduate Council:

I am submitting herewith a dissertation written by Xiaolong Liu entitled "A Magnetic Actuated Fully Insertable Robotic Camera System for Single Incision Laparoscopic Surgery." I have examined the final electronic copy of this dissertation for form and content and recommend that it be accepted in partial fulfillment of the requirements for the degree of Doctor of Philosophy, with a major in Biomedical Engineering.

Jindong Tan, Major Professor

We have read this dissertation and recommend its acceptance:

William R. Hamel, Andy Sarles, Nicole McFarlane

Accepted for the Council:
Dixie L. Thompson

Vice Provost and Dean of the Graduate School

(Original signatures are on file with official student records.)

A Magnetic Actuated Fully Insertable Robotic Camera System for Single Incision Laparoscopic Surgery

A Dissertation Presented for the

Doctor of Philosophy

Degree

The University of Tennessee, Knoxville

Xiaolong Liu

August 2015

This dissertation is dedicated to my parents Ying Ma, and Qing Liu.

Acknowledgements

I would like to thank my advisor Dr. Jindong Tan for his support and guidance during the past five years. I appreciate his patience and tolerance that helped me to overcome difficulties in my research and my life.

I would like to thank Dr. William R. Hamel, Dr. Andy Sarles and Dr. Nicole McFarlane, who served as my committee members of dissertation defense.

I would like to thank all my labmates at Michigan Technological University, from 2010 to 2012: Dr. Shaolin Wang, Dr. Fanyu Kong, Dr. Shuo Huang, Dr. Sheng Hu, Dr. Lufeng Shi, Dr. Xinying Zheng, Dr. Ya Tian, Kuan Xing, and Jian Lu. I appreciate their help on my research.

I would like to thank my labmates at the University of Tennessee, Knoxville. Thanks for their support on my works and dissertation writing after I transferred from Michigan Technological University from 2012 to 2015: Dr. Jie Zhang, Dr. Binrui Wang, Dr. Heng Zhang, Dr. Hongsheng He, Dr. Zhenzhou Shao, Dr. Xi Chen, Ning Li, Yan Li, Reza Yazdanpanah, and Xiaodong Yang. Thanks also to Qin Zou, Dr. Yujia Bai, Kai Kang, Ran Huang, Gefei Kou, and Ran Duan for their encouragement and friendship.

Finally, I would like to specially thank to my family members for their support and love all the time.

Abstract

Minimally Invasive Surgery (MIS) is a common surgical procedure which makes tiny incisions in the patients anatomy, inserting surgical instruments and using laparoscopic cameras to guide the procedure. Compared with traditional open surgery, MIS allows surgeons to perform complex surgeries with reduced trauma to the muscles and soft tissues, less intraoperative hemorrhaging and postoperative pain, and faster recovery time. Surgeons rely heavily on laparoscopic cameras for hand-eye coordination and control during a procedure. However, the use of a standard laparoscopic camera, achieved by pushing long sticks into a dedicated small opening, involves multiple incisions for the surgical instruments. Recently, single incision laparoscopic surgery (SILS) and natural orifice translumenal endoscopic surgery (NOTES) have been introduced to reduce or even eliminate the number of incisions. However, the shared use of a single incision or a natural orifice for both surgical instruments and laparoscopic cameras further reduces dexterity in manipulating instruments and laparoscopic cameras with low efficient visual feedback.

In this dissertation, an innovative actuation mechanism design is proposed for laparoscopic cameras that can be navigated, anchored and orientated wirelessly with a single rigid body to improve surgical procedures, especially for SILS. This design eliminates the need for an articulated design and the integrated motors to significantly reduce the size of the camera. The design features a unified mechanism for anchoring, navigating, and rotating a fully insertable camera by externally generated rotational magnetic field. The key component and innovation of the robotic camera is the

magnetic driving unit, which is referred to as a rotor, driven externally by a specially designed magnetic stator. The rotor, with permanent magnets (PMs) embedded in a capsulated camera, can be magnetically coupled to a stator placed externally against or close to a dermal surface. The external stator, which consists of PMs and coils, generates 3D rotational magnetic field that thereby produces torque to rotate the rotor for desired camera orientation, and force to serve as an anchoring system that keeps the camera steady during a surgical procedure. Experimental assessments have been implemented to evaluate the performance of the camera system.

Table of Contents

List of Tables

List of Figures

Chapter 1

Introduction

1.1 Minimally Invasive Surgery

Minimally Invasive Surgery (MIS) involves making small incisions in the patients anatomy, inserting surgical instruments and laparoscopic cameras through the incisions, and using laparoscopic visual feedback to guide the procedure. It allows surgeons to perform complex surgeries with a few small incisions that reduce scarring, hospital stay duration, hemorrhaging, postoperative pain, recovery time and unnecessary muscle cuts Cleary and Peters (2010). Surgeons rely heavily on laparoscopic cameras for hand-eye coordination and control during a procedure. However, the use of a standard trocar endoscope camera, achieved by pushing long sticks into small openings, involves multiple incisions for the endoscope ports and surgical instruments, as illustrated in the left figure* of Fig. 1.1. Robotic systems such as the Intuitive Surgicals da Vinci system for laparoscopic procedures has been extremely successful in manifesting the flexibility of the surgical instruments yet still requires the multiple incisions of traditional laparoscopy. Recently, single incision laparoscopic surgery (SILS) and natural orifice translumenal endoscopic surgery (NOTES) have been introduced to reduce the number of, or even eliminate,

*http://www.endosurgery.org/technique.html

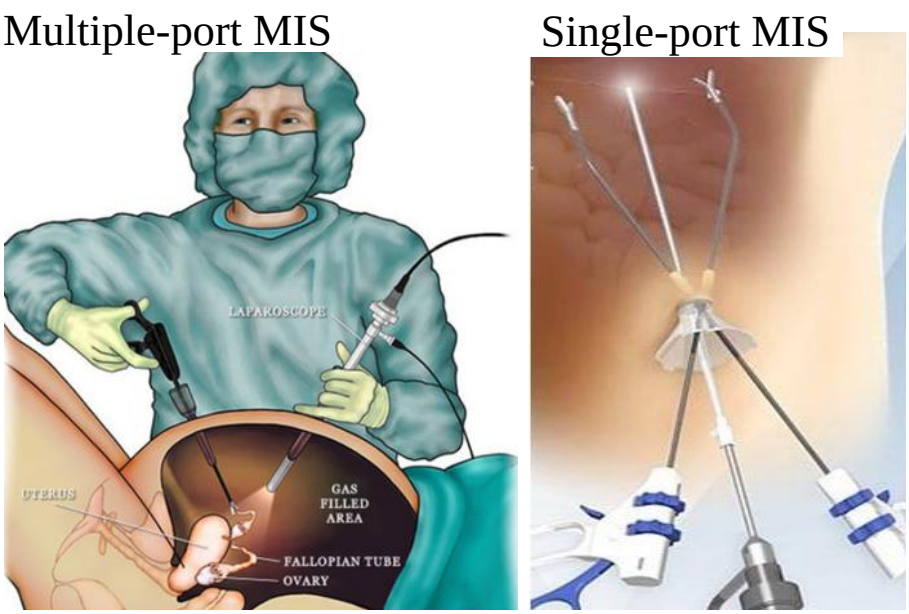

Figure 1.1: Multiple-port and single-port minimally invasive surgeries.

incisions Navarra et al. (2010), Saidy et al. (2012b), as shown in the right figure[†] of Fig. 1.1. The benefits of SILS or NOTES include less bleeding, less post-operative pain, faster incision recovery, and better cosmetic results compared with multiple-port surgeries Desai et al. (2009), Saidy et al. (2012a), Tracy et al. (2008). However, the shared use of a single incision or a natural orifice for both surgical instruments and laparoscopic cameras further reduces dexterity in manipulating instruments and laparoscopic cameras for better view angles.

1.2 Miniature Surgical Robots

Due to the limited surgical spaces inside human bodies, miniature laparoscopy and endoscopy surgical robots with various functions were developed to inspect abdominal cavities, and travel along GI tracts Moglia et al. (2009), Toennies et al. (2010), or be manipulated in fluid-filled lumens and/or soft tissues Nelson et al. (2010).

[†]http://www.gynaedurban.co.za/48-2/

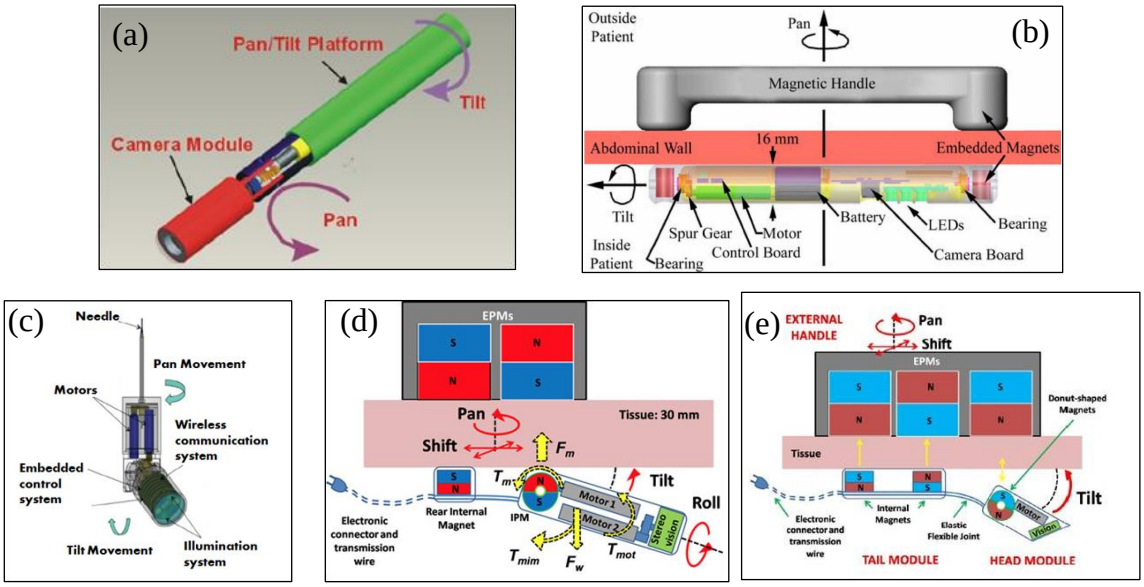

Figure 1.2: Laparoscopic cameras robots. (a) Hu et al. (2009); (b) Platt et al. (2009); (c) Castro et al. (2013); (d) Simi et al. (2013); (e) Simi et al. (2011).

1.2.1 Laparoscopic surgical camera robots

Insertable imaging robots with magnetic fixation and positioning for laparoscopic procedures have been reported in Cadeddu et al. (2009), Fakhry et al. (2009), Silvestri et al. (2013), Swain et al. (2010). In these solutions, the purposes of the on-board magnetic elements are intended for fixation, and manipulation of the device for positioning and orientation adjustments is normally achieved by manually maneuvering an external permanent magnet. To achieve greater accuracy and controllability of the imaging robots, researches have been done to manipulate the external permanent magnets with precisely controlled robot manipulators to overcome the exponential variability of magnetic fields. Research has also been done to integrate magnetic or electrical driven mechanism into the camera to manipulate the camera components Platt et al. (2009), Simi et al. (2011, 2013), as shown in Fig. 1.2(b), (d), and (e). The existing internal driven mechanisms usually consist of two articulated components, one providing fixation with the abdominal wall, and the other enabling manipulation of the camera module Castro et al. (2013), Hu et al.

(2009). Tethered multi-link robotic laparoscopic cameras as shown in Fig. 1.2(a) were proposed by Hu et al. (2009) which adopt on-board motors and peripheral mechanisms to actuate pan/tilt motion with camera bodies sutured against an abdominal wall for fixation.The camera design proposed in Castro et al. (2013) applied a wirelessly controlled motor-driven mechanism for pan/tilt motion with an on-board needle pierced through an abdominal wall for the camera fixation and electronics powering, as shown in Fig. 1.2(c). This articulated structure inevitably increases the size and complexity of the modules.

1.2.2 Endoscopic capsule robots

Researches have been intensively studied on swallowable medical robots, especially endoscopic robots to obtain visual feedbacks from GI tracts for disease inspects and diagnoses. Possible modules in a miniature surgical robot include vision, locomotion, localization, telemetry, and additional diagnostics, etc. One of the major research challenges to design such a robot is the development of its locomotion and localization modules, which actuate the robot to a desired surgical inspection target. To provide the surgical robots controllable motion, various solutions have been proposed which can be categorized into (1) internal locomotion; and (2) external locomotion.

The robot designs in Fig. 1.3(a)-(f) apply internal locomotion mechanisms that require on-board motors for actuation. A bidirectional legged locomotion mechanism with 12 legs was presented by Valdastri et al. (2009), as shown in Fig. 1.3(a). This design can uniformly distend tissue by using six-leg contacts, and is capable of traveling a colon in a time similar to conventional colonoscopy. To improve adhesion to an oesophageal wall, a similar design that applies bio-inspired feet was proposed by Glass et al. (2008), as shown in Fig. 1.3(b). Another locomotion mechanism that inspired by biology for a capsule robot was developed by Kim et al. (2005a,b) with two different prototypes shown in Fig. 1.3(c) and (d). The earthworm-like design propels itself by using extension/compression of Shape Memory Alloy (SMA)

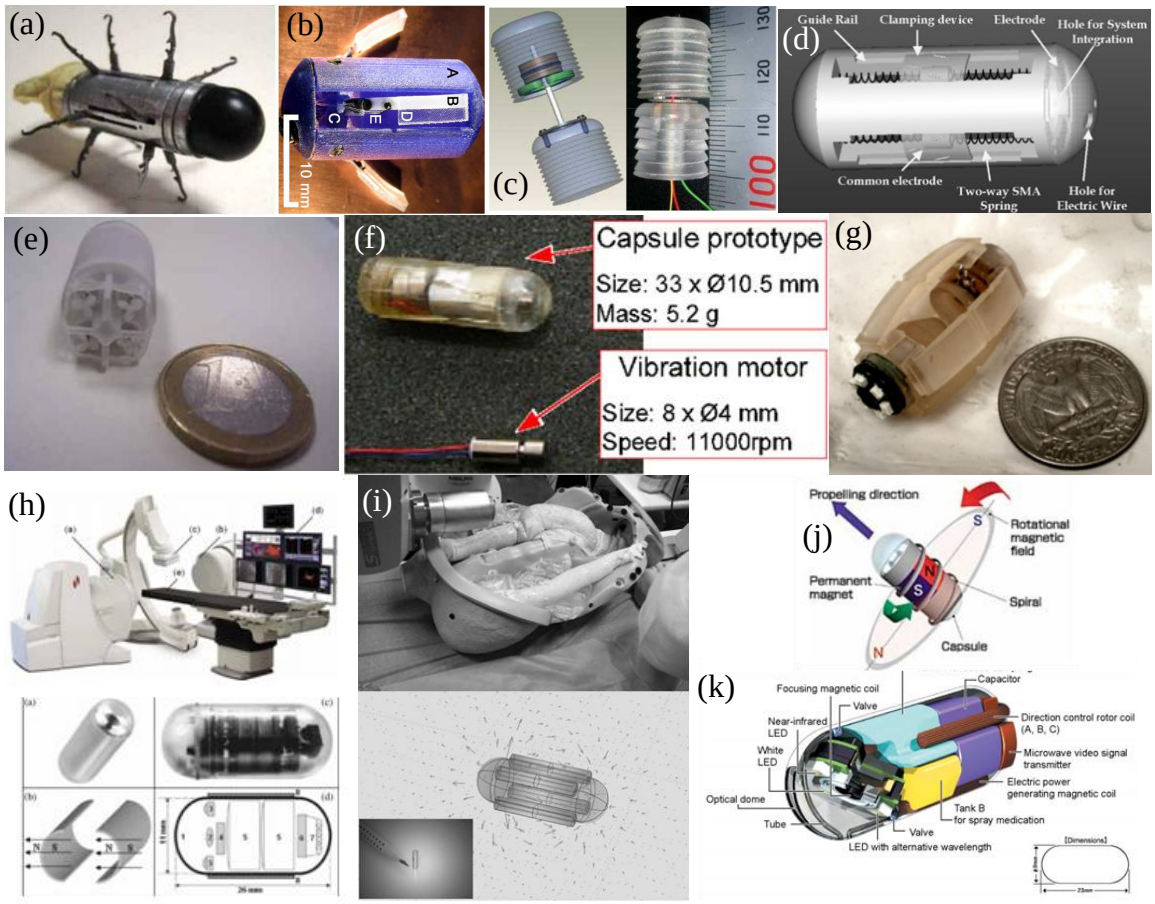

Figure 1.3: Endoscopy surgical robots. (a) Valdastri et al. (2009); (b) Glass et al. (2008); (c-d) Kim et al. (2005a,b); (e) Tortora et al. (2009); (f) Zabulis et al. (2008); (g) Yim and Sitti (2012); (h-i) Carpi and Pappone (2009), Ciuti et al. (2010); (j) Sendoh et al. (2003); (k) Uehara and Hoshina. (2003).

actuators. Micro needles were designed at both ends for anchoring to a surface. A propeller propulsion mechanism was developed by Tortora et al. (2009), as shown in Fig. 1.3(e) for actuating a capsule robot in GI environment filled with liquid. The submarine-like design can be actuated for various directions, speeds by its propellers that are controlled by a human interface. Zabulis et al. (2008) proposed a vibratory actuation mechanism shown in Fig. 1.3(f) , which consists of a micromotor and an assymetric mass, for a capsule robot to assist its traveling in GI tracts by decreasing friction with its surroundings.

The designs that applied external locomotion mechanisms are illustrated in Fig. 1.3(g)-(k). A drug-release robot shown in Fig. 1.3(g) was reported by Yim and Sitti (2012), in which the drug-release and locomotion mechanisms were designed by adopting a rolling cylinder EPM placed externally and a pair of axially magnetized IPMs inside the robot. The capsule robots with a magnetic shell and four internal permanent magnets (IPMs) shown in Fig. 1.3(h) and (i) were proposed by Carpi and Pappone (2009), Ciuti et al. (2010), which utilized a single cylindrical external permanent magnets (EPMs) mounted on a six-DOF robot arm to guide the robot to inspect GI tracts. Because of the low controllability by using EPMs, electromagnetic coils were applied to achieve flexible control of endoscopic robots. A three axis Helmholtz coils system was proposed to create rolling/rotating motions for a drug-release robot by Kim and Ishiyama (2014). An actuation mechanism of a capsule robot shown in Fig. 1.3(k) was achieved by wirelessly powering on-board motors and electronics with a coil vest by Uehara and Hoshina. (2003). A spiral structure warped capsule robot shown in Fig. 1.3(j) was proposed by Sendoh et al. (2003), which applied an externally rotational magnetic field to actuate the robot with an IPM on-board. A microrobot, which was made of permanent magnets for delicate retinal surgery, was designed to be actuated by eight electromagnetic coils for pose and force/torque control Kummer et al. (2010).

A major difference of the actuation requirements between a laparoscopic camera robot and an endoscopic camera robot is that the fixation function is trivial for an endoscopic camera robot. However, for a laparoscopic camera robot, the fixation and rotation functions have to work simultaneously to keep the camera being stably fixed in position when a rotational motion is actuated. Therefore, the locomotion mechanisms for endoscopic camera robots are limited to apply in a laparoscopic robot.

1.3 Research Goals

The two challenges in state-of-the-art systems are anchoring and manipulating (translational and rotational motion) the laparoscopic camera systems. Research efforts so far have addressed separate mechanisms for locomotion in the body cavity and pan/tilt of a laparoscopic camera, which results in bulky articulated systems and only limited degrees of freedom for locomotion and camera control. Therefore, there is a need to develop a unified fixation, translation, and rotation mechanism for autonomously controlling the locomotion of a fully insertable laparoscopic camera robot with high control accuracy.

The demands for multi-degrees of freedom (DOF) actuators or motors in robotics have motivated researchers to explore various mechanical design and actuation methods to enhance the system dynamic response and avoid singularities. Spherical induction motors were introduced in early in mid-1950s and ignite the interests of many researchers Chirikjian and Stein (1999), Liang et al. (2006), Lim et al. (2004), Rossini et al. (2011). Various forms of structural design have been conceived for multi-degrees of freedom and some have been prototyped. However, spherical motors have not been widely used in practical applications due to their constraints in the 3D workspace design of the stators and rotors and complexity of electromechanical analysis. Therefore, the implementation and control of spherical motors are usually confined to spherical step motors Chirikjian and Stein (1999), Liang et al. (2006), Lim et al. (2004), which affect their full potential as an isotropic real time control in 3D space. Additionally, the use of a spherical structure as a motor requires sophisticated bearing design for robotic systems. However, the application of such a concept to a wirelessly controlled laparoscopic camera system is an innovative design that could eventually break the barrier towards real applications of magnetically driven capsule cameras in minimally invasive surgery.

Motivated by various spherical motor concepts Chirikjian and Stein (1999), Liang et al. (2006), Lim et al. (2004), Rossini et al. (2011) and magnetic link designs for

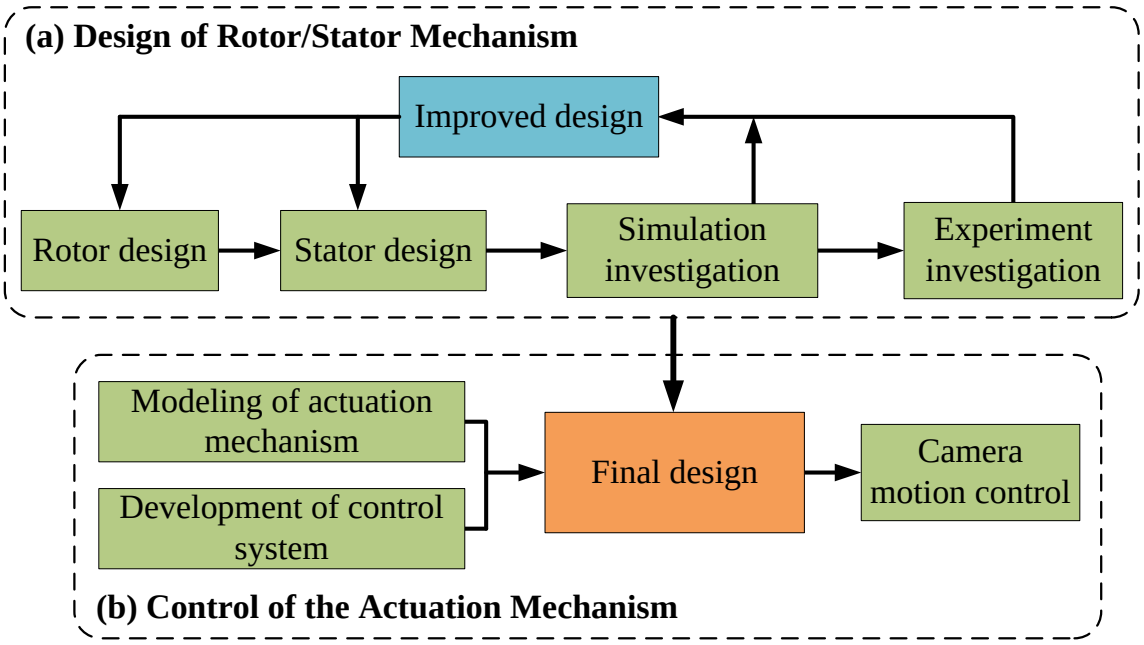

Figure 1.4: The research goals and the structure of this dissertation.

magnetically anchoring systems of endoscopic cameras Platt et al. (2009), Simi et al. (2011, 2013), Valdastri et al. (2010), **the objective of this research** is to develop an innovative actuation mechanism for wireless laparoscopic cameras that can be navigated, anchored and orientated wirelessly with a single rigid body to enhance and improve surgical procedures. The key component and innovation of the robotic camera is the magnetic driving unit, which is referred to as a rotor, driven externally by a specially designed magnetic stator. The rotor, consisting of magnets placed in the dome, can be magnetically coupled to a stator placed *ex vivo* against or close to the dermal surface. The *ex vivo* coils generate a 3D rotational magnetic field, thereby generating both torque to rotate the *in vivo* rotor in all three dimensions, and force to serve as an anchoring system that keeps the camera steady during a surgical procedure. The integration of the camera on-board electronics, such as an illumination and vision system, an inertial sensing system, a battery and battery management system, and a wireless communication system, is beyond the scope of this work.

Specifically, there are two main research goals achieved in this dissertation: first, the development of a reliable rotor/stator actuation mechanism for providing sufficient magnetic force and torque to anchor, translate, and rotate the camera; and second, the autonomous control of the developed actuation mechanism for the robotic camera with high accuracy.

The first goal can be achieved by following the design pipeline as shown in Fig. 1.4(a) and discussed in Chapters 2, 3, 4. Starting from a semi-spherical rotor/stator conceptual design, the locomotion capabilities are evaluated by simulation and experimental studies. Based on the design investigation results, improved designs of the rotor and the stator are proposed to enhance the camera locomotion capabilities.

The second goal can be achieved by developing the control model and control system of the final design, as shown in Fig. 1.4(b) and discussed in Chapters 5.

1.4 Research Challenges

The research challenges to develop the unified locomotion mechanism for a wireless laparoscopic camera robot are (1) design and analysis of the rotor and stator; and (2) the camera motion control by using the designed locomotion mechanism.

Design and analysis of the rotor and stator

To provide reliable manipulation of the camera by the external rotation magnetic field from the stator, the magnetic coupling between the rotor and stator should be capable of generating sufficient force and torque for the translation and rotation of the camera. Compared with a spherical actuator, the air gap between the rotor and the stator is much larger in the surgical situation due to a patient's abdominal wall thickness, which normally ranges is 20 mm $\sim$ 40 mm Song et al. (2006). The magnetic force and torque will rapidly reduce while the distance from the rotor to the stator increases. Therefore, the design and analysis of the magnetic driving unit and

the externally positioned stator will be thoroughly studied in this work for reliable actuation of the camera.

Motion control of the robotic camera

Once the laparoscopic camera is inserted into the body cavity, the camera is first manipulated to focus on the operative area. At this stage, we assume that the attractive force between the rotor and the stator is strong enough such that the rotor is pushed against the abdominal wall. The camera system can also be controlled such that the camera is floating in the gas filled body cavity, which requires accurate compensation of gravity by the external magnetic field and estimation of the camera locations. It becomes difficult for the camera system with limited sensing capability. In this work, a contact based control model will be adopted.

The tissue pressure on the rotor is a result of the balanced gravity and magnetic attractive forces to the rotor. The membrane forces are determined by a viscoelastic model consisting of the tissue stiffness and the viscous damping. Considering the variation in the thickness of the abdominal wall, the external magnetic forces should balance the camera gravity but cause little undesired internal pressure to the surrounding tissue. The membrane force is associated with deflection of the tissue, which is an exponential function of the depth of the deflection. With the design of the rotor, the membrane force can be integrated over the depth of the deflection.

In this work, the control model of the camera will be developed according to the force and torque analysis between the camera body and an abdominal wall tissue, in order to realize automatic motion control of the camera.

1.5 Contributions

The major contributions of my research presented in this dissertation are listed as follows.

1. An innovative magnetic actuated insertable robotic camera system was developed for SILS with a line-arranged rotor and a hybrid stator as the final design. The successful final design was invented based on two generation prototypes which are a semi-spherical driving unit and a line-arranged driving unit with pure coil stators. The final design features a reliable unified fixation, translation and rotation control of the capsulated dummy laparoscopic camera.

2. An closed-loop control system was designed and implemented which can automatically actuate the orientation of the camera with less than 1° control accuracy under an abdominal wall with a normal range thickness.

3. A novel abdominal wall thickness sensing system was proposed and implemented inside the hybrid stator. The sensing system, which consists of four-group tri-axis hall effect sensors, can provide sub-millimeter sensing accuracy in real time. With sensed abdominal wall thicknesses, the stator can thus generate appropriate rotational magnetic field for the camera motion control.

1.6 Dissertation Outline

This dissertation consists of four main chapters that are organized as follows:

Chapter 2 introduces a semi-spherical magnetic driving unit head for the camera locomotion. The proposed camera has two semi-spherical domes, one for housing the illumination and the camera module; the other for housing the small cylindrical magnets which serve as the driving unit in the camera system. The stator consists of multiple coils which are distributed around a virtual dome to simulate part of a stator of a spherical motor. The adjustable currents in the coils provide attracting force and rotating torque to fixate and manipulate the camera.

Chapter 3 introduces an improve line-arranged driving unit design based on the design in Chapter 2. A locomotion mechanism was proposed which consists of a flat-arranged stator with 17 iron-core coils and a line-arranged rotor with 3 cylindrical permanent magnets inside the camera. The motor-free design unifies the camera's fixation and manipulation by adjusting input currents in the stator which generates 3D rotational magnetic fields, and decouples the camera's locomotion into pan motion and tilt motion.

Chapter 4 introduces an improved hybrid stator design to enhance the locomotion capabilities of the mechanism developed in Chapter 3. This design features a unified mechanism for anchoring, navigating, and rotating a fully insertable camera by externally generated rotational magnetic field. The insertable camera body, which has no active locomotion mechanism on-board, is capsulated in a one-piece housing with two ring-shaped tail-end magnets and one cylindrical central magnet embedded on-board as a rotor. The stator positioned outside an abdominal cavity consists of both permanent magnets and electromagnetic coils for generating reliable rotational magnetic field. The prototype investigation was also demonstrated in this chapter.

Chapter 5 demonstrates a two-degree-of-freedom (2-DOF) orientation control of a magnetic actuated robotic surgical camera system for single incision laparoscopic surgery. The development of the control system is based on the successful design in Chapter 4. A closed-loop control system was developed to enable automatic fine orientation control (tilt motion and pan motion) of the camera. The experimental investigations were conducted to assess the control accuracy in tilt and pan motions respectively of the camera system. The combined orientation control in three-dimensional space was also evaluated by experiments.

At last, Chapter 6 concludes the dissertation and discusses the future work.

Chapter 2

Semi-spherical Rotor/Stator Driving Unit Design

2.1 Abstract

This chapter introduces an initial prototype of a unified active locomotion mechanism for a capsule-shaped laparoscopic surgical camera system. The proposed design integrates the camera's fixation and manipulation together by adjusting a 3D rotational magnetic field from a stator outside a patient's body. The stator generates both torque to rotate the inside rotor dome in all three dimensions, and force to serve as an anchoring system that keeps the camera steady during a surgical procedure. This design eliminates the need for an articulated design and therefore the integrated motors to significantly reduce the size of the camera. A set of stator and rotor designs are developed and evaluated by simulations and experiments.

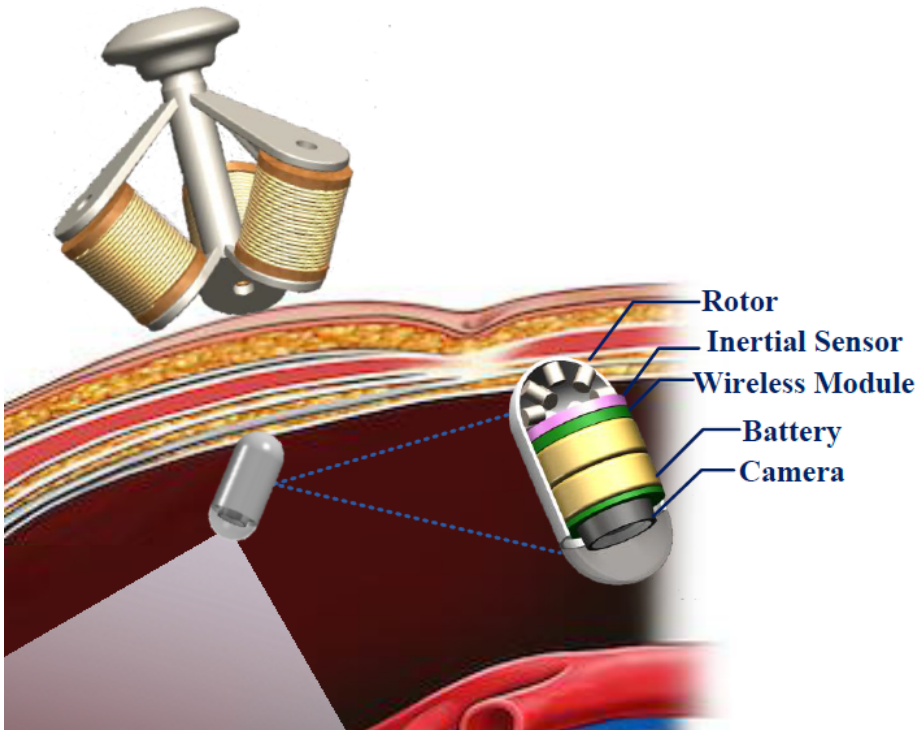

Figure 2.1: Concept of the capsule-shaped laparoscopic camera system.

2.2 Conceptual Design

A novel motor-free unified active locomotion mechanism is proposed for a laparoscopic camera, as shown in Fig. 2.1. Similar to a rotor in a spherical actuator, a set of magnets arranged at the semi-spherical dome can be magnetically coupled to a stator placed outside patient's body against or close to the dermal surface. The coils generate a 3D rotational magnetic field, thereby generating both torque to rotate the inside rotor dome in all three dimensions, and force to serve as an anchoring system that keeps the camera steady during a surgical procedure. This design eliminates the need for an articulated design and therefore the integrated motors to significantly reduce the size of the camera. This design enables the unified translational and rotation controls with the external device.

However, different from a spherical actuator, the distance from the camera's rotor to a stator is much longer in the surgical situation due to the thickness of patient's

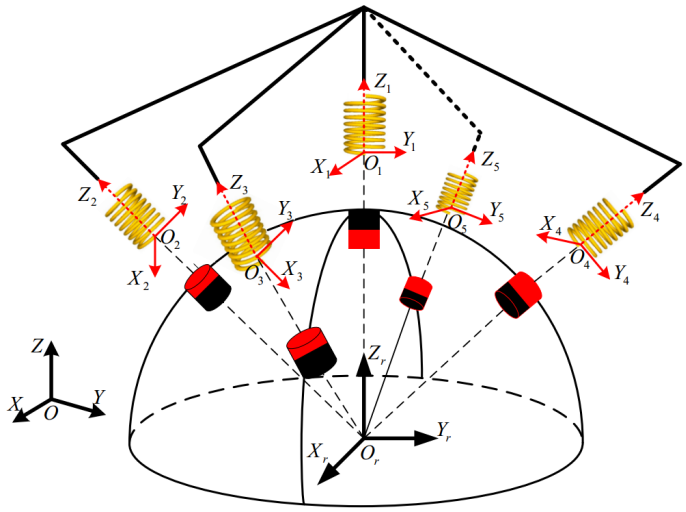

Figure 2.2: The working principle of the spherical motor inspired locomotion mechanism.

abdominal wall. The magnetic force and torque will rapidly reduce while the distance from a rotor to a stator increases. Only improving the input currents cannot solve this problem because of the limited power supply and coils's overheating. In order to address the problems mentioned above, a set of rotor and stator designs are proposed and evaluated in this paper for achieving a reliable laparoscopic camera system.

The laparoscopic camera system consists of two parts: a rotor embedded capsule-shaped camera and a coil winding stator. The camera consists of five main components, as shown in Fig. 2.1: a semi-spherical magnetic head for locomotion, an illumination and a camera module for visualization, a battery and a battery management module for power supply, a wireless communication module for data transmission, and an inertial sensing module for controlling. Our proposed camera has two semi-spherical domes, one for housing the illumination and the camera module; the other for housing the small cylindrical magnets which serve as the driving unit in the camera system. The stator consists of multiple coils which are distributed around a virtual dome to simulate part of a stator in a spherical motor. The adjustable currents in the coils provide attracting force and rotating torque to fixate and manipulate the camera.

The working principle of the proposed design can be illustrated in Fig. 2.2. The system is designed to enable two types of motions for the camera system, translational control and orientation control, in addition to the compensation of the gravity of the camera. The singularityless orientation control requires torque along three axes of camera system, and the translation control requires forces along three axes, with the force along z axis providing the fixation of the camera against an abdominal wall. By varying the input currents of all coils which coordinate at $\Sigma_j = \{X_j, Y_j, Z_j\}$, any desirable rotation can be achieved by the generated rotational magnetic field. The translational control is provided by moving the passive fixture along the dermal surface with attractive forces between the permanent magnets and coils. To simplify the analysis of our proposed designs, Σ_r and Σ_j are all referred to a common reference frame $\Sigma = \{X, Y, Z\}$ by assuming Σ 's origin O locates at O_r.

2.3 Stator Designs

The number of the coils in a stator should be at least four because of the camera's three degrees of freedom orientation mobility (1 for camera fixation in Z direction, 3 for camera orientation). But in fact, the rotation around capsule's long axis is not as important as the other two rotations due to the camera's symmetry structure along its long axis. Therefore, the coil's number of a stator can be extended to 3.

Considering a proper size of the stator, the designs consist of 3, 4, and 5 coils respectively as shown in Fig. 2.3 (a), (c), (d). To simplify the stator designs, all the coils share the same dimension: an outer radius R, an inner radius r, a height h and a tilt angle ψ. Taking the 3 coil stator as an example, the initial setting assumes all the coils are tangent to each other in the XY plane with $\psi = 0$, as shown in Fig. 2.3(a). The ψ rotating axises are fixed at the bottoms of the coils. To calculate ψ, the coil to rotor distance d has to be determined. According to the reference Song et al. (2006), the average thickness of the abdominal wall is about 30 mm. For compensating a tilted depth of the stator, d is set as 40 mm. As illustrated in Fig. 2.3

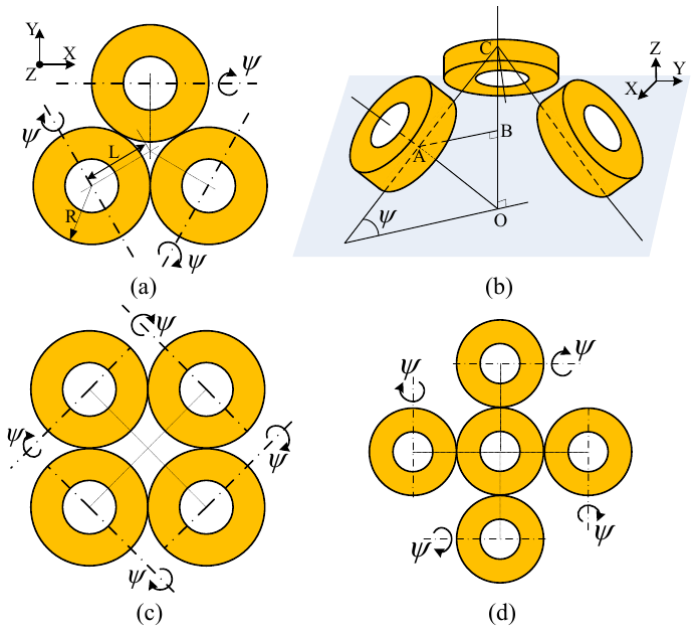

Figure 2.3: Three stator designs.

(b) where $OA = d$, $AB = L$, ψ can be calculated by $\arcsin(L/d)$. Considering the weak magnetic flux density generated by air-core coils, soft iron rods are inserted in the coils for producing stronger magnetic field. Similar calculations are applied to 4 and 5 coils stators in Fig. 2.3(c) and (d). In the 5 coil stator design, there is no tilt angle on the central coil.

2.4 Rotor Designs

For designing the rotor, a set of axially magnetized cylinder magnets are embedded in the semi-spherical dome of the camera. In this paper, four rotor designs are proposed as shown in Fig. 2.4. The red magnets represent the north poles pointing outside or upside while the blue ones point to the opposite ways. The rotor designs 1 and 4 in Fig. 2.4(a), (d) both include a disc magnet. It is worth noting that a disc magnet and a cylinder magnet can both be considered as a magnetic dipole in the far field. This fact will be used for developing the analytical model of the locomotion mechanism in Section 2.6. The rotor 1 in Fig. 2.4(a) consists of 12 small cylinder magnets that are

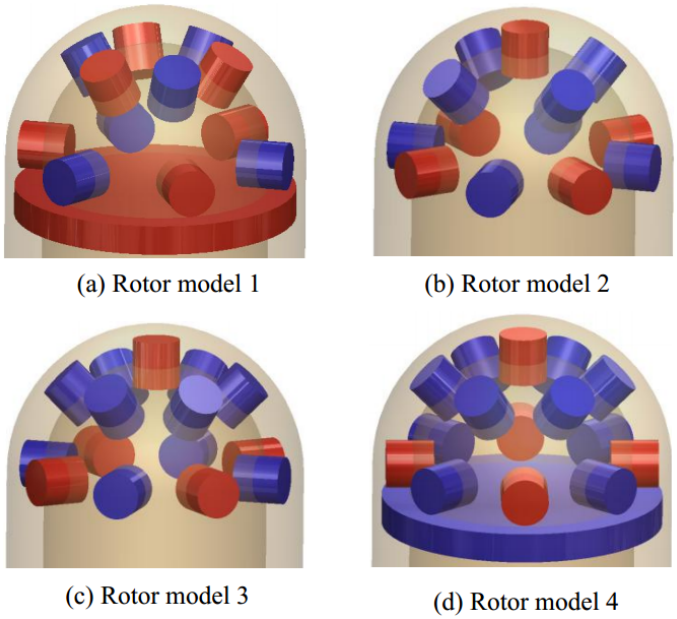

Figure 2.4: Four rotor designs.

mounted along the equator at the longitude of every 60°, along the latitude of 60° at the longitude of every 60°. The rotor 2 in Fig. 2.4(b) consists of 13 small cylinder magnets which are mounted along the equator at the longitude of every 45°, along the latitude of 45° at the longitude of every 90°, and one on the north pole. The rotor 3 shown in Fig. 2.4(c) is similar to model 2 with the only difference that the magnets are mounted along the latitude of 45° at the longitude of every 45°. The rotor 4 adds a disc magnet based on the rotor 3.

2.5 Design Parameters

The purpose of proposing different designs aims at seeking reasonable designs and parameters for a reliable camera locomotion mechanism. Therefore, a set of parameters of the stator and the rotor have to be specified. The outer radius R of the coils ranges from 8 mm to 30 mm, the inner radius and coil height are fixed at 5 mm and 30 mm respectively. The reason for fixing the inner radius and coil height is because changing the two parameters will not significantly affect the generated

force and torque compared with the outer radius R according to our preliminary experiments. Considering the dimension of the camera whose dome has a 8 mm inner radius and commercially available cylinder magnets. The radius and height of a cylinder magnet are selected as 1.27 mm and 2.54 mm separately with residual magnetization as 1.32 Tesla. The disc magnet is chosen as 1.59 mm height and 8 mm radius with its residual magnetization as 1.43 Tesla.

The current density in the coils has a major impact on the generated force and torque. The maximum current carrying capacity of a coil is determined by a copper wire's cross sectional area. In this paper, we select copper wire's with a cross sectional area as 1 mm^2. In terms of experiential data, a 1 mm^2 copper wire can carry less than 8 A for long-time duty and less than 16 A for short-time duty. The current carrying capacity also depends on insulation materials and cooling conditions. For testing our designs, we safely assume the maximum current carrying capacity $|I_{max}|$ is 5 A.

2.6 Modeling of Actuation Mechanism

The objective of building the analytical model of the camera system's locomotion mechanism is twofold: to realize real-time dynamic control of the laparoscopic camera; and to analyze the control capabilities of the rotor and stator designs. In this paper, we focus on evaluating the control capabilities of our proposed designs based on the analytical model. The major problem of developing the analytical model is the calculation of the force and torque generated on the rotor. The techniques applied to spherical motors for deriving their dynamic analytical model are all based on Lorentz law due to the air-core coils Rossini et al. (2013), Wang et al. (2003), Liang et al. (2006). However, in our application the thickness of the abdominal wall is much greater than the air gap in the spherical motors. Compared with air-core coils, iron-core coils can provide stronger magnetic field because of the high magnetic permeability of soft iron. In this paper, both air-core and iron-core coils will be

considered. The Lorentz force law can not develop the analytical model for iron-core coils. Considering the shapes of the cylinder/disc magnets in the semi-spherical dome of the camera, the magnetic moment of each magnet can be described as $\mathbf{M}$. The force and torque applied on a magnet with its magnetic moment $\mathbf{M}$ can be represented by

$$\mathbf{T} = \mathbf{M} \times \mathbf{B}, \tag{2.1}$$

$$\mathbf{F} = (\mathbf{M} \cdot \nabla)\mathbf{B}, \tag{2.2}$$

where $\mathbf{B}$ is the magnetic flux density at the location of $\mathbf{M}$ Jackson (1999). To analyze the generated force and torque, the rotor's magnetic moment $\mathbf{M}$ and the stator's magnetic flux density $\mathbf{B}$ have to be calculated.

2.6.1 Stator's Magnetic Flux Density B

For modeling the stator's magnetic flux density, a set of local coordinate systems of the coils are set as $\Sigma_1 = \{X_1, Y_1, Z_1\}$, $\Sigma_2 = \{X_2, Y_2, Z_2\}$, ..., $\Sigma_N = \{X_N, Y_N, Z_N\}$ where N is the number of the coils. $\mathbf{M}$ and $\mathbf{B}$ in (2.1) and (2.2) share the same coordinate system. A coordinate frame $\Sigma = \{X, Y, Z\}$ is adopted for establishing the relationship between the stator's coordinates and rotor's coordinates. The transformation from local coil coordinates $\Sigma_j = \{X_j, Y_j, Z_j\}$ to the reference coordinates $\Sigma = \{X, Y, Z\}$ can be expressed as

$$\mathbf{P}_j = \mathbf{R}_j \mathbf{P} + \mathbf{T}_j, \tag{2.3}$$

where $\mathbf{P} = (x, y, z)^T$ and $\mathbf{P}_j = (x_j, y_j, z_j)^T$ are the same point in different coordinates Σ and Σ_j, and $j = 1, ..., N$. $\mathbf{R}_j \in \mathbb{R}^{3\times3}$ and $\mathbf{T}_j \in \mathbb{R}^{3\times1}$ are the rotational matrix and translational vector from Σ_j to Σ respectively.

The magnetic flux density at a point in space can be superimposed from each coil in Σ

$$\mathbf{B}(x, y, z) = \sum_{j=1}^{N} \mathbf{R}_j^T \mathbf{B}_j(x_j, y_j, z_j), \tag{2.4}$$

where $\mathbf{B}_j$ is the coil's magnetic flux density in its local coordinates. Considering we have an air-core and an iron-core for the coils, it is preferred to have a common representation of the coil's magnetic flux density. Finite Element Method (FEM) is able to obtain accurate solutions of the coil's magnetic flux density by building extra fine meshes. However, the expensive computational time of FEM fails itself to serve in a real time application. A magnetic dipole model fitting method proposed in Kummer et al. (2010), which adopts the coil's axial magnetic flux density simulation results from Finite Element Method as the fitting data, is applied for estimating the parameter p and l in

$$\mathbf{B}_j(\mathbf{P}_j) = \frac{\mu_0}{4\pi}\left(-\frac{\mathbf{M}}{|\mathbf{P}_j|^3} + \frac{3(\mathbf{M}\cdot\mathbf{P}_j)\mathbf{P}_j}{|\mathbf{P}_j|^5}\right), \tag{2.5}$$

where $\mathbf{M} = p\mathbf{l}$ is the coil's equivalent magnetic moment. It has been verified in Kummer et al. (2010) the magnetic flux density $\mathbf{B}_j$ has a linear relationship with input current I_j. Thus, (3.3) can be reformulated as

$$\mathbf{B}(x, y, z) = \sum_{j=1}^{N} \mathbf{R}_j^T \mathbf{B}_j^u(x_j, y_j, z_j) I_j, \tag{2.6}$$

$\mathbf{B}_j^u$ is the unit magnetic flux density of coil j.

2.6.2 Rotor's Magnetic Moment M

The complex structures of the rotor designs make it difficult to express the rotor's magnetic moment in one piece. Because the forces and torques applied on each individual magnet can be superimposed in a linear way, a strategy for expressing the rotor's magnetic moment is to establish the relationship between each magnet's magnetic moment and the magnetic flux density generated from each coil.

In the rotor's local coordinates $\Sigma_r = \{X_r, Y_r, Z_r\}$, the cylindrical magnets are distributed around the semi-spherical dome, as shown in Fig. 2.2. The orientations

and positions of the magnets in Σ_r are denoted as $\mathbf{R}_i^m$ and $\mathbf{T}_i^m$, $i = 1, ..., n$, n is the number of the cylindrical magnets. The magnetic moment of the ith magnet in Σ_r is expressed as

$$\mathbf{M}_i^r = m_i \cdot \mathbf{d}_i, \tag{2.7}$$

where the value of the magnetic moment m_i can be calculated by

$$m_i = \frac{1}{4} M_0 \pi D_i^2 L_i, \tag{2.8}$$

M_0 is the residual magnetization of the cylinder magnet; D_i and L_i are the diameter and height of the ith cylinder Wang and Meng (2006). $\mathbf{d}_i$ is the magnet's orientation which is calculated by $\mathbf{d}_i = \mathbf{R}_i^m(0, 0, 1)^T$. Due to the rotor's rotational motion characterized by a rotational matrix $\mathbf{R}$ in the reference coordinates Σ, the transformation from Σ_r to Σ is represented by

$$\mathbf{P}_r = \mathbf{R}\mathbf{P} + \mathbf{T}, \tag{2.9}$$

where $\mathbf{P}_r$ denotes a point in Σ_r. $\mathbf{R} \in \mathbb{R}^{3\times3}$ and $\mathbf{T} \in \mathbb{R}^{3\times1}$ are the rotation matrix and the translation vector from Σ_r to Σ. With (2.9) and (2.3), the transformation is established between the rotor and stator by

$$\mathbf{P}_j = (\mathbf{R}_j\mathbf{R}^T)(\mathbf{P}_r - \mathbf{T}) + \mathbf{T}_j, \tag{2.10}$$

which is used to represent $\mathbf{M}$ and $\mathbf{B}$ in a common coordinates in order to calculate the force and torque in (2.1) and (2.2).

2.6.3 Force and Torque Calculation

Because magnetic forces contribute part of magnetic torques, shifting the magnet's rotational centers to the semi-spherical rotor's center is necessary for superimposing

the force-contributed torques generated on different magnets. According to what we have discussed in Section 2.6.1, 2.6.2 and (2.1)-(2.2), the force and torque generated on the rotor from a single unit-current coil j are formulated as

$$\mathbf{F}_j^u = \sum_{i=1}^{n} (\mathbf{M}_i^j \cdot \nabla)\mathbf{B}_j^u, \tag{2.11}$$

$$\mathbf{T}_j^u = \sum_{i=1}^{n} [\mathbf{M}_i^j \times \mathbf{B}_j^u + \mathbf{L}_i \times (\mathbf{M}_i^j \cdot \nabla)\mathbf{B}_j^u]. \tag{2.12}$$

where $\mathbf{L}_i$ is the ith magnet's lever arm; $\mathbf{M}_i^j$ is the ith magnetic moment represented in Σ_j and calculated by

$$\mathbf{M}_i^j = (\mathbf{R}_j \mathbf{R}^T) \cdot \mathbf{M}_i^r. \tag{2.13}$$

To develop the complete force and torque models, $\mathbf{F}_j^u$ and $\mathbf{T}_j^u$ have to be transformed in Σ. Denoting the input current as $\mathbf{I} = (I_1, I_2, ..., I_N)^T$, the final expression of electromagnetic force and torque in Σ can thus be formulated as

$$\mathbf{F} = \sum_{j=1}^{N} \mathbf{R}_j^T \mathbf{F}_j^u I_j, \tag{2.14}$$

$$\mathbf{T} = \sum_{j=1}^{N} \mathbf{R}_j^T \mathbf{T}_j^u I_j. \tag{2.15}$$

Considering the force analysis of the laparoscopic camera inside a patient's abdominal cavity, the forces applied on the camera can be categorized as the electromagnetic force $\mathbf{F}$, the membrane force $\mathbf{f}_m$ from the squeezed abdominal cavity wall tissue, the liquid friction force $\mathbf{f}_l$ while the camera is transitioning and rotating, and the camera's gravity force $m\mathbf{g}$. The electromagnetic force $\mathbf{F}$ will balance all the other forces. Assume $\mathbf{p}$ is the camera's location in Σ. According to Newton's law, the dynamic model of the camera can thus be expressed as

$$m\ddot{\mathbf{p}} = \mathbf{F} - \mathbf{f}_l - \mathbf{f}_m - m\mathbf{g}. \tag{2.16}$$

It is important to note that in (2.16) the Z component of the electromagnetic force f_z will lead to the tissue deformation and subsequently changes $\mathbf{f}_l$ and $\mathbf{f}_m$. To maximally eliminate the torques generated from $\mathbf{f}_l$ and $\mathbf{f}_m$ when the camera is steering, one control strategy to deal with this problem is that before manipulating the camera, reduce f_z for alleviating the effects of $\mathbf{f}_l$ and $\mathbf{f}_m$ on the camera. After actuating, increase f_z for applying the torques generated from $\mathbf{f}_l$ and $\mathbf{f}_m$ to balance the torque from the camera's gravity.

2.7 Experiment Validation

In this section, the prototype designs of our proposed laparoscopic camera system are fabricated and evaluated based on the developed analytical model of the locomotion mechanism. To analyze the analytical model of stator's magnetic flux density, the data from a FEM software is adopted as benchmarks. The maximum output forces and torques of different designs are compared in accordance with analytical solutions. At last, the generated forces and torques of the fabricated stator and rotor are tested by real force/torque sensors.

2.7.1 Simulation Results

Stator's Magnetic Flux Density Evaluation

For evaluating the analytical model of the iron-core stator's magnetic flux density developed in Section 2.6.1, a set of simulation data obtained from COMSOL Multiphysics 4.3a (COMSOL Inc., Sweden) are used to compare with our analytical results. As shown in Fig. 2.5 and 2.6, the analytical magnetic flux density of the stator is estimated by FEM. The parameters p and l for the magnetic dipole model in (2.5) are calculated as $p = 2.98\,\mathrm{Am}^2$ and $l = 0.44\,\mathrm{m}$. The origin of the stator coordinates $\Sigma_s = \{X_s, Y_s, Z_s\}$ is located at the geometric center of the three origins of coil coordinates. The direction Z_s is determined by summing the vectors $\mathbf{Z}_1$, $\mathbf{Z}_2$,

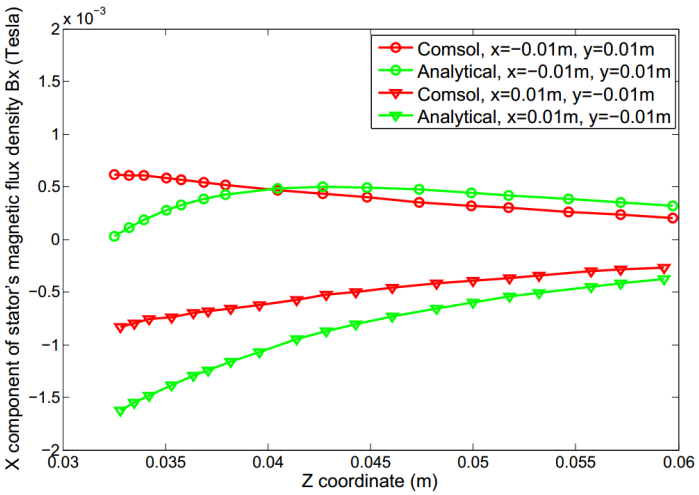

Figure 2.5: B_x component magnetic flux density.

and $\mathbf{Z}_3$ in Σ. Fig. 2.5 and 2.6 show the comparison results of B_x and B_z in the working region which is along negative Z_s direction ranging from 0.03 m to 0.05 m with two sets of x-y coordinates $\{x_s = 0.01\,\text{m}, y_s = -0.01\,\text{m}\}$ and $\{x_s = -0.01\,\text{m}, y_s = 0.01\,\text{m}\}$. Due to the stator's symmetric structure, B_y can be referred to B_x. As illustrated in Fig. 2.6, B_z has a major contribution to the generated force and torque because of being much greater than B_x.

Stator's Design Evaluation

Table 2.1, 2.2 and 2.3 show the three stator models' evaluation results based on the rotor 1. The maximum force and torque components in x, y, z directions are evaluated under the input current $-5\,\text{A} \sim 5\,\text{A}$. With a fixed rotor to coil distance as $d = 40\,\text{mm}$, we test the coil radius 10 mm, 20 mm, 30 mm on the 3 coil stator, 10 mm, 20 mm, 25 mm on the 4 coil stator, and 8 mm, 10 mm, 15 mm on the 5 coil stator. The reason for not applying the same set of radius on all the stator models is because a large radius R for 4 and 5 coil stator will lead ψ to approach to 90°. It is shown in Table 2.1, 2.2 and 2.3 that an iron-core stator can generate much greater force and torque than an air-core stator under the same set of design parameters. To clarify the evaluation results, the iron-core experimental results are visualized as shown in

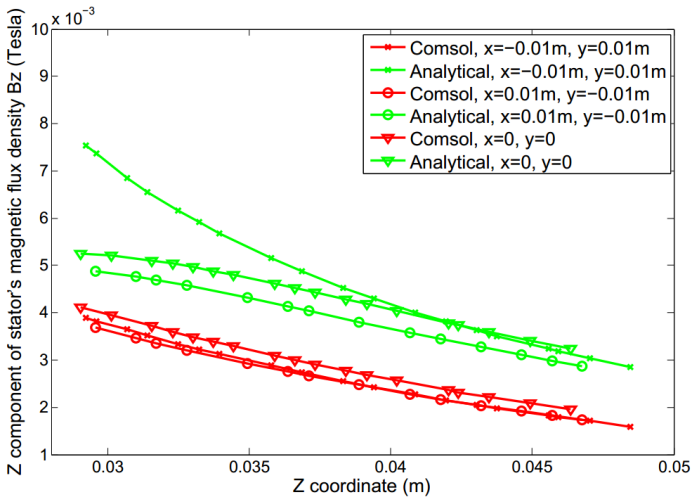

Figure 2.6: B_z component magnetic flux density

Fig. 2.7. The maximum force and torque in x and y directions increases as the outer radius R and tilt angle ψ increases. But the force component in z direction decreases after the tilt angle ψ is over 45°. The 5 coil stator is a special case which shows that $\psi = 48.6°$ still keeps a growing trend of F_{zmax} value due to the effect of central coil. The torque values T_z along the camera's axis have a e^{-18} scale which means the camera cannot be rotated around its Z_r axis. This fact is actually reasonable because in a real application the camera will not be required to rotate around its own Z_r axis.

Comparing the three models in Table 2.1, 2.2 and 2.3, the 3 coils iron-core stator with $R = 20\,\text{mm}$ and the 4 coils iron-core stator with $R = 20\,\text{mm}, 25\,\text{mm}$ provide reasonable forces and torques in all x, y, and z directions. In a real surgery situation, a small tilt angle ψ design is preferred because a larger ψ leads to a greater distance from the rotor to the stator. Therefore, the 3 coil stator with $R = 20\,\text{mm}$ is selected as the candidate design and used in the rotor models evaluation due to its good balance of coil tilt angle ψ and generated forces and torques.

Rotor's Design Evaluation

Table 2.4 shows the evaluation results of four rotor designs based on the 3 coil iron-core stator with $R = 20\,\text{mm}$. The rotor 1 and 4 generate greater forces and torques

Table 2.1: 3 Coil Stator Models Evaluation Based on Rotor 1 Configuration

Core Type	$R\ (mm)$	$\psi\ (°)$	$F_{xmax}\ (N)$	$F_{ymax}\ (N)$	$F_{zmax}\ (N)$	$T_{xmax}\ (Nm)$	$T_{ymax}\ (Nm)$	$T_{zmax}\ (Nm)$
Air Core	10	16.8	0.0023	0.0020	0.0073	4.08e-5	4.71e-5	2.03e-20
	20	35.3	0.0374	0.0324	0.0395	7.79e-4	8.99e-4	1.38e-19
	30	60	0.0991	0.0858	0.0286	3.40e-3	3.90e-3	2.72e-15
Iron Core	10	16.8	0.0318	0.0275	0.1004	5.65e-4	6.52e-4	2.68e-19
	20	35.3	0.1983	0.1718	0.2099	4.10e-3	4.80e-3	8.40e-19
	30	60	0.3441	0.2980	0.0993	1.17e-2	1.35e-2	3.71e-18

Table 2.2: 4 Coil Stator Models Evaluation Based on Rotor 1 Configuration

Core Type	$R\ (mm)$	$\psi\ (°)$	$F_{xmax}\ (N)$	$F_{ymax}\ (N)$	$F_{zmax}\ (N)$	$T_{xmax}\ (Nm)$	$T_{ymax}\ (Nm)$	$T_{zmax}\ (Nm)$
Air Core	10	20.7	0.0027	0.0027	0.0090	5.76e-5	5.76e-5	9.13e-20
	20	45	0.0396	0.0396	0.0264	1.10e-4	1.10e-4	2.86e-20
	25	61.9	0.0438	0.0438	0.0235	1.80e-3	1.80e-3	9,85e-20
Iron Core	10	20.7	0.038	0.038	0.1244	7.97e-4	7.97e-4	1.36e-19
	20	45	0.2103	0.2103	0.1402	5.80e-3	5.80e-3	9.40e-19
	25	61.9	0.2405	0.2405	0.1291	1.00e-2	1.00e-2	2.62e-19

Table 2.3: 5 Coil Stator Models Evaluation Based on Rotor 1 Configuration

Core Type	$R\ (mm)$	$\psi\ (°)$	$F_{xmax}\ (N)$	$F_{ymax}\ (N)$	$F_{zmax}\ (N)$	$T_{xmax}\ (Nm)$	$T_{ymax}\ (Nm)$	$T_{zmax}\ (Nm)$
Air Core	8	23.6	0.0013	0.0013	0.0048	2.80e-5	2.80e-5	1.19e-21
	10	30	0.0036	0.0036	0.0097	8.15e-5	8.15e-5	4.49e-21
	15	48.6	0.0164	0.0164	0.0179	4.88e-4	4.88e-4	3.18e-20
Iron Core	8	23.6	0.0237	0.0237	0.0871	5.09e-4	5.09e-4	2.17e-20
	10	30	0.0497	0.0497	0.1340	1.10e-3	1.10e-3	1.05e-19
	15	48.6	0.1274	0.1274	0.1391	3.80e-3	3.80e-3	2.88e-19

Table 2.4: Rotor Models Evaluation under 3 Coils Stator with R=20 mm, Iron Core.

Rotor models	$F_{xmax}\ (N)$	$F_{ymax}\ (N)$	$F_{zmax}\ (N)$	$T_{xmax}\ (Nm)$	$T_{ymax}\ (Nm)$	$T_{zmax}\ (Nm)$
Model 1	0.1983	0.1718	0.2099	4.10e-3	4.80e-3	8.40e-19
Model 2	0.0091	0.0079	0.0097	2.89e-4	3.34e-4	2.54e-19
Model 3	0.0153	0.0132	0.0162	4.89e-4	5.65e-4	2.37e-19
Model 4	0.2136	0.1850	0.2261	4.60e-3	5.30e-3	2.42e-18

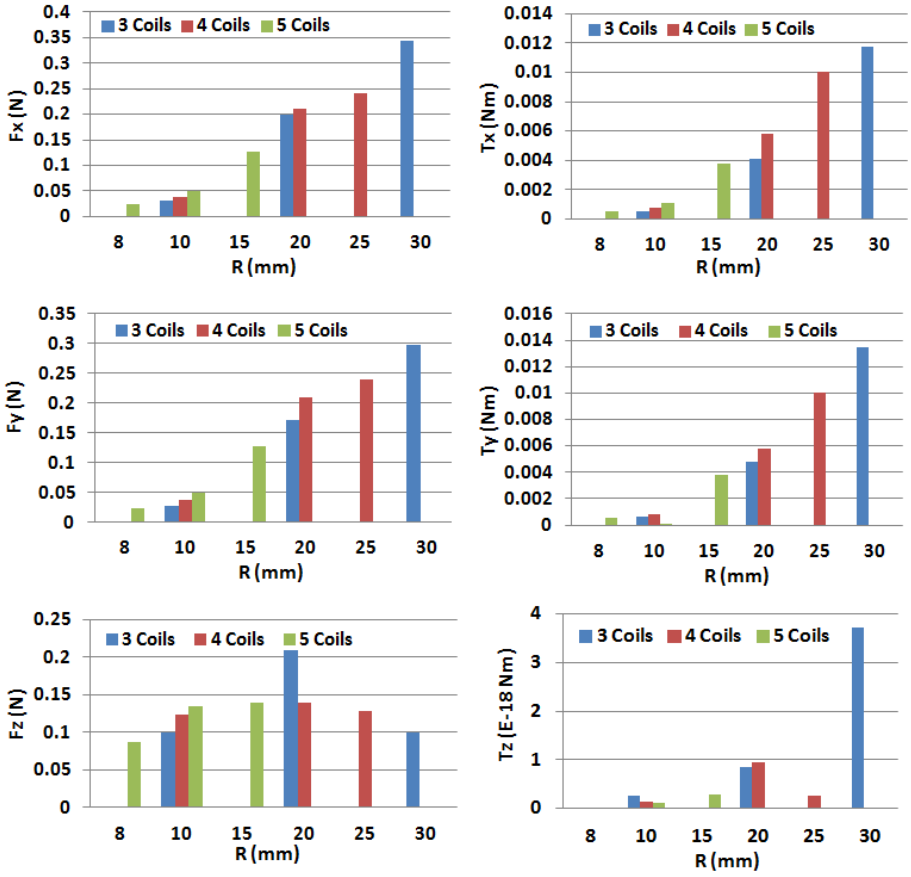

Figure 2.7: Stator design comparisons.

than those generated in the rotor 2 and 3 due to the disc magnet. Rotor 3 has a better performance than rotor model 2. To analyze if the design of our active locomotion system works well, the camera dynamics and abdominal wall tissue model have to be involved. Being evaluated by the Solidworks software, the camera weights approximately 15 grams, and the distance from the gravity center to rotor's center is about 10 mm. The threshold force and torque to actuate the camera are 0.147 N and 0.001 47 Nm which indicates the rotor 1 and 4 are capable of providing enough force and torque for the locomotion mechanism.

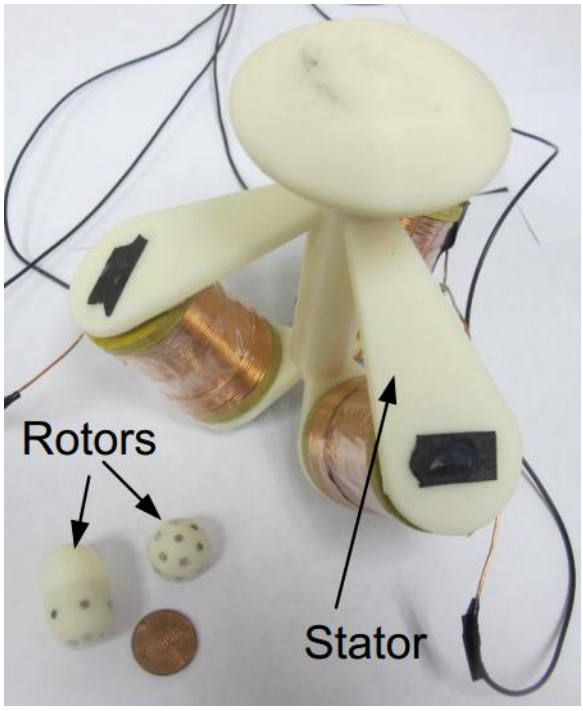

Figure 2.8: The fabricated rotors and stator.

2.7.2 Camera System Fabrication

Rotor Fabrication

According to the analytical evaluations of the rotors in Table 2.4, the rotor 4 is selected due to the best force and torque performance among all four rotor designs. The sizes of the small cylinder magnets and the disc magnet are $1/10'' \times 1/10''$ (K&J Magnetics, NdFeB N42) and $5/8'' \times 1/16''$ (K&J Magnetics, NdFeB N52) with their residual magnetizations as 1.32 Tesla and 1.43 Tesla respectively. Based on the size of the magnets, the size of the capsule-shaped camera is designed as $0.75'' \times 1.18''$. A 3D printer is used to fabricate the prototype, as shown in Fig. 2.8.

Stator Fabrication

According to the analytical evaluation in Table 2.1, 2.2, 2.3, the 3 coils iron-core stator with 20 mm outer radius shows the best balance of reasonable dimension and sufficient force and torque for manipulating the camera. Therefore, in this paper we

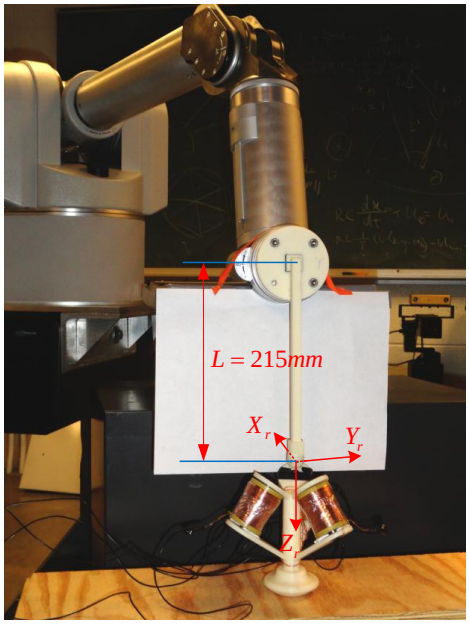

Figure 2.9: The force and torque measurement setups.

fabricate this stator design for experimental test, as shown in Fig. 2.8. The coils are wound by 600 turns copper ware with 1 mm^2 cross sectional area. The height, outer radius and inner radius of each of the coils are 40 mm, 20 mm, and 5 mm respectively. The resistance of each coil is about 1.3 Ω. The soft iron rods applied in the coils are 9.5 mm in diameter and 60 mm in height with their maximum magnetic permeability 2000 H/m. In order to provide controllable independent current inputs for each of the coils, three DC power supplies (Mastech HY5020E) with a maximum output voltage 50 V and maximum current output 20 A are adopted for driving the camera's transitional and rotational motions.

2.7.3 Force and Torque Measurement Experiments

For validating the analytical model and the maximum generated forces/torques, experiments were set up based on our fabricated rotor and stator. The magnetic force and torque were measured by Barrett WAM arm's Six-Axis Force/Torque sensor with 50 mN force sensing resolution and 1.5 mNm torque sensing resolution. In both of the force and torque measurements, the z axis of the rotor Z_r was configured to coincide

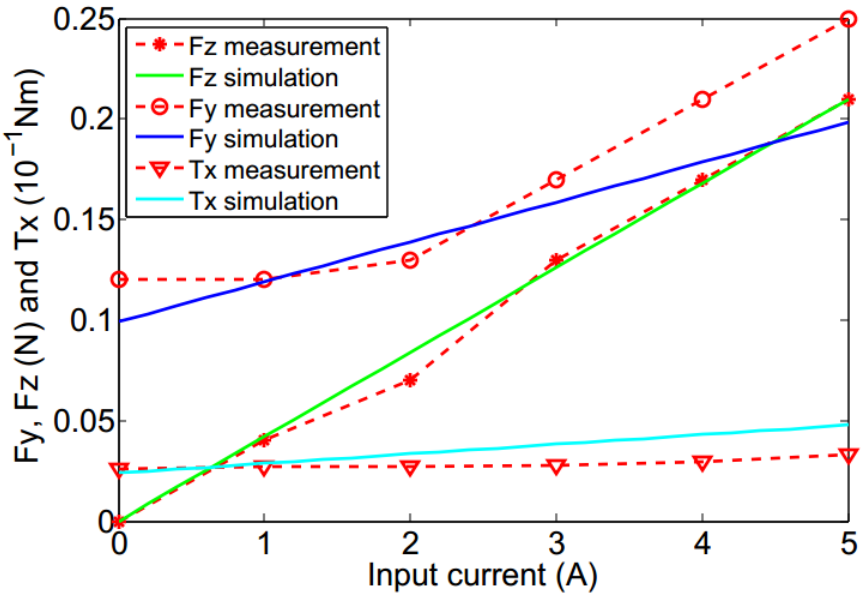

Figure 2.10: Force and torque comparison results between measurements and simulations.

with the symmetry axis of the stator. And the distance from the coils to the center of the rotor was set as 40 mm. For measuring the magnetic force and torque, the locomotion mechanism was placed upside down, as shown in Fig. 2.9. An "L" shaped lever arm connected the rotor model 4 on one side, and was attached to the F/T sensor on the other side.

The forces along Z_r axises were measured under various current input limits from 0 to 5 A. And the torques were measured around X_r axis. Due to the torque sensing resolution, the F/T sensor was not capable of recording the generated torque according to the simulation results in Table 2.1–2.4. Therefore, the lever arm was used to amplify torque measurements for compensating the limits of the sensor. Figure. 2.10 compares the measurements and simulation results of the generated force and torque. For measuring F_z, all the coils were applied the same current value and direction ranging from 0 to 5 A. In order to measure F_y and T_x, the current of the coil on Y_rZ_r plane ranges $0 \sim -5$ A with the other coils keeping a constant current input at 5 A. The preliminary comparison results indicate that the simulation results

from our developed analytical model agrees with the measurement results from the F/T sensor.

2.8 Summary

In this chapter, we proposed an innovative active locomotion mechanism for a wireless laparoscopic camera. The locomotion mechanism enables a unified control of transition and orientation for the camera by varying the input current of stator's coils. This design eliminates the need for an articulated design and therefore the integrated motors to significantly reduce the size of the camera. Three stator designs and four rotor designs are developed and evaluated by simulations and experiments for testing manipulation capability of different designs. According to the simulation and experimental results, the proposed designs are able to provide reasonable force and torque to translate and rotate a laparoscopic camera inside patient's abdominal cavities.

Although this design benefits from its small size, simple fabrication, and unified actuation, for stable motion control the stator needed at least 5 A current inputs, which resulted in coil overheating. To resolve this problem, a line-arranged driving unit is proposed and investigated in the next chapter.

Chapter 3

Line-arranged Rotor Driving Unit Design

3.1 Abstract

This chapter introduces a line-arranged rotor driving unit design for a wireless laparoscopic surgical camera based on the experimental investigations of the previous semi-spherical rotor design. The mechanism consists of a flat-arranged stator with 17 iron-core coils and a line-arranged rotor with 3 cylindrical permanent magnets inside the camera. This design unifies the camera's fixation and manipulation by adjusting input currents in the stator which generates 3D rotational magnetic fields, and decouples the camera's locomotion into pan motion and tilt motion. In the simulation studies, the proposed design can conservatively achieve 360° pan motion with a 22.5° resolution, and 127° $\sim$ 164° maximum tilting range for tilt motion which depends on tilt motion working modes and the distance between the rotor and the stator.

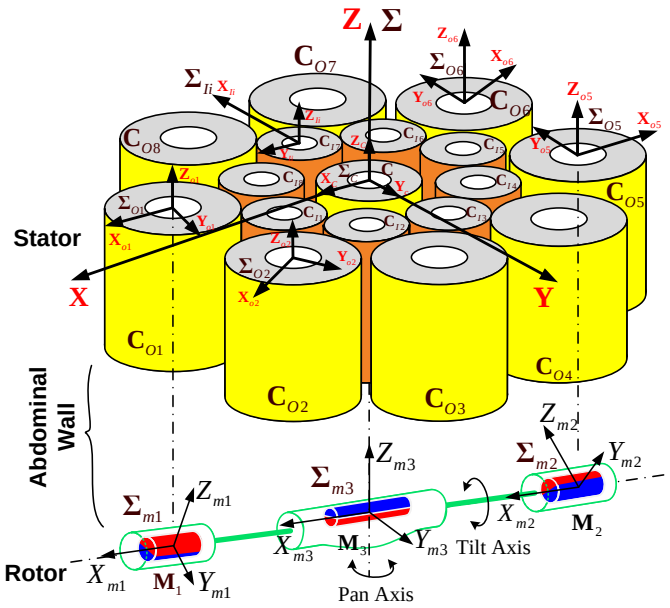

Figure 3.1: The conceptual illustration of the our proposed locomotion mechanism design.

3.2 Design Consideration of Line-arranged Rotor Driven Unit

The locomotion mechanism of laparoscopic camera system consists of a magnetic rotor and a coil winding stator. In this paper, we concentrate on developing the locomotion mechanism and leave out the other components in the camera for future work. The camera design has three housings connected by two rigid bars, as shown in Fig. 3.1. Each of the housing can freely rotate around the axis of the bar. For each tail-end housing, a diametrically magnetized cylindrical magnet is embedded with a free axial rotation relative to its housing. One diametrically magnetized cylindrical magnet is fixed with the central housing. All the other main components of the camera, such as a camera module, batteries, internal sensors, wireless modules, are sealed in the central housing. The stator consists of multiple coils to generate a rotating magnetic field for pan and tilt motions of the camera.

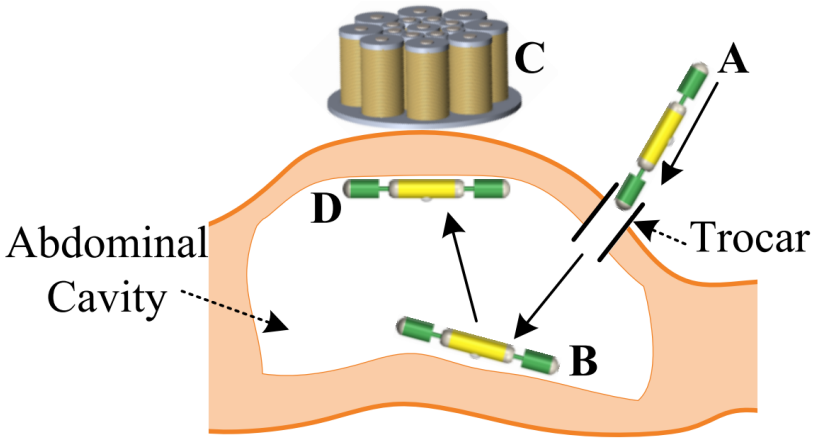

Figure 3.2: Application scenario of the laparoscopic camera system.

Fig. 3.2 shows the application scenario of our proposed laparoscopic camera system. To insert the laparoscopic camera (A) into the patient's abdominal cavity, a trocar has to be applied first. After the camera reaches to (B) position, the stator (C) is activated for attracting the camera against the abdominal wall at position (D). The process of posing camera from (B) to (D) can be assisted by using laparoscopic clamp forceps. A surgeon controls the current inputs to adjust a desired camera visual direction.

The working principle of our proposed camera system is illustrated in Fig. 3.1. The system is designed to enable two types of motions: orientation and translation. The orientation control is decoupled into a pan motion control and a tilt motion control that are capable to function separately based on our design. To initialize the pose of the camera, C_{O1}, C_{O5}, C are activated to align magnets $\mathbf{M}_1$, $\mathbf{M}_2$, $\mathbf{M}_3$ with the coils respectively.

For the pan motion of the camera, outer coils and tail-end magnets $\mathbf{M}_1$, $\mathbf{M}_2$ are mainly involved. Due to the symmetric design of the stator and rotor, the motion, that magnet $\mathbf{M}_1$ rotates from aligning with C_{O1} to aligning with C_{O2} while magnet $\mathbf{M}_2$ rotates from C_{O5} to C_{O6}, is the whole process we need to discuss. In order to keep the camera rotating around pan-axis during the pan motion, the current values in C_{O5} and C_{O6} have to separately synchronized with C_{O1} and C_{O2}. After the camera

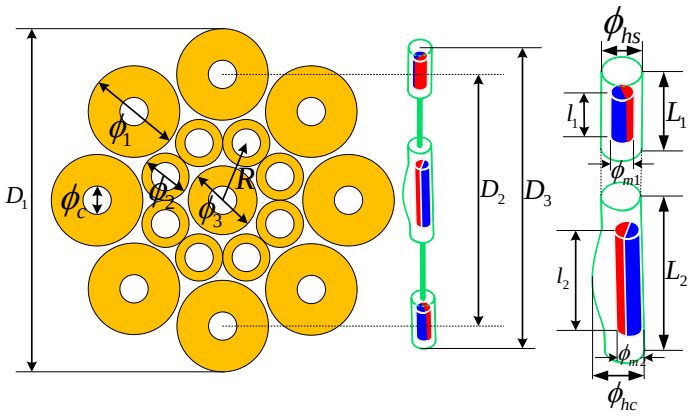

Figure 3.3: Rotor and stator design.

reaches the desired pan angle, the outer coils will replace the function of central coil C to provide the fixation of the camera against the abdominal wall.

The tilt motion is activated by the remaining coils to generate a torque along X_{m3} axis on the central magnet $\mathbf{M}_3$. The eletromagnetic torque applied on $\mathbf{M}_3$ generate a rotational motion on the central housing around tilt axis due to the fixed attachment of $\mathbf{M}_3$ and its housing. The purpose of translational control is to reposition the camera to a desired location. It can be achieved by the initialized coil setting and moving the stator manually. The magnets follow the repositioning of the stator to a new location.

Table 3.1: Stator and Rotor Design, Unit: [mm]

Stator				Rotor			
ϕ_1	32	R	23	ϕ_{hs}	12	l_1	12.7
ϕ_2	17	D_1	122	ϕ_{hc}	13	l_2	25.4
ϕ_3	24	D_2	90	ϕ_{m1}	6.35	L_1	14
ϕ_c	10	D_3	102	ϕ_{m2}	6.35	L_2	40

3.3 Configurations of Rotor and Stator

According to the working principle introduced in Section 3.2, it is desired to have the stator design with symmetric structure which arranges coils circularly around one central coil. To make the stator have sufficient control capability, it is designed with 8 outer coils, 8 inner coils, and 1 central coil by considering the compromise between coil sizes and the number of coils, as shown in Fig. 3.3. The specifications of the rotor and stator design are shown in Table 3.1. All the coils in the stator are 50 mm in height and wound by AWG23 copper wires which can tolerate 2.5 A maximum current. The windings of an outer coil, an inner coil and the central coil are 2000, 600, and 1000 turns respectively. For generating stronger magnetic field compared with air-core stators, iron cores with diameter 9 mm, height of 50 mm are applied to all the coils. Three diametrically magnetized cylindrical magnets are in three separate housings of the camera. Two identical tail-end magnets are with the residual magnetization 1.32 T, and the central magnet is with the residual magnetization 1.43 T.

3.4 Modeling of Actuation Mechanism

The objective of building an analytical model for the camera system's locomotion mechanism is twofold: to analyze the locomotion capabilities of the proposed design; and to control of the laparoscopic camera in real time. In this paper, we focus on the first objective based on the analytical model. The central problem of developing the model is how to calculate forces and torques generated on the magnets. The analytical models of spherical motors are based on Lorentz law due to their air-core stators Rossini et al. (2013), Wang et al. (2003), Liang et al. (2006). In our application the thickness of the abdominal wall is much greater than the air gap in the spherical motors. Iron-core coils are thus considered because the high magnetic permeability of soft iron can significantly enhance the coil's magnetic field. However, the Lorentz law can not handle the force and torque analysis with iron-core coils.

An alternative way to formulate magnetic force and torque is to consider a magnet as a magnetic moment $\mathbf{M}$. The equations can be represented as

$$\mathbf{T} = \mathbf{M} \times \mathbf{B}, \quad \mathbf{F} = (\mathbf{M} \cdot \nabla)\mathbf{B}, \tag{3.1}$$

where $\mathbf{B}$ is the magnetic flux density at the location of $\mathbf{M}$ Jackson (1999). If the size of the magnet is small enough, it can be assumed that the magnetic field applied over the magnet is uniform. Under this assumption, the computation of (3.1) is greatly simplified. However, considering the thickness of an abdominal wall and the sizes of magnets in our camera, it is not appropriate to use the assumption for deriving our analytical model. Therefore, two main problems have to be addressed first: how to represent the magnetic field of the iron-core stator; and how to calculate the magnetic force and torque without the simplified assumption. Then analytical models of the pan and tilt motions are developed.

3.4.1 Stator's Magnetic Flux Density B

For modeling the stator's magnetic flux density, a set of coordinates have to be set first. As shown in Fig. 3.1, Σ_{Oi}, Σ_{Ii}, Σ_C are the local frame of outer coils, inner coils and central coil respectively, where $i = 1, ..., 8$. It is important to note that for the purpose of clear illustration, we draw the coil's local coordinates on the top of them. But in all the following model developments, we set the origins of the local coordinates at the coil's bottoms. The representations of $\mathbf{M}$ and $\mathbf{B}$ in (3.1) have to share the same coordinates. Therefore, the central coil local frame Σ_C is adopted as a reference frame $\Sigma = \{X, Y, Z\}$ for establishing the relationship of coordinates between the stator and rotor. The transformation from local coil frame Σ_j to the reference frame Σ is expressed as

$$\mathbf{P} = \mathbf{R}_j \mathbf{P}_j + \mathbf{T}_j, \tag{3.2}$$

where $\mathbf{P} = (x, y, z)$ and $\mathbf{P}_j = (x_j, y_j, z_j)$ are the same point in Σ and Σ_j, and $j = Oi, Ii, C$. $\mathbf{R}_j$ and $\mathbf{T}_j$ are a rotational matrix and a translational vector.

It has been claimed in Kummer et al. (2010) that an iron-core coil's magnetic flux density has linear relationships with its input current, and all the individual fields can be superimposed linearly. This assumption has been verified at the coinciding point of the axes of the coils. According to our stator design, the working space is not under the verified region. We extend the assumption that it still holds when the working space has an offset to the coil axes. This extended assumption is verified in Section 3.5.1. The superimposed magnetic flux density in Σ is represented as

$$\mathbf{B}(x, y, z) = \sum_{j=1}^{N} \mathbf{R}_j \mathbf{B}_j^u(x_j, y_j, z_j) I_j, \tag{3.3}$$

where $\mathbf{B}_j^u$ is the unit current magnetic flux density of coil j in its local frame; N is the number of coils. Finite Element Method (FEM) can yield accurate solutions of a coil's magnetic flux density by building extra fine meshes. However, the expensive computational time of FEM fails this method to serve in a real time application. A magnetic dipole model fitting method proposed in Kummer et al. (2010), which adopts the coil's axial magnetic flux density from FEM as the fitting data, is applied for estimating the parameter p and $\mathbf{l}$ in

$$\mathbf{B}_j^u(\mathbf{P}_j) = \frac{\mu_0}{4\pi} \left(-\frac{\mathbf{M}}{|\mathbf{P}_j|^3} + \frac{3(\mathbf{M} \cdot \mathbf{P}_j)\mathbf{P}_j}{|\mathbf{P}_j|^5} \right), \tag{3.4}$$

where $\mathbf{M} = p\mathbf{l}$ is the coil's equivalent magnetic moment.

3.4.2 Rotor's Magnetic Moment M

To calculate (3.1), the magnetic moments $\mathbf{M}$ have to be determined. The rotor of the camera consists of three diametrically magnetized cylinder magnets: one central magnet fixed with its housing, two tail-end magnets rotationally free around the tilt axis with respect to their housings. Body fixed frames of the magnets are set as Σ_{m1},

Σ_{m2} and Σ_{m3}. The magnetic moment of the kth magnet in Σ_{mk} is expressed as

$$\mathbf{M}_k = M_0 V \cdot [0, 0, 1]^T, \tag{3.5}$$

where $k = 1, 2, 3$; M_0 is the residual magnetization of the magnet; $V = \pi(a_k/2)^2 l_k$ is the volume of the magnet k; a_k and l_k are the diameter and length of the kth magnet; The transformation from Σ_{mk} to Σ is represented by

$$\mathbf{P} = \mathbf{R}_{mk}\mathbf{P}_{mk} + \mathbf{T}_{mk}, \tag{3.6}$$

where $\mathbf{P}_{mk}$ denotes a point in Σ_{mk}. $\mathbf{R}_{mk}$ and $\mathbf{T}_{mk}$ are a rotational matrix and a translational vector.

3.4.3 Force and Torque Modeling

The locomotion of the camera depends on forces and torques applied on all the three magnets. A strategy to solve this problem is to calculate the force and torque separately on each magnet and superimpose them. For deriving the magnetic force and torque on magnet $\mathbf{M}_k$, $\mathbf{B}$ has to be integrated over the magnet's volume V. Due to the complexity of $\mathbf{B}$, it is cumbersome to use its exact representation in (3.3). Instead, expending the magnetic field at the origin point of Σ_{mk} by using Taylor series expansion is an effective way to simplify $\mathbf{B}$ Groom (1997). Equation (3.1) is reformulated as

$$\bar{\mathbf{T}}_k = \int_V \{(\mathbf{M}_k \times \bar{\widetilde{\mathbf{B}}}) + [\bar{\mathbf{r}} \times (\mathbf{M}_k \cdot \nabla)\bar{\widetilde{\mathbf{B}}}]\}\, dv, \tag{3.7}$$

$$\bar{\mathbf{F}}_k = \int_V (\mathbf{M}_k \cdot \nabla)\bar{\widetilde{\mathbf{B}}}\, dv, \tag{3.8}$$

where '-' represents a vector in Σ_{mk}, $\bar{\mathbf{r}}$ is the position of an element of the magnet in Σ_{mk}; $\bar{\widetilde{\mathbf{B}}}$ and $\widetilde{\mathbf{B}}$ are Taylor series expansions of $\mathbf{B}$ in Σ_{mk} and Σ respectively; and

$\widetilde{\widetilde{\mathbf{B}}} = \mathbf{R}_{mk}\widetilde{\mathbf{B}}|_{(\mathbf{P}=\mathbf{R}_{mk}\mathbf{P}_{mk}+\mathbf{T}_{mk})}$. Equations (3.7) and (3.8) are solved by ignoring high order gradient terms, i.e.

$$\bar{T}_{k\bar{x}} = -m_k V(\lambda_2^k B_x + \eta_2^k B_y + \zeta_2^k B_z), \tag{3.9}$$

$$\bar{T}_{k\bar{y}} = m_k V(\lambda_1^k B_x + \eta_1^k B_y + \zeta_1^k B_z), \tag{3.10}$$

$$\begin{aligned}\bar{T}_{k\bar{z}} =&(1/12)m_k V l_k^2(\lambda_2^k B_{x\bar{z}\bar{x}} + \eta_2^k B_{y\bar{z}\bar{x}} + \zeta_2^k B_{z\bar{z}\bar{x}})- \\ &(1/4)m_k a_k^2 V(\lambda_1^k B_{x\bar{z}\bar{y}} + \eta_1^k B_{y\bar{z}\bar{y}} + \zeta_1^k B_{z\bar{z}\bar{y}}),\end{aligned} \tag{3.11}$$

$$\bar{F}_{k\bar{x}} = m_k V(\lambda_1^k B_{x\bar{z}} + \eta_1^k B_{y\bar{z}} + \zeta_1^k B_{z\bar{z}}), \tag{3.12}$$

$$\bar{F}_{k\bar{y}} = m_k V(\lambda_2^k B_{x\bar{z}} + \eta_2^k B_{y\bar{z}} + \zeta_2^k B_{z\bar{z}}), \tag{3.13}$$

$$\bar{F}_{k\bar{z}} = m_k V(\lambda_3^k B_{x\bar{z}} + \eta_3^k B_{y\bar{z}} + \zeta_3^k B_{z\bar{z}}), \tag{3.14}$$

where B_i is ith component of $\mathbf{B}$ in Σ; B_{ij} is the first order gradient of B_i on variable j; B_{ijr} is the second order gradient of B_{ij} on variable r. In (3.9), (3.10), $j = x, y, z$ is a coordinate in Σ. In (3.11)-(3.14), $j, r = \bar{x}, \bar{y}, \bar{z}$ are coordinates in Σ_{mk}. $\lambda_n^k, \eta_n^k, \zeta_n^k, \rho_n^k$ are the components of $\mathbf{R}_{mk} = (\boldsymbol{\lambda}^k, \boldsymbol{\eta}^k, \boldsymbol{\zeta}^k)_{3\times 3}$ and $\mathbf{T}_{mk} = (\rho_1^k, \rho_2^k, \rho_3^k)^T$, $n = 1, 2, 3$.

Because the number of coils is 17, (3.7) and (3.8) are decomposed as a 3×17 force matrix $\bar{\mathbf{F}}_k^u$, a 3×17 torque matrix $\bar{\mathbf{T}}_k^u$ and a 17×1 input current vector $\mathbf{I}$. $\bar{\mathbf{T}}_k^u$ and $\bar{\mathbf{F}}_k^u$ are derived from unit current inputs. Since all the forces and torques should be analyzed in a common frame, $\bar{\mathbf{T}}_k$ and $\bar{\mathbf{F}}_k$ have to be represented in the reference frame by using $\mathbf{R}_{mk}$,

$$\mathbf{T}_k = \mathbf{R}_{mk}\bar{\mathbf{T}}_k^u\mathbf{I}, \quad \mathbf{F}_k = \mathbf{R}_{mk}\bar{\mathbf{F}}_k^u\mathbf{I}. \tag{3.15}$$

With (3.15), different groups of coils can be activated to achieve desired motions.

3.4.4 Pan Motion Analytical Model

The idea of the locomotion mechanism of our proposed camera system is to separately activate its pan and tilt motion. The coil activation of pan motion is shown in

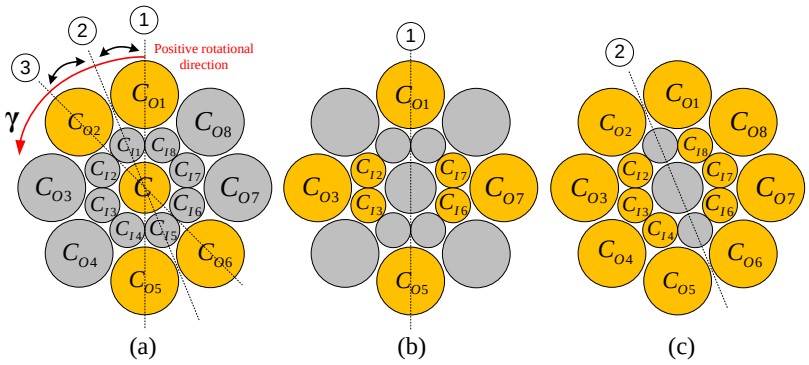

Figure 3.4: Pan and tilt motion working modes. (a) illustrates a single phase of pan motion; (b) shows tilt mode 1; and (c) shows tilt mode 2.

Fig. 3.4(a) where the highlighted circles are the coils to be activated. A full 360° pan motion consists of 8 identical phases. Fig 3.4(a) shows a single phase of coils activation. The camera is centered at C and rotated from ① to ③ by adjusting the current inputs in $C_{O1,2,5,6}$. During the pan motion, the currents in C_{O5} and C_{O6} is simultaneous with C_{O1} and C_{O2} respectively while coil C provides attractive force for the camera fixation. Theoretically, the camera can stop at any pan angle between ① and ③ by adjusting the input currents. But in practical applications, a 22.5° resolution is sufficient because field of views (FOV) of commercially available camera modules are much larger than 22.5°, e.g. PillCam SB2 (Given Imaging Inc.) with FOV 156°, MicroCam (IntroMedic Inc.) with FOV 150° Moglia et al. (2009).

Due to the symmetrical structure of the camera system, only $\mathbf{M}_1$ is analyzed under coil C_{O1} and C_{O2}. To calculate the force and torque, $\mathbf{M}_1$'s direction has to be determined according to (3.5) and (3.6). Considering $\mathbf{M}_1$ aligns with the magnetic field generated by $C_{O1,2}$, the currents are designed with the rotational feedback angle γ around $\mathbf{Z}$ axis, as shown in Fig. 3.4(a). For the pan motion from position ① to ②, the currents are designed as

$$I_{O1} = \begin{cases} \xi I_{max} + (1-\xi) I_{max}(1 - \left|\frac{\gamma - \gamma_{g1}}{\gamma_{g1}}\right|), \gamma < \gamma_{g1} \\ I_{max}, \gamma \geq \gamma_{g1} \end{cases} \tag{3.16}$$

$$I_{O2} = \begin{cases} I_{max}, \gamma < \gamma_{g1}, \\ \xi I_{max} + (1-\xi) I_{max}(1 - \left|\frac{\gamma - \gamma_{g1}}{\gamma_{g1}}\right|), \gamma \geq \gamma_{g1} \end{cases} \tag{3.17}$$

where $\xi \in [0, 1]$ is a coefficient, which initially reduces I_{O1} for the starting of the rotation; $|I_{max}| \leq 2.5\,\text{A}$; $\gamma_{g1} = 22.5°$. To rotate the camera from ② to ③, $C_{O1,2}$ are activated by setting $I_{O1} = 0$,

$$I_{O2} = \xi I_{max} + (1-\xi) I_{max} \left|(\gamma - \gamma_{g2})/\gamma_{g2}\right|, \tag{3.18}$$

where $\gamma_{g2} = 45°$. The direction of magnetic field generated by $C_{O1,2}$ at the center of $\mathbf{M}_1$ in Σ_{m1} is represented as

$$\mathbf{d}_1 = \mathbf{R}_{m1}^T \frac{\mathbf{R}_{O1}\mathbf{B}_{O1}^u I_{O1} + \mathbf{R}_{O2}\mathbf{B}_{O2}^u I_{O2}}{|\mathbf{R}_{O1}\mathbf{B}_{O1}^u I_{O1} + \mathbf{R}_{O2}\mathbf{B}_{O2}^u I_{O2}|}. \tag{3.19}$$

Therefore, the forces applied on $\mathbf{M}_{1,2,3}$ are derived according to (3.15)

$$\mathbf{F}_k = \mathbf{R}_{mk}\bar{\mathbf{F}}_k^u \mathbf{I}_k^{act}, \tag{3.20}$$

$\mathbf{I}_k^{act}$ is the current vector of activated coils, $k = 1, 2, 3$.

Fig. 3.5 illustrates the dynamics of the camera system which is analyzed in Σ_o. $\mathbf{X}_o$ is along the camera's long axis, $\mathbf{Z}_o$ is with the same direction of $\mathbf{Z}$ in Σ, and $\mathbf{Y}_o$ is perpendicular to $\mathbf{X}_o$ and $\mathbf{Z}_o$. $F_1^{x,y,z}$ and $F_2^{x,y,z}$ are derived by using $\mathbf{F}_1$, $\mathbf{F}_2$ and the camera's pan angle with respect to Σ. The magnetic torques T_1^m and T_2^m rotate the tail-end magnets to align with the magnetic field. Due to the lubricated friction between the tail-end magnet and its housing, we only need to confirm that T_1^m and T_2^m can overcome T_f^{m1} and T_f^{m2} when the tail-end housings are moving.

$$T_i^m \geq T_f^{mi} = \mu_{lub}|\mathbf{F}_i^y + \mathbf{F}_i^z| r_{mag}, \tag{3.21}$$

where T_f^{mi} is the frictional torque between the magnet and its housing; μ_{lub} is the lubricated friction coefficient; r_{mag} is the radius of the magnet; and F_i^z is the magnetic force in $\mathbf{Z}_o$ direction, $i = 1, 2$. (3.21) will be validated in Section 3.5.4.

The pan motion is actuated by F_1^y and F_2^y. By considering the tissue-housing sliding friction coefficient μ_{tis} as 0.1 Loring et al. (2005), the lubricated friction coefficient μ_{lub} between metal and plastic can be made smaller than μ_{tis}. The tail-end housings roll against the tissue if (3.22) is satisfied

$$T_{pan=} r_{cam}(F_1^y + F_2^y - F_1^r - F_2^r) - T_f^{pan} \geq 0, \tag{3.22}$$

where $r_{cam} = D_2/2$; $F_{1,2}^r$ are the rolling resistances between the housings and the tissue; T_f^{pan} is the central housing's spinning frictional torque which is modeled by

$$T_f^{pan} = \mu_{tis}(F_1^z + F_2^z + F_3^z - G)r_{avg}, \tag{3.23}$$

where $r_{avg} = L_2/4$ is the average distance from the rotational center to friction applied point on the central housing; G is the whole gravity of the camera. To fix the camera against the abdominal wall,

$$F^z = F_1^z + F_2^z + F_3^z - G > 0, \tag{3.24}$$

has to be always satisfied. The rolling resistance $F_{1,2}^r$ are modeled by following Hunter's work Hunter (1961), which is under some assumptions: the tissue is a viscoelastic half space by comparing thickness of abdominal wall ($30 \sim 50\,\text{mm}$) and tail-end housing indention (maximum indention is $\phi_{hs}/2 = 6\,\text{mm}$) and the tail-end housing rotates at constant velocity V which neglects the acceleration term in order to simplify the preliminary analysis.

$$F_i^r = \frac{2F_N}{\phi_{hs}}(b - \frac{V\tau}{1+f} + \Gamma\frac{a_0}{a}), \tag{3.25}$$

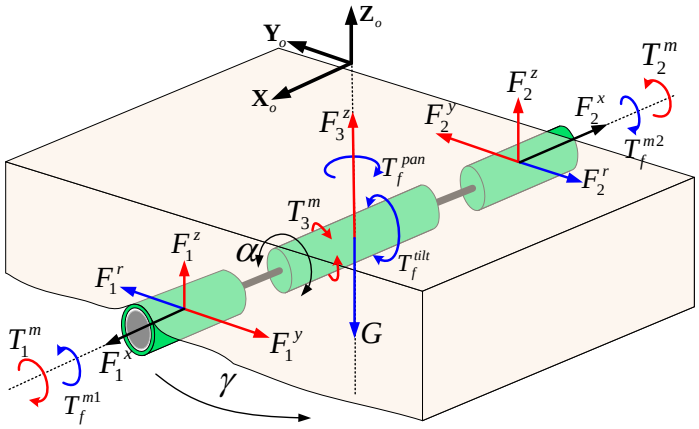

Figure 3.5: Analysis of the camera system dynamics.

where F_N is the load per unit length of a cylindrical tail-end housing; τ and f are parameters which specify the model of the viscoelastic tissue; a_0 denotes semicontact width of the housing when $V = 0$. The unknown variables a, Γ, b are solved by a set of boundary conditions.

3.4.5 Tilt Motion Analytical Model

In tilt motion modes, the central coil C is set off and replaced by the outer coils to provide attractive force for pulling the camera against the abdominal wall. As shown in Fig. 3.4(b) and 3.4(c), the dash lines represent the two tilt modes. In Fig. 3.4(b), coil $C_{O1,5}$ are activated for balancing the weight of the camera, and coil $C_{I2,3,6,7}$, $C_{O3,7}$ are activated for generating tilt motions on the central magnet. Fig. 3.4(c) is similar to Fig. 3.4(b), but with coils $C_{O1,2,5,6}$ activated for camera weight balancing and with coils $C_{I2,3,4,6,7,8}$, $C_{O3,4,7,8}$ activated for generating tilt motion. The torque generated by the activated coils are represented by

$$\mathbf{T}_3 = \mathbf{R}_{m3}\bar{\mathbf{T}}_3^u\mathbf{I}_{tilt}, \tag{3.26}$$

where $\mathbf{I}_{tilt}$ is the current vector of the activated coils. Fig. 3.4 shows T_3^m is the eletromagnetic rotational torque around the central housing's long axis, and is derived

from $\mathbf{T}_3$ by using $\mathbf{R}_{m3}$. The tilt motion of the central housing requires T_3^m can overcome the frictional torque T_f^{tilt} and the torque T_g from central housing 's gravity $\mathbf{G}_c$. Therefore,

$$T_{tilt} = T_3^m - T_f^{tilt} - T_g > 0, \tag{3.27}$$

has to be satisfied, where T_f^{tilt} is calculated by

$$T_f^{tilt} = \mu_{tis}(F_1^z + F_2^z + F_3^z - G)r_{mag}. \tag{3.28}$$

The necessary conditions for enabling pan and tilt motions in (3.21), (3.22), (3.24), (3.27) are validated in Section 3.5.5.

3.5 Simulation Assessment

In this section, the locomotion mechanism of our proposed design is evaluated by simulations. The extended assumption on superimposing magnetic field is firstly verified. The analytical model of magnetic field and electromagnetic force and torque are evaluated by using a benchmark software. And the locomotion capabilities of pan and tilt motions are investigated separately in the last part of this chapter.

3.5.1 Verification of Extended Assumption

To verify the extended assumption for developing (3.3), two points in the working space are selected. The evaluation point of pan motion is set on the intersection line of two planes which are a tangent plane to separate the coils C_{O1} and C_{O2}, and a cut-through plane which is determined by the two coils' axes, as shown in Fig. 3.6(a) point A. The distance from A to the two coils' bottom is set as 30 mm. The tilt motion evaluation point B shown in Fig. 3.6(b) is set on the axis of the central coil with a distance of 30 mm to the coil's bottom. The coils C_{I2} and C_{I4} are selected for verifying the tilt case. Fig. 3.7(a) and Fig. 3.7(b) show the verification results by using

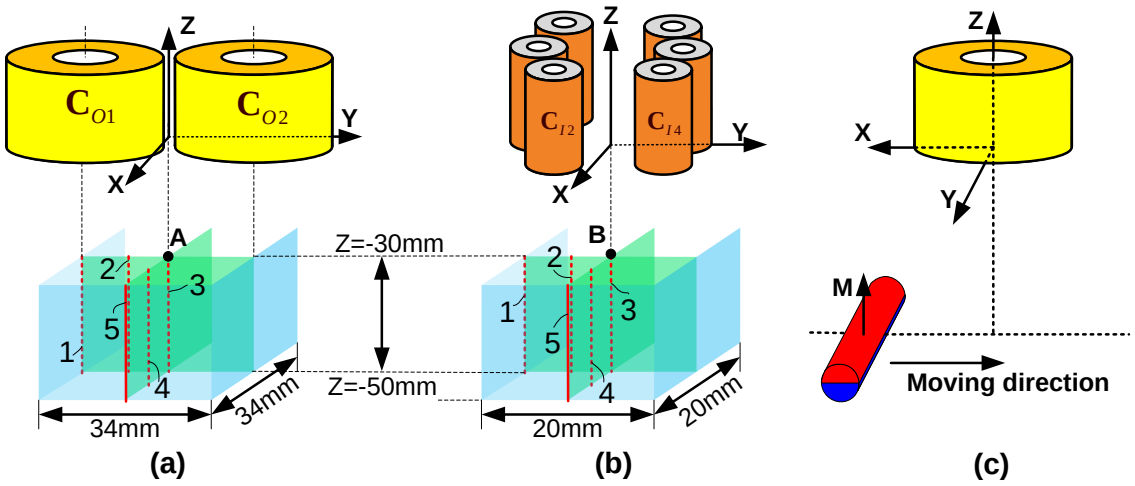

Figure 3.6: (a) and (b) illustrate the working space for verifying the extended assumption in Section 3.5.1, and the evaluation space of the analytical magnetic field in Section 3.5.2. (c) shows the configuration for evaluating the analytical model of force and torque in Section 3.5.3.

COMSOL Multiphysics 4.3a (COMSOL Inc., Sweden). The relative permeability of the iron core is set as 3000 H/m. Fig. 3.7(a) and 3.7(b) validate that the magnetic fields generated by the two pairs of coils can be represented by summation of the fields from the individual coils of each pair.

3.5.2 Evaluation of the Superimposed Magnetic Fields

For evaluating the superimposed magnetic field in (3.3), a comparison between the analytical model and the simulation result from COMSOL is implemented. In Fig. 3.6, two cubic working spaces are selected which are below two outer coils Fig. 3.6(a) and six inner coils Fig. 3.6(b) with $Z = -30\,\text{mm} \sim -50\,\text{mm}$. The unit current parameters m and l of an outer coil and an inner coil are $p = 3.81\,\text{Am}^2$, $l = 1.29\,\text{m}$ and $p = 2.41\,\text{Am}^2$, $l = 0.04\,\text{m}$ respectively. Due to the difficulty for analyzing all the points in the working spaces, lines $1-5$ in Fig. 3.6(a) and lines $1-5$ in Fig. 3.6(b) are selected according to their representative positions and the symmetry of the working spaces. In Fig. 3.6(a), (x,y) coordinates of line 1-5 are (0, −17), (0,−11), (0,0), (11,0), (17,0). In Fig. 3.6(b), (x,y) coordinates of line 1-5 are (0, −10), (0,−5), (0,0), (5,0),

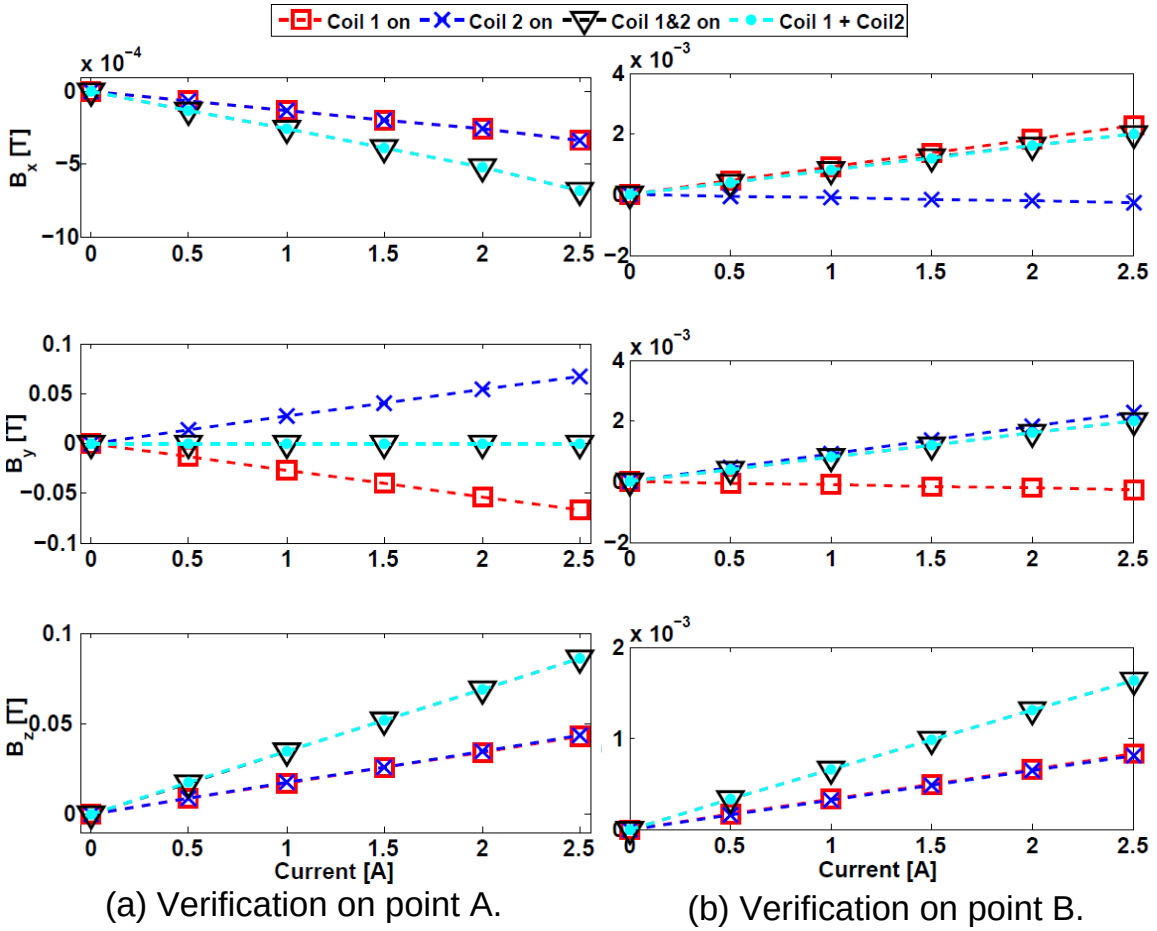

(a) Verification on point A.

(b) Verification on point B.

Figure 3.7: Verifications on the assumption of superimposing magnetic fields.

(10,0), unit [mm]. The magnetic flux density **B** in (3.3) is expressed by the norm of magnetic field strength **H** because of its concise and comprehensive expression of magnetic field. Fig. 3.8(a) and 3.8(b) show the comparison between the COMSOL results and our analytical model results for the two working spaces. The average differences are 8.97% (the case in Fig. 3.6(a)) and 11.86%(the case in Fig. 3.6(b)).

3.5.3 Evaluation of Force and Torque Model

This evaluation aims at proving the validation of the analytical model of force and torque developed in (3.15). The evaluation is implemented by using diametrically magnetized cylindrical magnets with the two different sizes which have been explained

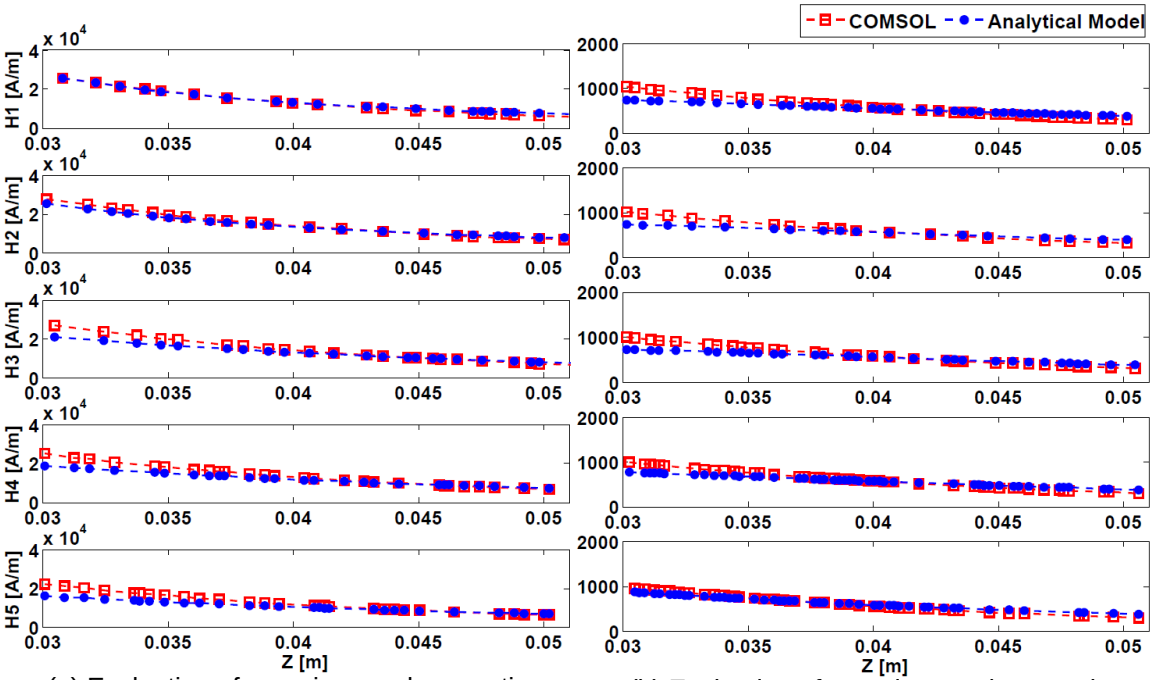

(a) Evaluation of superimposed magnetic field of outer coils.

(b) Evaluation of superimposed magnetic field of inner coils.

Figure 3.8: The analytical model of magnetic field evaluation.

in Section 3.3. The long axis of the magnet is perpendicular to XZ plane and centered at X=$-20 \sim 20$ mm, Z=-30 mm, as shown in Fig. 3.6(c). The magnetized direction of the magnet is always kept in **Z** direction. The magnetic field is generated by a single coil which has the configuration of outer coils in Section 3.3 with a maximum 2.5 A current input. A comparison model is built by COMSOL with 879, 160 mesh elements and 1 mm maximum element size of the selected mesh. Fig. 3.9 shows the comparison results of the force and torque agree well for the magnet with the length of 12.7 mm. For the magnet with the length of 25.4 mm, the agreement of results are worse than the shorter magnet's. This is due to the high order terms in (3.9)-(3.14) are ignored in order to simplify the calculation. Although the accuracy of the model can be further improved, it still can provide us a reasonable assessment for the locomotion performance of our proposed design. The following pan/tilt motion analyses will base on this analytical model.

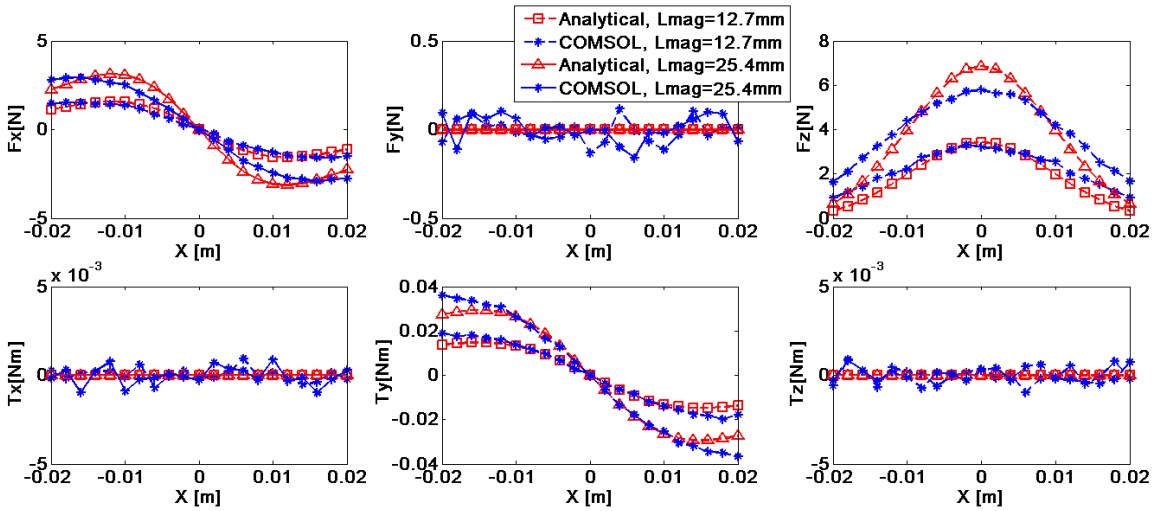

Figure 3.9: Analytical force and torque models evaluation on two different sizes of cylindrical magnets.

3.5.4 Pan Motion Evaluation

In this paper, we conduct quasi-static evaluations to quantize the locomotion capability of the camera system. For the pan motion, (3.22) and (3.24) are to be validated by orientating the camera from ① to ③ as shown in Fig. 3.4(a). The viscoelastic tissue is modeled as Standard Linear Solid (SLS) model which is characterized by spring module $E_1 = 4.28 \times 10^3$ N/m^2, spring-dashpot series $E_2 = 1.61 \times 10^4$ N/m^2, $\eta = 8.05 \times 10^3$ N-s/m^2, Poisson ratio $\nu = 0.5$ Wang et al. (2013). The friction coefficients are set as $\mu_{tis} = 0.1$, $\mu_{lub} = 0.05$. According to Hunter (1961), we maximize F_i^r in (3.25) by setting $V = a_0/\tau$.

The pan motion consists of two phases $0° \sim 22.5°$ and $22.5° \sim 45°$. $C_{O1,2,5,6}$ and C are activated in Fig. 3.10d-3.10h. During the period $0° \sim 22.5°$, the currents are set as $I_{O1} = I_{O5}$ (refer to (3.16)), $I_{O2} = I_{O6} = I_{max}$, $I_C = 0.2$ A with $\xi = 0$, $I_{max} = 2$ A; during the period $22.5° \sim 45°$, the currents are set as $I_{O1} = I_{O5} = 0$, $I_{O2} = I_{O6}$ (refer to (3.18)), $I_C = 0.2$ A with $\xi = 0.3$, $I_{max} = 2$ A. Fig. 3.10a shows under the distance from the camera to the stator $Z = -35 \sim -50$ mm, T_{pan} is validated until γ reaches to 0.74 rad. The unreached angles can be achieved by the next set coils. Fig. 3.10b validates (3.24) that the eletromagnetic force in **Z** direction can always balance the

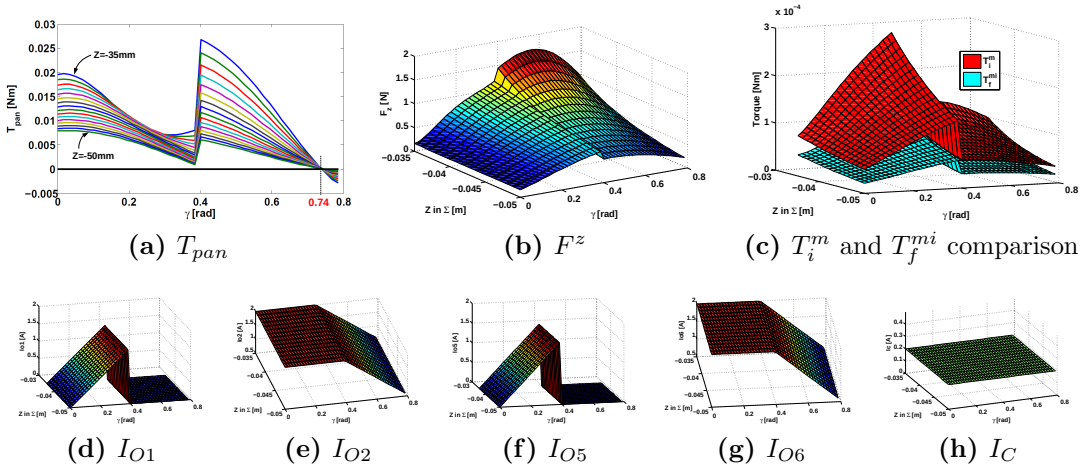

(a) T_{pan} **(b)** F^z **(c)** T_i^m and T_f^{mi} comparison

(d) I_{O1} **(e)** I_{O2} **(f)** I_{O5} **(g)** I_{O6} **(h)** I_C

Figure 3.10: Evaluation of pan motion. (a)-(c) validate the necessary conditions in equations (3.21), (3.22), (3.24) for generating a pan motion. (d)-(h) show the activated coils and input current values.

weight of the camera (assume $G = 30$ grams). Fig. 3.10c validates (3.21) which shows magnetic torque T_i^m on tail-end magnet can overcome the lubricated frictional torque T_f^{mi} between the magnet and its housing.

3.5.5 Tilt Motion Evaluation

The objective of evaluating tilt motion is to analyze the available tilting range constrained by (3.27) and (3.24). The tilt motion has two modes as shown in Fig. 3.4(b) and (c). The central housing is positioned from $\alpha = 0°$ (the magnet is in **Z** direction in Σ) to $\alpha = 90°$ (the central housing counterclockwise rotating around the camera shaft). Each mode is investigated by $Z = -35 \sim -50$ mm. The current setting for this evaluation is shown in Table 3.2. Fig.3.11a and 3.11d illustrate when $Z = -35$ mm, 1.37 rad (78.5°) tilt motion for mode 1 and 1.43 rad (82°) tilt motion for mode 2 are available; and when $Z = -50$ mm, 1.14 rad (65.3°) tilt motion for mode 1 and 1.11 rad (63.6°) for mode 2 are available. The full ranges of tilt motion of mode 1 and mode 2 thus vary from 130.6° to 157° and from 127.2° to 164°

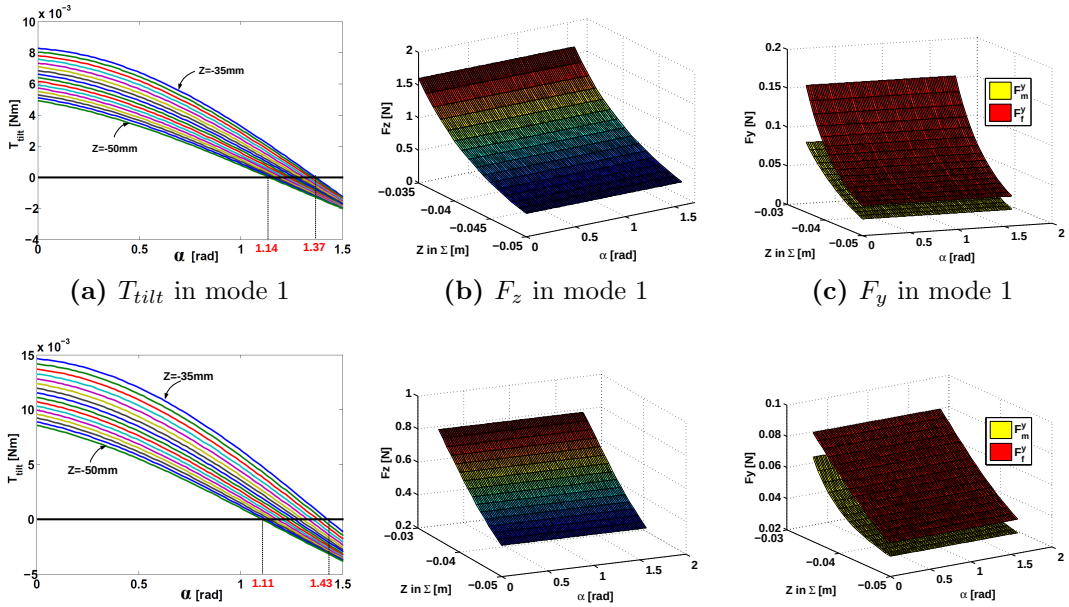

(a) T_{tilt} in mode 1 **(b)** F_z in mode 1 **(c)** F_y in mode 1

(d) T_{tilt} in mode 2 **(e)** F_z in mode 2 **(f)** F_y in mode 2

Figure 3.11: Evaluations of tilt motion. (a)-(c) analyze tilt mode 1, and (d)-(f) analyze tilt mode 2.

Table 3.2: Input Currents For Evaluating Tilt Mode 1 and Mode 2, Unit [A]

	I_{O1}	I_{O2}	I_{O3}	I_{O4}	I_{O5}	I_{O6}	I_{O7}	I_{O8}	I_{I1}	I_{I2}	I_{I3}	I_{I4}	I_{I5}	I_{I6}	I_{I7}	I_{I8}	I_C
Mode 1	1	0	-1	0	1	0	1	0	-2.5	-2.5	-2.5	-2.5	2.5	2.5	2.5	2.5	0
Mode 2	1	1	-1	-1	1	1	1	1	0	-2.5	-2.5	-2.5	0	2.5	2.5	2.5	0

respectively. Fig. 3.11b and 3.11e validate (3.24) with a minimum 0.2 N remaining force after balancing the weight of the camera.

The electromagnetic forces for generating tilt motions cause the tail-end magnets a $\mathbf{Y}_0$ direction (as shown in Fig. 3.5) motion trend by F_f^y. Therefore, it is necessary to compare F_f^y and the sliding friction F_m^y between the camera housings and abdominal wall. Fig. 3.11c and 3.11f show F_f^y is capable to balance F_m^y for keeping the camera in position.

3.6 Summary

This chapter presented a line-arranged rotor driving unit design for a wireless laparoscopic camera. The design applied 17 flatly arranged coils as a stator and three diametrically magnetized cylindrical magnets as a stator. This design features the camera's fixation and manipulation, and enables a decoupled pan and tilt activation of the camera by varying the input current of stator's coils. According to our simulation results, the laparoscopic camera conservatively has the capability to achieve 360° pan motion with a 22.5° resolution, and the range of 127° $\sim$ 164° tilt motion which depends on tilt motion working modes and the distance between the rotor and the stator.

However, the experimental testings of the fabricated design showed that the current control of the 17 coils required a complex algorithm, which caused poor control reliability. To enhance the performance of the actuation system, a hybrid stator which consists of both permanent magnets and coils is introduced in the next chapter.

Chapter 4

Improved Hybrid Stator Design with Line-arranged Driving Unit

4.1 Abstract

This chapter presents an improved hybrid stator design to drive a line-arranged rotor capasulated in laparoscopic cameras. This design features a unified mechanism for anchoring, navigating, and rotating a fully insertable camera by externally generated rotational magnetic field. The insertable camera body, which has no active locomotion mechanism on-board, is capsulated in a one-piece housing with two ring-shaped tail-end magnets and one cylindrical central magnet embedded on-board as a rotor. The stator positioned outside an abdominal cavity consists of both permanent magnets and electromagnetic coils for generating reliable rotational magnetic field. The prototype results in a compact insertable camera robot with a 12.7 mm diameter and a 68 mm length. The design concepts are analyzed theoretically and verified experimentally. The experiments validate that the proposed camera robot design provides reliable camera fixation and locomotion capabilities under various testing conditions. According to the great performance demonstrated in experimental studies, the hybrid stator and the line-arranged rotor are served as the final actuation mechanism design.

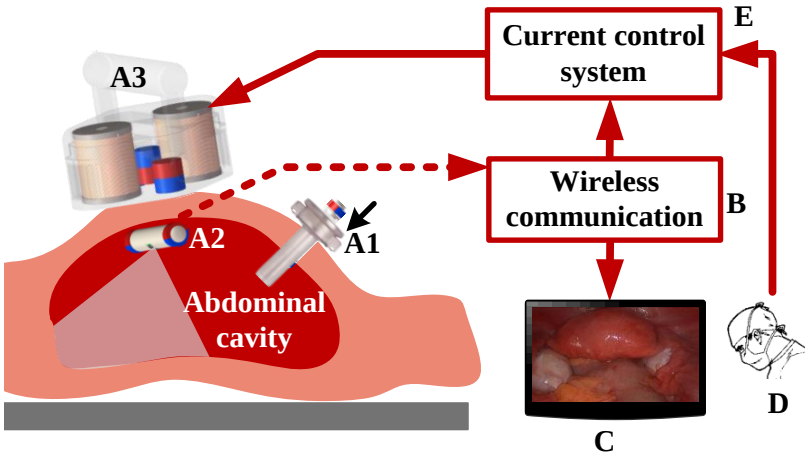

Figure 4.1: Conceptual illustration of the magnetic actuated camera robot. (A1) The process of inserting the camera robot into the patient's abdominal cavity through a trocar. (A2) The initialized position after the camera inserted inside. (A3) The stator. (B) The visual information is transmitted through wireless communication from the camera to the display terminal (C) and current control system (E). (D) A surgeon can control the current input of the stator through current control system (E) for a desired robot pose.

4.2 Line-arranged Rotor Actuation Strategy with Hybrid Stator

4.2.1 Configurations of Hybrid Stator and Rotor Design

The objective of this chapter is to design a unified active locomotion mechanism for a fully insertable wireless laparoscopic camera robot with no on-board motors. As conceptually illustrated in Fig.4.2, the locomotion mechanism consists of (1) a rotor with two tail-end IPMs (tIPMs) and one central IPM (cIPM), and (2) a stator with two coils, two side EPMs (sEPMs), and one central EPM (cEPM). In the stator that placed externally against an abdominal wall, the EPMs and the coils are orthogonally arranged. In the rotor that pushed against an abdominal wall internally, the robot body can rotate freely related to the ring-shaped tIPMs that have unchanged orientations with respect to the stator, and the diametrically magnetized cylindrical cIPM is fixed with the robot body.

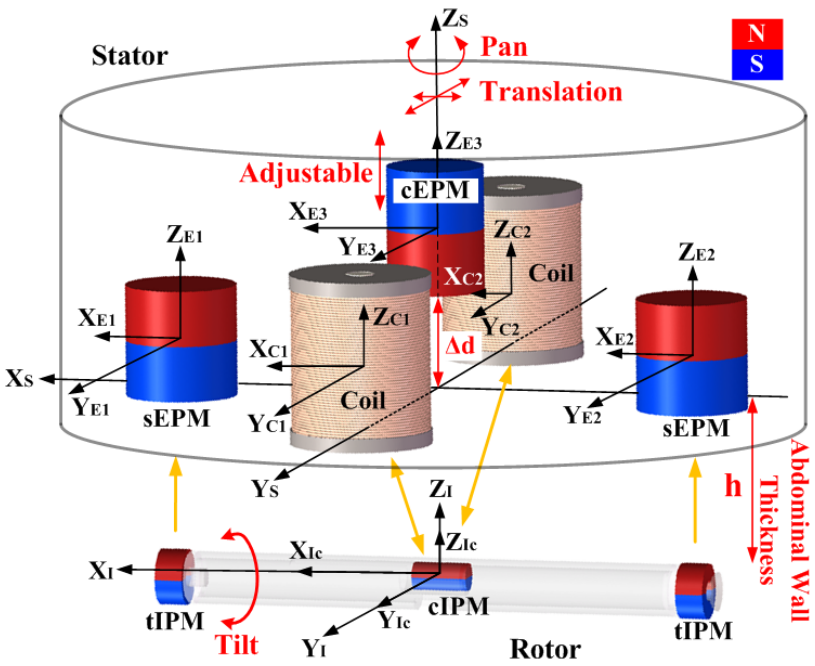

Figure 4.2: The conceptual design of the proposed camera robot system.

The stator-rotor mechanism is designed to enable orientation (rotational control), navigation (translational control), in addition to the compensation of the gravity of the camera (fixation control). The robot orientation consists of pan motion and tilt motion. The pan motion requires torque along Z_I axis of the robot, and the tilt motion control requires torque along X_I axis. The robot navigation requires forces along X_I, Y_I, Z_I axes, with the force along Z_I axis providing fixation of the robot against the abdominal wall. The robot navigation control is provided by moving the stator along the dermal surface with the attractive forces between the sEPMs and the tIPMs. A spinning motion of the stator along Z_S can actuate the robot pan motion by coupling the magnetic field of the sEPMs and the tIPMs. Due to the dominated magnetic field from the sEPMs at the location of the cIPM, the cEPM with its north pole pointing downside is used to eliminate the influence from the sEPMs on the cIPM by adjusting the cEPM displacement along Z_S. In this way, the robot tilt motion can be effectively actuated by the magnetic coupling between the coils and the cIPM.

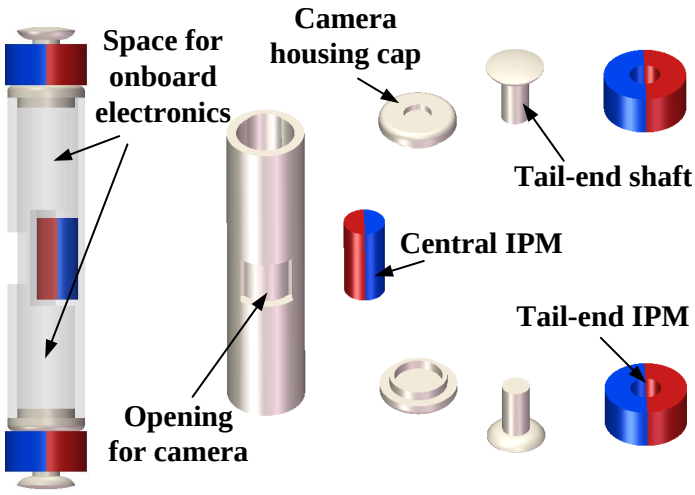

Figure 4.3: Rotor design and its disassembled parts.

The open-ended research problem of chapter is twofold: (1) the effective design of the stator-rotor locomotion mechanism for the camera robot; and (2) the control model of the robot tilt motion. The detailed discussions are presented in Section 4.3 and 4.4.

4.2.2 System Overview

Fig. 4.1 illustrates an application scenario of the proposed laparoscopic camera robot. To insert the camera robot (A1) into the patient's abdominal cavity, a trocar is firstly applied. The robot is introduced into the abdominal cavity with surgical forceps, and fixed against the abdominal wall at an initial position (A2) by a stator (A3). A surgeon (D) sends signals of desired robot poses to the current control system (E) by using a user interface. The camera robot at (A2) sends imaging information to the display terminal (C) through the wireless communication module (B).

4.3 Hybrid Stator Design and Rotor Design

The working environments of the laparoscopic camera robot are insufflated abdominal cavities and abdominal walls. To insert the robot into an abdominal cavity, the

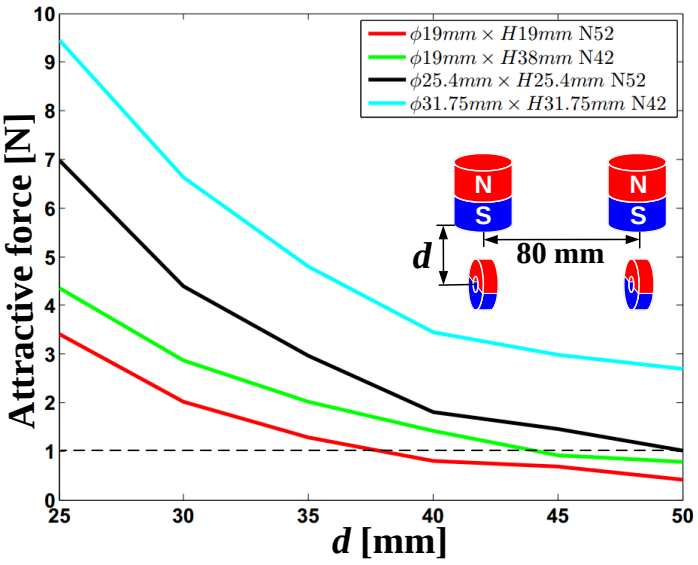

Figure 4.4: Fixation forces are investigated by using four pairs of candidate sEPMs and a pair of tIPMs. The evaluation is conducted under 25 mm $\sim$ 50 mm rotor-to-stator distances and a 80 mm distance between the sEPMs.

diameter of the robot should adapt to the 12 mm $\sim$ 15 mm diameter of a standard trocar. Considering the normal thickness of an abdominal wall that ranges from 20 mm to 40 mm Song et al. (2006), the actuation mechanism design should be able to provide sufficient actuation capabilities under this working range.

4.3.1 Rotor Design

Robot Housing

The robot housing is designed to host on-board electronics and a cIPM by using a 12.7 mm outer diameter (OD), 10 mm inner diameter (ID) tube, as shown in Fig. 4.3. A small cylindrical housing is built in the middle of the tube to fix the cIPM. Two shafts connected with the robot housing caps are designed to support the tIPMs. This design enables the robot housing and the tIPMs to be separate pieces when they rotate along the robot axis. The robot length is an important parameter to be determined, because it affects the torque on the cIPM from the tIPMs. To reserve sufficient space for on-board electronics and avoid overly lengthy device, the candidate

robot length ranges from 50 mm to 100 mm. The final length selection depends on the robot actuation performance, which is described in Section 4.3.2.

Rotor Magnets

The rotor magnets used in the design are diametrically magnetized. The reason to choose this type of magnet is twofold: first, ring-shaped/cylindrical magnets can be well fitted into the capsule-shaped robot; and second, diametrically magnetized magnets can be efficiently actuated by external magnetic fields. Due to the restricted diameter of the robot, two ring-shaped magnets with ODs of 12.7 mm, IDs of 4.75 mm and thicknesses of 6.35 mm are selected to serve as tIPMs to maximize magnetic anchoring performance on the rotor side. The cIPM applies a cylindrical magnet with a 6.35 mm diameter and a 12.7 mm length to fit in the robot housing. Based on the determined parameters of the rotor design, a stator design can thus be studied for optimizing the robot actuation performance.

4.3.2 Stator Design

The stator design is developed to provide reliable magnetic field to manipulate the camera robot for fixation, translation, rotation (pan and tilt motions). Due to the multiple desired actuation functions and the complex composition of the stator magnetic field, which is generated from two coils and three EPMs, the analysis of the stator magnetic design has to be decoupled for each specific actuation function. The key issue of the stator design is to decouple the pan motion and the tilt motion. A cEPM is designed to reduce the dominated magnetic field by the sEPMs in the working space of the cIPM. In this way, the coils are enabled to actuate the tilt motion of the rotor. The fixation, translation, and pan motion are actuated by the magnetic coupling between the sEPMs and the tIPMs.

The stator design follows three steps: first, the sEPMs should be designed to provide sufficient fixation force, translation force, and pan motion torque for the

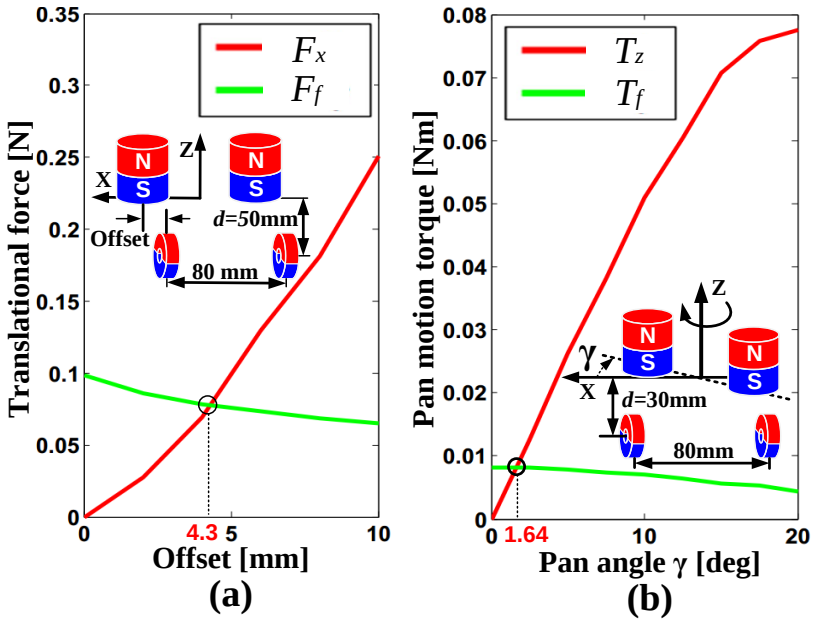

Figure 4.5: Translational force and pan motion torque investigation. (a) The comparison result of translational force F_x between a stator and a rotor in X direction, and frictional force F_f in -X direction with the stator offset distance ranging from 0 mm to 10 mm. (b) The comparison result of the pan motion torque T_z and the frictional torque T_f against the pan motion.

camera robot; second, parameters and configurations of the coils have to be optimized to balance the coil volumes and magnetic field strength; and third, the central axis field of the stator has to be designed by using a cEPM to decouple the pan motion and the tilt motion of the camera robot. The design analysis of the stator in this section is conducted by COMSOL Multiphysics 5.0 (COMSOL Inc., Sweden).

sEPMs of the Stator

According to our preliminary experimental study, a set of axially magnetized cylindrical magnets serve as sEPM candidates. The dimensions and materials of the magnets are illustrated in the legend of Fig. 4.4. To investigate the attractive force between the sEPMs and the tIPMs, the robot length is temporary determined at 80 mm which is approximately the middle point of the desired length range 50 $\sim$ 100 mm. Since the normal range of an abdominal wall thickness is 20 mm $\sim$

40 mm, the range of the rotor-to-stator distance d, which is the distance between the bottom surface of the stator and the symmetric axis of the rotor, is estimated as 30 mm $\sim$ 50 mm. Fig. 4.4 shows the simulation results of the attractive forces between different sets of the sEPMs and the tIPMs under the rotor-to-stator distance ranging from 30 mm to 50 mm. With the estimated the total robot weight that is under 30 g, the magnet with the dimension ϕ25.4 mm $\times$ H25.4 mm, which generates more than 4 N force at 30 mm and 1 N at 50 mm, can provide reliable fixation force with maximum contact compression about 0.5 psi against an abdominal wall. This pressure is much smaller than the safe threshold 3.45 psi for preventing undesired histological damages Best et al. (2011).

Based on the selected sEPMs, the translation and pan motion of the rotor are investigated in Fig. 4.5. Fig. 4.5(a) shows the simulation results of the translational motion with offsets ranging from 0 to 10 mm between the sEPMs and the tIPMs under 50 mm rotor-to-stator distance. The result shows the translational force F_x in X direction can overcome the frictional force F_f in -X direction after the offset distance reaches 4.3 mm. Fig. 4.5(b) shows the sEPMs can provide sufficient pan motion torque T_z along the central axis of the stator to overcome frictional torque T_f after a relative rotational angle $\gamma = 1.64°$ is reached.

Coils of the Stator

The coil dimension design is based on the intensive experimental studies in our prior work Liu et al. (2014a,b) to determine a compact size of the coils, which should compromise with providing sufficient magnetic field strength. The experiments indicate a coil with 50 mm height, 50 mm OD, 10 mm ID, and an iron core with 60 mm height is optimal. The winding wire used in the coils is AWG23 copper wire with 2,000 turns. For the safety consideration, the input current of the coils is limited to 1.5 A for preventing coil overheating.

To optimize the utilization of the coil magnetic field in the robot working space, as illustrated in the yellow area of Fig. 4.6(a), the configurations that include the

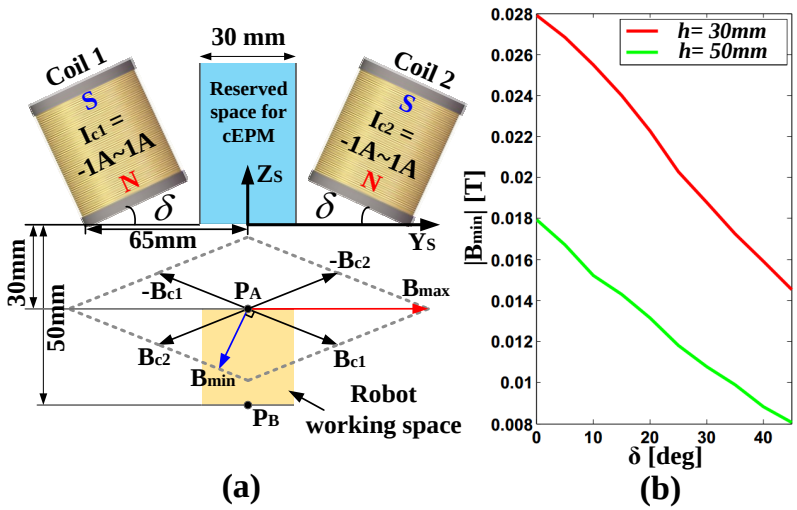

Figure 4.6: Configurations of electromagnetic coils in the stator. (a) The setup for testing the coils δ angle to generate optimal magnetic field in the robot working space. $\mathbf{B}_{min}$ and $\mathbf{B}_{max}$ represent the minimum and the maximum magnetic field strength in a rotational magnetic field generated by the coils. (b) The relationship between the coils tilt angle δ and $\mathbf{B}_{min}$.

distance between the coils, and the tilt angle δ need to be studied. The minimal distance between the two coils is determined by the volume of a cEPM. According to the dimensions of the sEPMs (25.4 mm diameter, 25.4 mm height), a cylindrical space with 30 mm in diameter, as shown in the blue region of Fig. 4.6(a), is reserved for a central EPM to balance the central axis field of the stator. The tilt angle δ of the coils is used to adjust the magnetic field performance. Due to the desire of having a compact stator design, the coil pivot points used to achieve tilt angles are set at $\pm$65 mm on the Y_S axis by considering the 50 mm diameters of the coils.

To determine the optimal δ angle, $\mathbf{B}_{min}$, which is a minimum composed magnetic field by the coils, is used to quantify a δ angle performance. As illustrated in Fig. 4.6(a), $\mathbf{B}_{c1}$ and $\mathbf{B}_{c2}$ are the magnetic fields generated by the coil 1 and the coil 2 respectively. The rhombus demonstrates the region of possible composed magnetic field by setting $-1\,\text{A} \sim 1\,\text{A}$ current input in each coil.

Fig. 4.6(b) shows the $|\mathbf{B}_{min}|$ values at the working space boundary points $\mathbf{P}_A$ and $\mathbf{P}_B$, which represent the rotor-to-stator distance 30 mm and 50 mm respectively. The

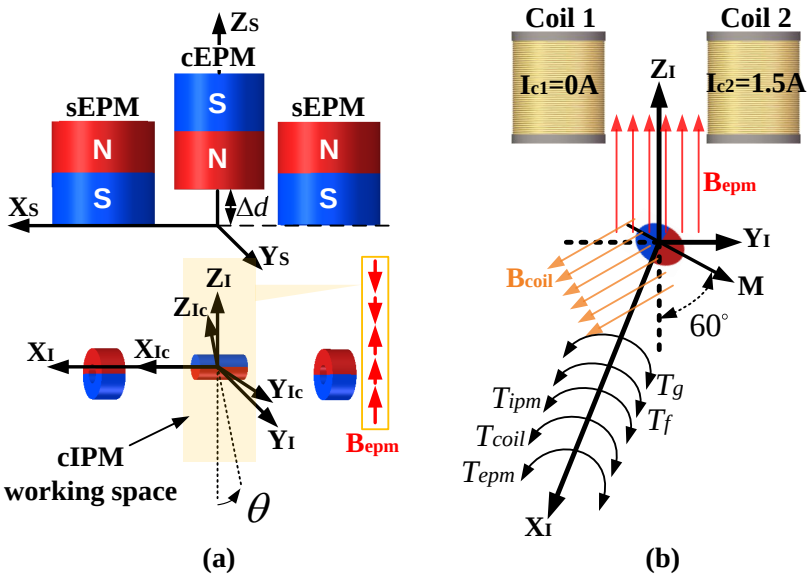

Figure 4.7: Design of the central axis field of the stator. (a) The configuration of the cEPM and the EPMs magnetic field in the working space of the cIPM. (b) The analysis of the central axis field $\mathbf{B}_{epm}$.

magnetic field investigation is conducted by ranging δ angle from 0° to 45°. The simulation results indicate that the optimal tilt angle δ is 0°, which enables the coils to generate the maximum $|\mathbf{B}_{min}|$.

Central Axis Field of the Stator

The purpose of designing the central axis field of the stator is to reduce the dominated field control by the sEPMs, and subsequently enables the coils to actuate the cIPM for tilt motion with an inversely positioned cEPM. The key problem of the central axis field design is to determine an acceptable range of magnetic field strength generated by the EPMs in the cIPM working space, as shown in Fig. 4.7(a). Under the designed range of magnetic field, the coils should be able to actuate the robot to achieve at least 60° tilt motion, which is sufficient for a laparoscopic visualization task.

To estimate the acceptable range of the central axis field $\mathbf{B}_{epm}$, a static torque analysis of the robot tilt motion is conducted by considering the relations between $\mathbf{B}_{epm}$ and T_{epm}. $T_{epm} \in \mathbb{R}^{1\times1}$ is the magnetic torque applied on the cIPM from the

EPMs along X_I axis. We assume the cIPM is described by a body-attached magnetic moment $\mathbf{M} \in \mathbb{R}^{3\times1}$ with a constant magnitude in ampere square meter. The torque and force on the cIPM generated from the stator, in newton meters and newtons respectively, can be expressed as

$$\mathbf{T} = \mathbf{M} \times \mathbf{B}, \quad \mathbf{F} = (\mathbf{M} \cdot \nabla)\mathbf{B}, \tag{4.1}$$

where $\mathbf{B} \in \mathbb{R}^{3\times1}$ represents the magnetic field of the stator Jackson (1999). In accordance with (4.1), T_{epm} can be calculated by

$$T_{epm} = |\mathbf{B}_{epm}| \cdot |\mathbf{M}| \cdot \sin(\widehat{\mathbf{B}_{epm}, \mathbf{M}}). \tag{4.2}$$

To guarantee the robot can achieve at least 60° tilt angle, the boundary condition of T_{epm} is expressed by

$$T_{epm} + T_f \leq T_{coil} + T_{ipm} + T_g, \tag{4.3}$$

where T_f is a frictional torque generated between the abdominal wall and the robot; T_{coil} is the torque on the cIPM with 60° tilt angle by giving input current of the coil 2 as 1.5 A; T_{ipm} is the torque on the cIPM with 60° tilt angle from the tIPMs; T_g is the gravity torque of the robot. The reason to put T_f on the left side of (4.3) is to develop a strict boundary to T_{epm}. The boundary condition (4.3) should be valid under 30 mm $\sim$ 50 mm rotor-to-stator distances. The robot length, which determines the distance between the sEPMs, has a major impact on T_{ipm} and is evaluated in the range of 50 mm $\sim$ 100 mm. Except T_{epm}, all the other torques in (4.3) are calculated by modeling the rotor and the stator in COMSOL. The boundary values of the central axis field $\mathbf{B}_{epm}$ are calculated according to the boundary values of T_{epm} and (4.2), as illustrated in Table 4.1. The minimum boundary value of $|\mathbf{B}_{epm}|$ is 0.0138 T under the condition of the rotor-to-stator distance 50 mm, and the robot

Table 4.1: The Central Axis Magnetic Field Boundary $|\mathbf{B}_{epm}|$ for 50 mm $\sim$ 100 mm Robot Length

Distance (mm)	50	60	70	80	90	100
30	0.0416 T	0.0371 T	0.0361 T	0.0334 T	0.0329 T	0.0328 T
50	0.0219 T	0.0179 T	0.0168 T	0.0143 T	0.0139 T	0.0138 T

length 100 mm. Therefore, the central axis magnetic field of the stator can be bounded as $|\mathbf{B}_{epm}| < 0.0138\,\mathrm{T}$.

Under the guideline of the central axis field boundary developed above, the cEPM can be designed. As illustrated in Fig. 4.7(a), the central axis field $\mathbf{B}_{epm}$ changes its direction as the rotor-to-stator distance increases. To control the tilt motion of the robot, $\mathbf{B}_{epm}$ with $+Z_I$ direction is desired in the cIPM working space as illustrated in Fig. 4.7(b), because the magnetic field with this direction can help the coils to actuate the cIPM for achieving a larger tilt angle. To reserve sufficient space for on-board electronics, the distance between the centers of the tIPMs is determined as 60 mm. The distance between the sEPMs is subsequently determined. By using trial and error method, the cEPM is designed as an axially magnetized cylindrical magnet with 22.22 mm in diameter, 28.57 mm in height, and an offset distance $\Delta d = 5\,\mathrm{mm} \sim 10\,\mathrm{mm}$ in $+Z_S$ direction. The range of the central axis field with the designed central EPM is evaluated by COMSOL under rotor-to-stator distance 30 mm $\sim$ 50 mm. The simulation results in $|\bar{\mathbf{B}}_{epm}| \in [0.0014\,\mathrm{T}, 0.004\,97\,\mathrm{T}]$, which has a uni-directional field point in $+Z_S$ direction, and is within the acceptable central axis field boundary $|\mathbf{B}_{epm}| < 0.0138\,\mathrm{T}$.

Table 4.2 shows the summarized specifications of the rotor and the stator designs. The whole length of the robot is designed as 68 mm in accordance with the determined distance of the tIPMs. The distance of the sEPMs and the distance of the coils, which are 60 mm and 80 mm respectively, are measured between their axial axes.

Table 4.2: Specifications of The Rotor and Stator Prototype Designs

Part Name	Dimension
Central housing	OD 12.7 mm, ID 10 mm
Robot whole length	68 mm
cIPM:	Diametrically magnetized
Size	Diameter 6.35 mm, Length 12.7 mm
Material	NdFeB Grade N42
tIPM:	Diametrically magnetized
Size	OD 12.7 mm, ID 4.75 mm
	Thickness 6.35 mm
Material	NdFeB Grade N42
Dummy robot weight	16.6 g
Electromagnetic coils:	
Dimensions	Height 50 mm, OD 50 mm, ID 10 mm
Axial distance	80 mm
Wire type	AWG23
Turns	2,000
Iron-core dimensions	Diameter 9 mm, Length 60 mm
Iron-core permeability	100,000
sEPMs:	Axially magnetized
Size	Diameter 25.4 mm, Height 25.4 mm
Material	NdFeB Grade N52
Axial distance	60 mm
cEPM:	Axially magnetized
Size	Diameter 22.22 mm, Height 28.57 mm
Material	NdFeB Grade N52
Offset Δd	5 mm$\sim$ 10 mm

4.4 Control Model of Robot Tilt Motion

This section aims at developing a control model for the robot tilt motion activated by the coils. The objective can be achieved by (1) analyzing the stator magnetic field, and (2) modeling the robot dynamics with the magnetic force/torque between the rotor and the stator, and the frictional force/torque between the robot and an abdominal wall.

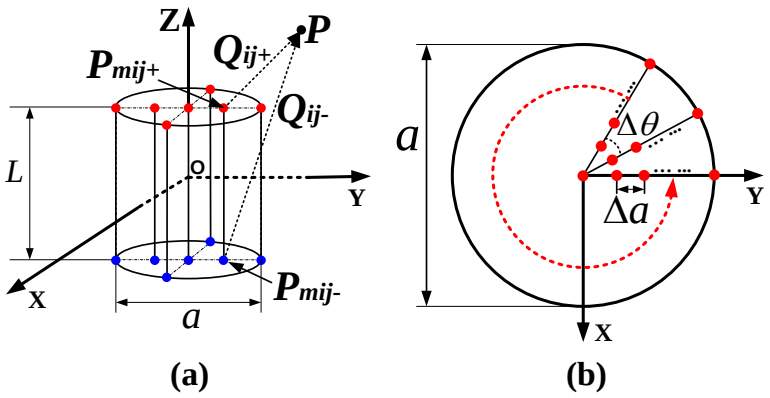

Figure 4.8: EPM magnetic field modeling.

To clarify the relationship between the stator and the rotor, coordinate systems are defined in Fig. 4.2, and explained as follows:

- $\Sigma_{Ei}\{X_{Ei}, Y_{Ei}, Z_{Ei}\}$ represent the coordinate systems of the EPMs, $i = 1, 2, 3$.
- $\Sigma_{Ci}\{X_{Cj}, Y_{Cj}, Z_{Cj}\}$ represent the coordinate systems of the coils, $j = 1, 2$.
- $\Sigma_S\{X_S, Y_S, Z_S\}$ and $\Sigma_I\{X_I, Y_I, Z_I\}$ represent the internal coordinates of the stator and the rotor respectively.
- $\Sigma_{Ic}\{X_{Ic}, Y_{Ic}, Z_{Ic}\}$ represents the body attached coordinate systems of the cIPM.

4.4.1 Magnetic Field Analysis of the Stator

Due to the fixed relative positions of the EPMs and the coils, the stator magnetic field can be calculated by superimposing the magnetic fields from the EPMs and the coils Liu et al. (2014b).

EPM Magnetic Field

Inspired by Kok-Meng and Hungsun (2007), the EPMs can be represented by a magnetic dipole array, as shown in Fig. 4.8(a). The magnetized direction is along +Z axis, and the diameter and length of the magnet are a and L respectively. The positive

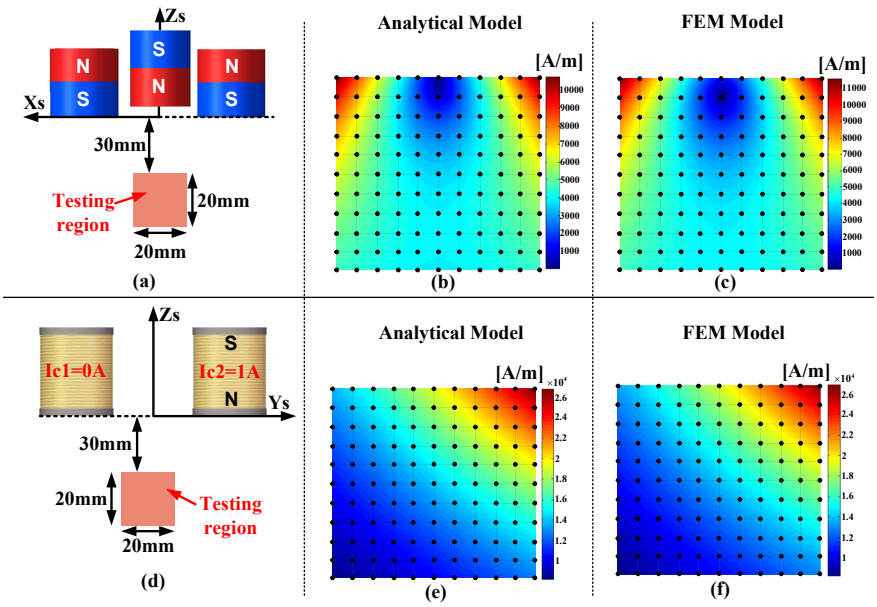

Figure 4.9: Stator magnetic field modeling and evaluations. (a) The configuration for testing the composed magnetic field of the EPMs. (b)-(c) The magnetic fields of the EPMs in the testing region of (a) calculated by the magnetic field model and a FEM model separately. (d) The configuration for testing the magnetic field of the coils. In this setting, only the right coil is activated with a unit-current input. (e)-(f) The magnetic fields of the coil in the testing region of (d). (e) is generated by the magnetic field model, and (f) is developed by a FEM model. The black dots in (b), (c), (e), (f) represent the sampled data for quantitatively comparing the results from the magnetic field model and the FEM model.

and negative magnetic charges are distributed on the top and bottom surfaces. The number and the arrangement of the magnetic changes on the surfaces determine the accuracy of the magnetic field model. Fig. 4.8(b) shows the magnetic charge arrangement on one surface. Eleven magnetic changes are evenly sampled starting at (x=0, y=0), along +Y direction. The interval distance Δa between two adjacent charges is calculated as $a/10$. Then the magnetic charge sampling line on +Y axis rotates around Z axis with a sampling interval angle $\Delta\theta$ as $\pi/6$. Because the 121 magnetic charges are symmetrically distributed around Z axis, only a quarter of the magnetic dipoles need to be estimated by the fitting data, which is obtained from FEM numerical magnetic field results.

By summarizing all the magnetic dipoles, the magnetic flux density of an EPM is expressed as

$$\mathbf{B}_e = \frac{\mu_0}{4\pi} m_0 \Gamma_{00} + \frac{\mu_0}{4\pi} \sum_{i=1}^{K_m} \sum_{j=1}^{N_m} m_{ij} \Gamma_{ij}, \tag{4.4}$$

$$\Gamma_{ij} = \frac{\mathbf{Q}_{ij+}}{|\mathbf{Q}_{ij+}|^3} - \frac{\mathbf{Q}_{ij-}}{|\mathbf{Q}_{ij-}|^3}, \tag{4.5}$$

where m_{ij} is the strength of the ij^{th} magnetic dipole, and m_0 is the strength of the magnetic dipole at the center; $K_m = 10$ denotes the number of magnetic dipoles radially, and $N_m = 12$ is the number of magnetic dipoles for a single loop; $\mathbf{Q}_{ij+/-}$ represents a vector from the location of positive/negative magnetic charge $\mathbf{P}_{mij+}/\mathbf{P}_{mij-}$ to a point $\mathbf{P}$ in space.

Coil Magnetic Field

It has been experimentally proved in Kummer et al. (2010) that the magnetic flux density of an iron-core coil has a linear relationship with its input current. To develop the magnetic field model for an iron-core coil, Kummer et al. (2010) estimates the parameter with one pair of magnetic dipoles by using the magnetic field data generated from FEM solutions of a unit-current coil. Compared with a single pair of magnetic dipoles, a multiple-dipole model, which has been used for estimating EPM models above, has more abilities to achieve an accurate model. Thus, to derive the model of the magnetic field of an iron-core coil, (4.4) is applied to estimate a unit-current magnetic field. The relationship between an input current of a coil and the generated magnetic flux density is formulated by

$$\mathbf{B}_c = \mathbf{B}_c^u I_c, \tag{4.6}$$

where $\mathbf{B}_c^u$ has the same formulation as $\mathbf{B}_e$ in (4.4), but the fitting data is generated from a unit-current coil; I_c is the input current of the coil.

Superimposed Magnetic Field

Since the magnetic field models of the EPMs and the coils are separately developed, a superimposed magnetic field of the stator can thus be formulated. Recalling the coordinate systems demonstrated in Fig. 4.2, $\mathbf{R}_{Ei}, \mathbf{T}_{Ei}$ and $\mathbf{R}_{Cj}, \mathbf{T}_{Cj}$ represent the rotational matrices and translational vectors from Σ_S to Σ_{Ei} and from Σ_S to Σ_{Cj} respectively. The superimposed magnetic field of the stator can be expressed in (4.7) by using (4.4) and (4.6):

$$\mathbf{B}_s(\mathbf{P}_s) = \sum_{i=1}^{3} \mathbf{R}_{Ei}\mathbf{B}_e^i(\mathbf{P}_i) + \sum_{j=1}^{2} \mathbf{R}_{Cj}\mathbf{B}_c^u(\mathbf{P}_j)I_{cj} \tag{4.7}$$

where $\mathbf{B}_e^i$ denotes the magnetic flux density of the i^{th} EPM; $\mathbf{P}$ represents coordinates in frame Σ_S; $\mathbf{P}_i$, $\mathbf{P}_j$ are the transferred coordinates of $\mathbf{P}_s$ from Σ_S to Σ_{Ei} and Σ_{Cj} by using $\mathbf{P}_i = \mathbf{R}_{Ei}^T\mathbf{P}_s - \mathbf{R}_{Ei}^T\mathbf{T}_{Ei}$ and $\mathbf{P}_j = \mathbf{R}_{Cj}^T\mathbf{P}_s - \mathbf{R}_{Cj}^T\mathbf{T}_{Cj}$.

To investigate the validity of the model of the stator magnetic field, the configuration of the stator adopted the designed parameters in Table 4.2 with $\Delta d = 5\,\text{mm}$. Considering the working space of the cIPM, $20\,\text{mm} \times 20\,\text{mm}$ magnetic field testing regions were designed on both the $X_S Z_S$ plane and the $Z_S Y_S$ plane for validating the EPM field and the coil field respectively, as shown in Fig. 4.9(a) and (d). The comparison results of the EPMs magnetic field generated by the our developed model and a FEM model are shown Fig. 4.9(b) and (c). Similarly, Fig. 4.9(e) and (f) show the comparison results of the magnetic field generated from the unit-current coil by using the magnetic field model and a FEM model separately. To evaluate the results quantitatively, the sampled magnetic field data, which are the black dots shown in Fig. 4.9(b)(c) and (e)(f), were applied with 2 mm intervals in the testing regions for both the EPMs and the coil. The average errors for the comparison results of the EPMs and the coils are 7.85% and 1.23% respectively. The accuracies of developed magnetic field models were further improved by providing more experimental data for (4.4) and (4.6) in Section 4.5.2.

4.4.2 Control with Electromagnetic Coils

The robot tilt motion is activated by the magnetic coupling between the coils and the cIPM. I_{c1} and I_{c2} are represented as the current inputs of the coils, and θ is represented as the rotational angle of the robot tilt motion. The robot dynamics need to be studied for developing the relationship between the control inputs I_{c1}, I_{c2} and the output θ.

Fig. 4.7(b) shows the dynamic analysis of the robot tilt motion. The torques that affect the tilt motion along X_I include (1) T_s which is the combination of T_{epm} and T_{coil} on the cIPM from the EPMs and the coils of the stator; (2) T_{ipm} which is the magnetic torque on the cIPM from the tIPMs along X_I; (3) T_f and T_g which are the frictional torque of the robot-tissue interaction and the torque due to the robot gravity along X_I. The bold fonts $\mathbf{T}_s, \mathbf{T}_{ipm}, \mathbf{T}_f$, and $\mathbf{T}_g$ are used to represent the torque vectors with the components along X_I, Y_I, Z_I.

Combining (4.1) and (4.7), the torque on the cIPM generated from the stator, in newton meters, can be expressed as

$$\mathbf{T}_s = \underbrace{\mathbf{M} \times (\sum \mathbf{R}_{Ei}\mathbf{B}_e^i)}_{\mathbf{E}} + \underbrace{(\mathbf{M} \times \mathbf{R}_{C1}\mathbf{B}_c^u)}_{\mathbf{C}_1} I_{c1} + \underbrace{(\mathbf{M} \times \mathbf{R}_{C2}\mathbf{B}_c^u)}_{\mathbf{C}_2} I_{c2}, \tag{4.8}$$

where $\mathbf{E} \in \mathbb{R}^{3\times1}$ denotes the torque from the EPMs, i=1,2,3; $\mathbf{C}_1 \in \mathbb{R}^{3\times1}$ and $\mathbf{C}_2 \in \mathbb{R}^{3\times1}$ denote the unit current torques from the coils. Benefiting from the magnetic field model in (4.4), $\mathbf{E}$, $\mathbf{C}_1$, and $\mathbf{C}_2$ can be computed in real time.

The non-zero components in $\mathbf{T}_f$ and $\mathbf{T}_{ipm}$ are the x-components represented by T_f and T_{ipm}. T_f is determined by F_{attr} which is the attractive force between the stator and the rotor. Due to the reduced magnetic field of the EPMs in the cIPM working space, the magnetic coupling between the stator and the central IPM has a minor contribution which is less than 7% of the total attractive force according to our simulation. To reduce the complexity of the system control, this trivial contribution of the attractive force F_{attr} is neglected. As $F_{attr} = f_1(h)$ and $T_{ipm} = f_2(\theta)$ are

functions of an abdominal wall thickness h and the robot tilt angle θ respectively, f_1 and f_2 can be modeled by polynomial approximation

$$f_1(h) = \sum_{k=1}^{n+1} \eta_k h^{n-k+1}, \quad f_2(\theta) = \sum_{k=1}^{m+1} \xi_k \theta^{m-k+1}, \tag{4.9}$$

where η_k and ξ_k are the polynomial coefficients to be determined by experimental data; n and m denote the degrees of f_1 and f_2.

By representing $\boldsymbol{\omega} = [\dot{\theta}, 0, 0]^T$ as the angular velocity of the robot tilt motion, the dynamic model can be formulated in Σ_I as

$$\mathbf{T}_s + \mathbf{T}_{ipm} + \mathbf{T}_f + \mathbf{T}_g = \mathbf{I}'\dot{\boldsymbol{\omega}} + \boldsymbol{\omega} \times \mathbf{I}'\boldsymbol{\omega}, \tag{4.10}$$

where $\mathbf{I} \in \mathbb{R}^{3\times3}$ is the moment of inertia in the body attached frame Σ_{I_c}; $\mathbf{R}_I^{I_c} \in \mathbb{R}^{3\times3}$ is the rotational matrix from Σ_I to Σ_{I_c}; $\mathbf{I}' = \mathbf{R}_I^{I_c} \cdot \mathbf{I} \cdot (\mathbf{R}_I^{I_c})^T$ is the moment of inertia of the rigid body in Σ_I.

Since the tilt motion is actuated along the X_I axis, only the x components need to be considered in (4.10). By substituting (4.8) and (4.9) in (4.10), the dynamic equation is reformulated as

$$E_x + C_{1x}I_{c1} + C_{2x}I_{c2} + T_{ipm} + \mu(F_{attr} - mg)r_f + mgr_g \sin\theta = a_{11}\ddot{\theta}, \tag{4.11}$$

where E_x, C_{1x}, C_{2x} are the x components in $\mathbf{E}, \mathbf{C}_1$, and $\mathbf{C}_2$ respectively; μ is the frictional coefficient between the robot and an abdominal wall; mg represents the gravity of the robot; r_f and r_g denote the lever arms of the friction force and the gravity force to generate T_f and T_g; a_{11} denotes the element of 1^{th} row, 1^{th} column in $\mathbf{I}$;

To generate a desired tilt angle for the robot, the coil current inputs I_{c1} and I_{c2} can be found by applying pseudoinverse to

$$\mathbf{C}_x\mathbf{I}_c = G, \tag{4.12}$$

where $\mathbf{C}_x = [C_{1x}, C_{2x}] \in \mathbb{R}^{1\times 2}$; $\mathbf{I}_c = [I_{c1}, I_{c2}]^T \in \mathbb{R}^{2\times 1}$; G represents the summation of the remaining terms in (4.11). Because $\mathbf{C}_x$ has a full row rank, the solution of the current input vector $\mathbf{I}_c$ can be calculated by using

$$\mathbf{I}_c = \mathbf{C}_x^T(\mathbf{C}_x\mathbf{C}_x^T)^{-1}G. \tag{4.13}$$

4.5 Prototype Fabrication and Experimental Validation

4.5.1 Prototype Fabrication and Experiment Platform Setup

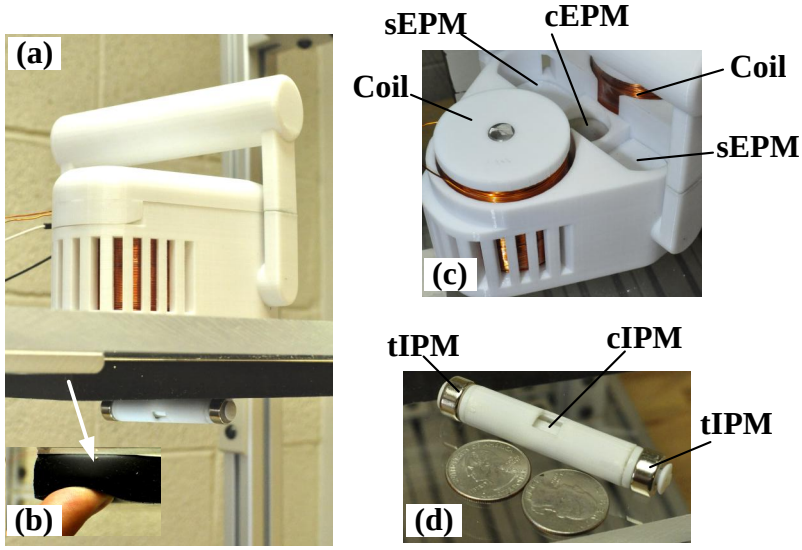

Figure 4.10: Experimental environment and the fabricated capsule robot system: (a) experiment setups for evaluating the robot locomotion capabilities; (b) the simulated abdominal wall tissue made by a viscoelastic material; (c) the stator design; (d) the rotor design.

Experiment platform setup

Fig. 4.10(a) shows the overview of the experimental environment. The robot system was fabricated by a 3D prototyping machine (Fortus 400mc, Stratasys Inc.). To

simulate the viscoelastic properties of a real insufflated abdominal wall (average Young's modulus 32.5 kPa) Song et al. (2006), a viscoelastic material Durometer 40 with (Young's modulus 27.57 kPa at 15% deflection, Sorbothane, Inc.) was applied as illustrated in Fig. 4.7(b). The initial abdominal wall thickness was 26 mm (tissue layer 15 mm, support layer 11 mm), which can be adjusted by increasing the distance between the stator and the support layer. The vertical displacement Δd of the cEPM can be manually adjusted at this stage. A silicone oil lubricated rotor-tissue contact layer was added to the bottom of the viscoelastic material for mimicking an internal abdominal wall surface.

Rotor and stator fabrication

Fig. 4.10(c) and (d) show the prototype of the camera robot and the stator. The specifications of the stator and rotor designs are illustrated in Table 4.2. The permanent magnets applied in the prototype are all from K&J Magnetics. The AWG23 cooper wires adopted in the coils are from TEMCo. And the iron-cores of the coils are made by EFI Alloy 50 from Ed Fagan. The space above the EPMs in the stator is reserved for the on-board electronics and the tetherless power supply of the stator.

Current control system

A tethered current control system was developed by the PWM technique. The system consists of a micro-controller (STM32F4Discovery, STMicroelectronics Inc.) to generate PWM signals, two PWM amplifiers (L6205 DMOS Full Bridge Driver, STMicroelectronics Inc.) to amplify the signals, a power supply for powering up the amplifiers, and a PC computer to send control command to the micro-controller via a serial communication.

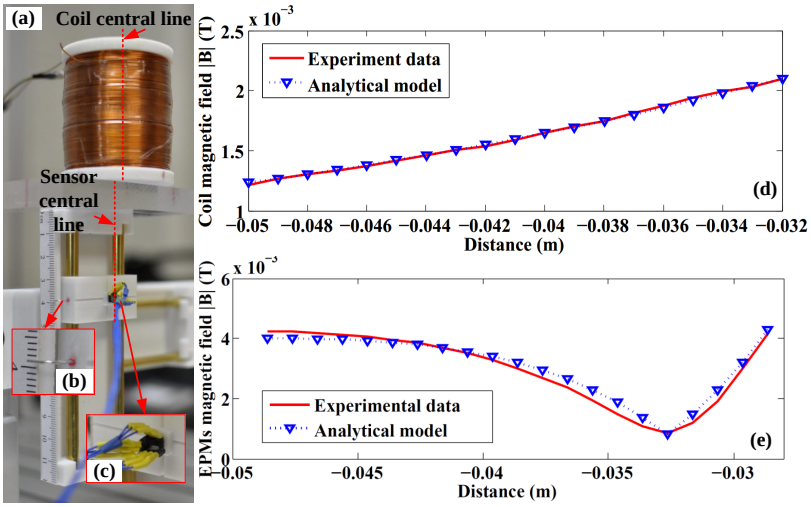

Figure 4.11: Stator magnetic field experimental evaluation.

4.5.2 Model Evaluation

Stator magnetic field

The models of the stator magnetic field developed in Section 4.4.1 were validated by using hall effect sensors (CYL8405, ChenYang Technologies GmbH) with measuring range $0 \sim 64\,\text{mT}$ and sensitivity about $50\,\text{mV/mT}$. The measured analog magnetic field signals were converted to digital signals with sensing resolution $0.01\,\text{mT}$ by using a 16bit ADC (ADS1115, Texas Instruments Inc.). Due to the imperfection of the coil wrapping, the iron cores, and the permanent magnets, model calibration was performed by using experimental data. Fig. 4.11(a) shows the experiment platform for magnetic field validation which consists of a vertical moving track with a position indicator (Fig. 4.11(b)), three hall effect sensors for 3-axis sensing (Fig. 4.11(c)), and a transparent support board for placing the coils or the EPMs at desired locations. Fig. 4.11(d) and (e) show the magnetic flux density norm comparison results of the experimental data and the magnetic field models along the sensor central line for a single coil with unit current input and the three EPMs with the vertical displacement of the cEPM as $\Delta d = 1\,\text{mm}$. According to the configuration of the stator, the distance from the coil central line to the sensor central line was set as $40\,\text{mm}$ for validating

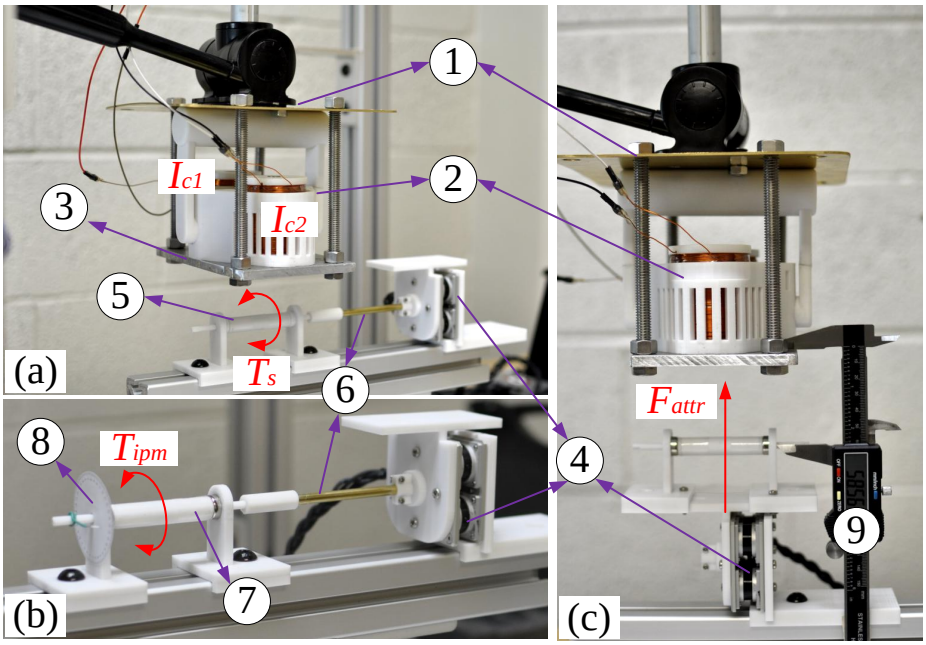

Figure 4.12: Experiment configurations for evaluating the model of T_s in (a), estimating the polynomial coefficients of T_{ipm} in (b) and F_{attr} in (c). ①: stator lifting mechanism; ②: the stator; ③: the stator supporting board made by aluminum; ④: six axis force/torque sensor; ⑤: camera housing with the cIPM inside, and without the tIPMs at the tail-ends; ⑥: shaft; ⑦: camera housing with the cIPM inside, and with the tIPMs at the tail-ends; ⑧: tilt angle indicator; ⑨: caliper for measuring the stator-to-rotor distance.

the coil magnetic field. For the EPMs, the sensor central line was set to coincide with the central line of the cEPM. The average errors of the magnetic field models demonstrated in Fig.4.11(d) and (e) were 0.001% and 0.02% respectively.

Table 4.3: Magnetic Torque Between tIPMs and cIPM T_{ipm}

θ (deg)	0	15	30	45	60	75	90
T_{ipm} (mNm)	0	-0.76	-1.23	-1.53	-1.68	-1.85	-1.96

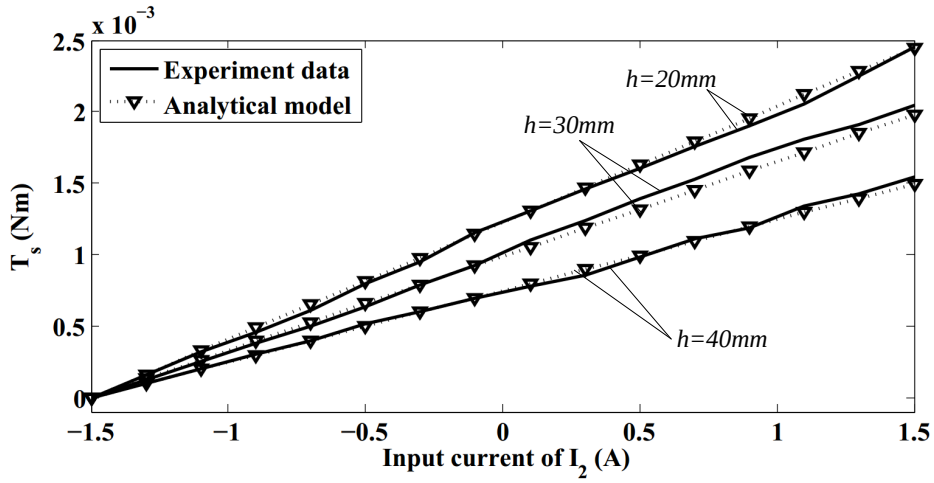

Figure 4.13: Experimental evaluation of magnetic torque on the cIPM.

Magnetic torque on the cIPM

Fig. 4.12(a) shows the experimental setup for evaluating $\mathbf{T}_s$ in (4.8). Due to the tilt motion generated along the camera axis, T_s which is the x component of $\mathbf{T}_s$ was measured by changing the current inputs of the coils I_{c1} and I_{c2}. A six axis force/torque(F/T) sensor (HEX-58-RB-2000N, OptoForce Inc.), as illustrated in Fig. 4.12(a)-④ with torque resolution 5×10^{-4} Nm along the shaft was applied. A cIPM was embedded in the camera housing (Fig. 4.12(a)-⑤) which was connected to the F/T sensor with a shaft (Fig. 4.12(a)-⑥). The tilt angle of the camera housing was fixed at 0°. The distance h between the stator and the camera was adjusted by a lifting mechanism (Fig. 4.12(a)-①), and measured by a caliper (Fig. 4.12(c)-⑨). An aluminum board was used at the bottom surface of the lifting mechanism ((Fig. 4.12(a)-③) with relative magnetic permeability about 1. The input current I_{c1} was fixed at -1.5 A, while I_{c2} was linearly changed from -1.5 A to 1.5 A. Fig. 4.13 shows the comparison results of experiment data and the model in (4.8) under stator-to-rotor distances 20 mm, 30 mm, and 40 mm. The average error of the model demonstrated in Fig. 4.13 was 0.0035%.

Table 4.4: Stator/Rotor Attractive Magnetic Force

h (mm)	Δd (mm)	$F_{attr}(N)$	ΔF (N)
20	11	3.978	±0.034
25	8	2.590	±0.034
30	4	1.626	±0.034
35	2	0.916	±0.034
40	1	0.544	±0.034
45	0	0.442	±0.034
50	0	0.340	±0.034

Polynomial coefficients estimation

Fig. 4.12(b) shows the experimental setup for measuring the magnetic torque T_{ipm} to estimate the polynomial coefficients in (4.9). Compared with the configuration of the camera housing in Fig. 4.12(a)-⑤, the configuration in Fig. 4.12(b)-⑦ applied two tIPMs with fixed orientations at both ends of the camera housing. The tilt angle of the cIPM was indicated by an angle indicator as illustrated in Fig. 4.12(b)-⑧. After a tilt angle was set, the shaft at the sensor side was fastened by the screws to hold the angle.

Table 4.3 shows the T_{ipm} experiment data by changing the tilt angle from 0 to 90° with 15° interval. The estimated polynomial coefficients for T_{ipm} are $\xi_1 = 0.0247$, $\xi_2 = -0.1176$, $\xi_3 = 0.2298$, $\xi_4 = -0.4801$, $\xi_5 = -1.5159$ with a fitting error 0.76% at the fourth degree polynomial ($m = 4$ in (4.9)).

Fig. 4.12(c) demonstrates the experimental setup for measuring the magnetic attractive force F_{attr} to estimate the polynomial coefficients in (4.9). Table 4.4 shows

the attractive force F_{attr} between the stator and the rotor with respect to stator-to-rotor distance h sampled from 20 mm to 50 mm. The values in the column of Δd show the optimal displacements of the cEPM that enable minimal magnetic field from the EPMs on the cIPM. ΔF represents the maximum influence on the attractive force by activating the coils in the stator. The experiment data validates that the magnetic force contribution from the coils is minor compared with the magnetic force from the EPMs. A fourth degree polynomial curving fitting ($n = 4$ in (4.9)) was applied for F_{attr} to achieve a curve fitting error 1.66% with the coefficients $\eta_1 = -0.0498$, $\eta_2 = -0.1143$, $\eta_3 = 0.7364$, $\eta_4 = -1.0856$, $\eta_5 = 0.9237$.

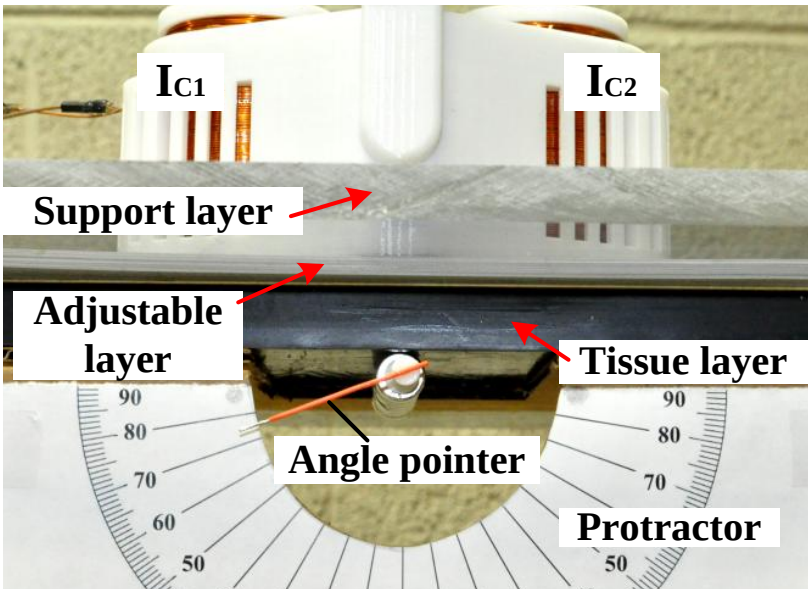

Figure 4.14: Experimental setup for open-loop control of the camera tilt motion.

4.5.3 Open-loop Control of Tilt motion

Fig. 4.14 shows the experimental setups for the camera robot tilt motion control by using (4.11). The simulated abdominal wall consisted of three types of layers: (1) the tissue layer lubricated with silicone oil; (2) support layer; and (3) adjustable layer which was used for changing the total thickness of the abdominal wall. To indicate the tilt angles, a protractor and an angle pointer were applied.

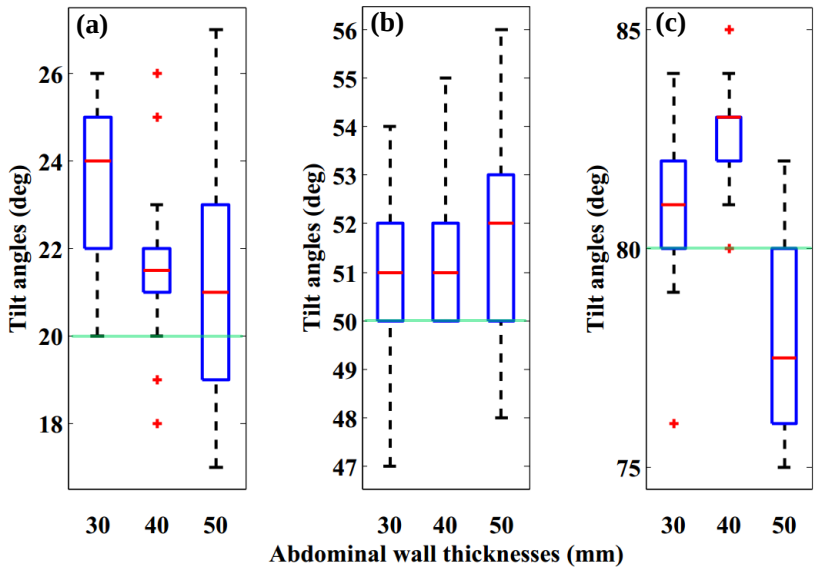

Figure 4.15: Experimental results of the open-loop control of tilt motion. (a) Desired tilt angle $\theta_d = 20°$; (b) $\theta_d = 50°$; (c) $\theta_d = 80°$.

Considering the candidate on-board electronics to be integrated in the camera robot, the moment of inertia matrix $\mathbf{I}$ of the robot was estimated by modeling it in SolidWorks2013 (Dassault Systémes SolidWorks Corp.) as

$$\mathbf{I} = \begin{pmatrix} 0.174 & 0 & -0.003 \\ 0 & 3.473 & 0 \\ 0 & 0 & 3.469 \end{pmatrix}, \tag{4.14}$$

where the unit of each element in $\mathbf{I}$ is $\mathrm{kg\,mm^2}$. The other parameters used in (4.11) were estimated or measured as $\mu = 0.1$, $r_f = 4\,\mathrm{mm}$, and $r_g = 1.5\,\mathrm{mm}$. Extra weights were filled in the camera housing to simulate the full load of on-board electronics with the total weight of the camera robot as $mg = 0.26\,\mathrm{N}$.

To control the tilt motion with (4.11), 5th-order desired trajectories, which are smooth at the angular acceleration level, were generated by initializing the robot tilt angles as 0° and setting the desired tilt angles θ_d. The control current inputs I_{c1} and I_{c2} were computed by (4.13) in real time.

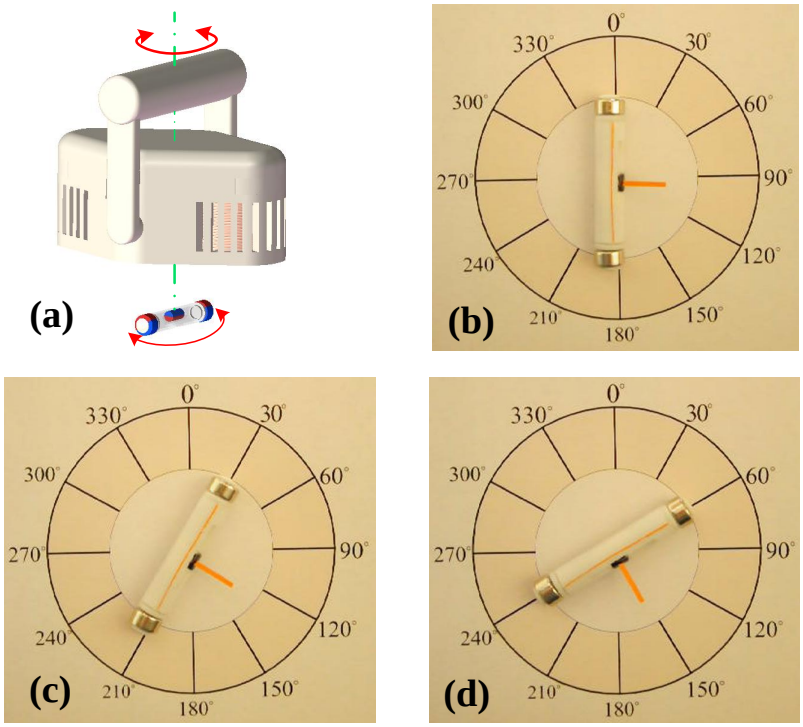

Figure 4.16: Demonstration of decoupled pan and tilt motion.

Fig. 4.15 shows the experimental results of open-loop control of the camera tilt motion by setting the desired tilt angles as 20°, 50°, and 80° which are illustrated by the green lines in Fig. 4.15(a), (b), and (c) respectively. This experiment was grouped by 30 mm, 40 mm, and 50 mm abdominal wall thicknesses. For each group and each desired tilt angle, the control process was implemented by 30 trials. The box-and-whisker plots indicate that the tilt angle errors fell in ±7°. The tilt angle control for $\theta_d = 50°$ in Fig. 4.15(b) was better behaved than in (a) and (c) with no single sample considered as extremes. Fig. 4.15(c) demonstrates that camera tilt angle can be successfully controlled up to 80° which is sufficient for visualization tasks of abdominal cavities.

4.5.4 Decoupled Pan and Tilt Motion

Fig. 4.16 shows the decoupled the robot pan and tilt motion by setting a fixed 60° tilt angle, while generating the pan motion. Fig. 4.16(a) illustrates the rotational

axis of the stator for pan motion. To demonstrate the fixed tilt angle, orange makers were attached on the robot. Fig. 4.16(b)-(d) show the sampled pan angles with a 30° sampling interval from 0° to 60°, while the pan motion is continuously generated.

4.6 Summary

In this chapter, an innovative hybrid stator was developed for generating reliable rotational magnetic field to actuate a a fully insertable laparoscopic camera robot, which consists of an improved line-arranged rotor design. Fixation, translation and rotation functions are unified into a capsule design of insertable body, which is controlled by adjusting rotational magnetic field from the stator. The experiment investigations showed that the system provide reliable anchoring, translation, 360° continuous pan motion control, and fine tilt motion control up to 80° under the conditions of 30 mm $\sim$ 50 mm simulated abdominal wall thicknesses. Pan and tilt motion can be simultaneously controlled in a decoupled way, which enables a flexible motion control of the camera robot to illuminate and visualize a target surgical area.

Chapter 5

Closed-loop Control of the Robotic Camera System

5.1 Abstract

This chapter demonstrates a magnetic actuated robotic surgical camera system with two-degree-of-freedom (2-DOF) orientation control for single incision laparoscopic surgery. The design of the camera system that consists of a stator and a rotor features a unified mechanism for anchoring, navigating, and rotating the insertable camera (rotor) by externally generated rotational magnetic field from the stator. The insertable camera that has no on-board active locomotion mechanism is capsulated in a one-piece housing with two ring-shaped tail-end magnets and one cylindrical central magnet as the rotor. The stator positioned outside an abdominal cavity consists of both permanent magnets and electromagnetic coils to generate rotational magnetic field. A closed-loop control system was developed to enable autonomous fine orientation control (tilt motion and pan motion) of the camera. The experimental investigations indicated that the camera can achieve 0.67° and 0.49° control accuracies in tilt and pan motions respectively. The combined orientation control in three-dimensional space demonstrated less than 1° control accuracy.

5.2 Problem Description of Camera Orientation Control

As illustrated in Fig. 4.2, the magnetic actuation mechanism of the camera robot consists of (1) a rotor with two tail-end IPMs (tIPMs) and one central IPM (cIPM), and (2) a stator with two coils, two side EPMs (sEPMs), and one central EPM (cEPM). In the stator that placed externally against an abdominal wall, the EPMs and the coils are orthogonally arranged. In the rotor that pushed against an abdominal wall internally, the robot body can rotate freely related to the ring-shaped tIPMs , and the diametrically magnetized cylindrical cIPM is fixed with the robot body.

The stator-rotor mechanism is designed to enable orientation (rotational control), navigation (translational control), in addition to the compensation of the gravity of the camera (fixation control). The robot orientation consists of pan motion and tilt motion. The pan motion requires torque along Z_I axis of the robot, and the tilt motion control requires torque along X_I axis. The robot navigation requires forces along X_I, Y_I, Z_I axes, with the force along Z_I axis providing fixation of the robot against an abdominal wall. The robot navigation control is provided by moving the stator along the dermal surface with the attractive forces between the sEPMs and the tIPMs. A spinning motion of the stator along Z_S can actuate the robot pan motion by coupling the magnetic field of the sEPMs and the tIPMs. Due to the dominant magnetic field from the sEPMs at the location of the cIPM, the cEPM with its north pole pointing downside is used to eliminate the influence from the sEPMs on the cIPM by adjusting the cEPM displacement along Z_S. The cEPM displacement is adjusted according to an abdominal wall thickness for minimizing the magnetic field from the EPMs on the cIPM. In this way, the camera tilt motion can be actuated by the magnetic coupling between the coils and the cIPM.

The research objective of this work is to enable automatic control of the camera robot's tilt motion and pan motion. To control the tilt motion, the cEPM

displacement Δd has to be firstly adjusted in accordance with the thickness of an abdominal wall h at the current stator location. In our prior work Liu et al. (2015), the optimal displacements of the cEPM Δd with respect to different abdominal wall thicknesses h were formulated in $\Delta d = f(h)$, which is a function represented by a lookup table with h as a variable. The ***first research task*** of this paper is to develop an abdominal wall thickness estimation method with an automatic cEPM displacement mechanism. Based on this step, our ***second research task*** is to developed a closed-loop tilt motion control scheme for the camera robot by controlling the current inputs of the coils with an on-board tilt angle feedback sensing module. To control the pan motion of the camera robot, the stator has to be rotated externally to generate rotational magnetic coupling with the tIPMs in the camera robot. This function was achieved manually in our previous prototype. In this work, the ***third research task*** is to design a pan motion mechanism in the stator for achieving automatic pan motion control of the camera robot.

5.3 Control Method of Magnetic Actuation Mechanism

Fig. 5.1 illustrates the orientation control architecture of the camera robot. The system initialization is firstly executed by estimating the abdominal wall thickness and adjusting the displacement of the cEPM according to the rotor-to-stator distance when the stator is repositioned to new locations on an abdominal wall. The input parameters of the control system are the desired tilt angles θ_d and pan angles ϕ_d. For tilt motion, the output angle θ is controlled by the calculated input currents I_{c1} and I_{c2} of the coils. A tri-axis accelerometer embedded in the camera robot is applied for providing the tilt angle feedback. The details of the tilt motion control are illustrated in Fig. 5.6. The pan motion output angle ϕ is controlled by an actuation mechanism design presented in Section 5.3.5 with a pan motion feedback system.

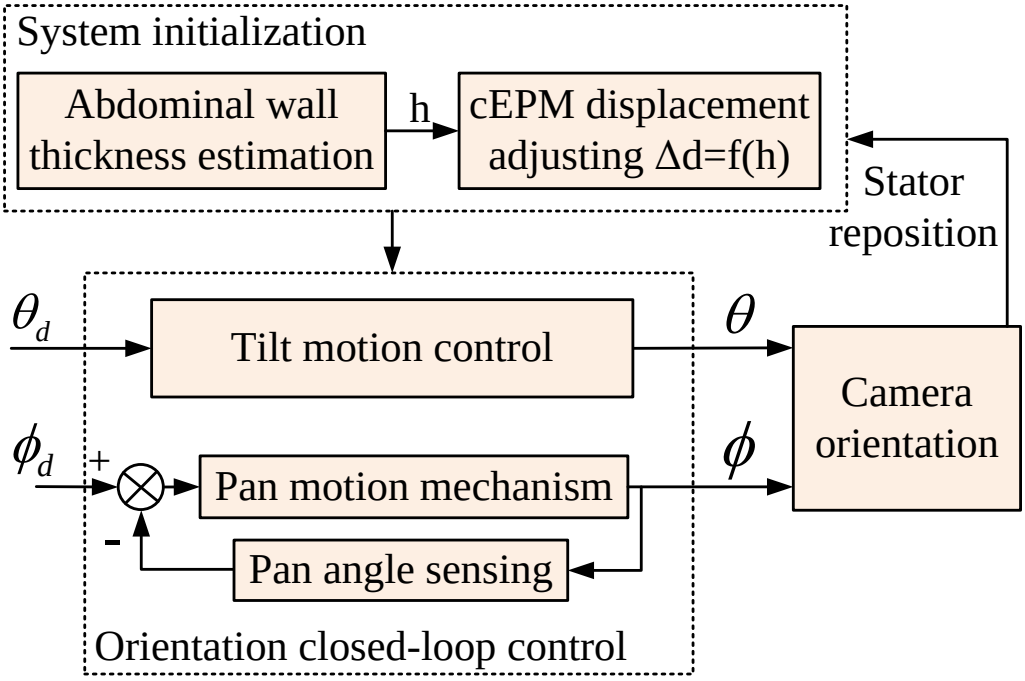

Figure 5.1: Robotic camera system orientation control architecture.

To clarify the relationship between the stator and the rotor, coordinate systems are defined in Fig. 4.2, and explained as follows:

- $\Sigma_{Ei}\{X_{Ei}, Y_{Ei}, Z_{Ei}\}$ represent the coordinate systems of the EPMs, $i = 1, 2, 3$.
- $\Sigma_{Ci}\{X_{Cj}, Y_{Cj}, Z_{Cj}\}$ represent the coordinate systems of the coils, $j = 1, 2$.
- $\Sigma_S\{X_S, Y_S, Z_S\}$ and $\Sigma_I\{X_I, Y_I, Z_I\}$ represent the internal coordinates of the stator and the rotor respectively.
- $\Sigma_{Ic}\{X_{Ic}, Y_{Ic}, Z_{Ic}\}$ represents the body attached coordinate systems of the cIPM.

5.3.1 Optimal Vertical Displacement of cEPM

The criteria of the optimal vertical displacement Δd of the cEPM is to minimize the magnetic field generated by the three EPMs at the location of the cIPM. Since the location of the cIPM with respect to the stator is determined by an abdominal wall thickness h, the objective is to develop a function for Δd with h as the variable.

Magnetic Field Analysis of the Stator

Due to the fixed relative positions of the EPMs and the coils, the stator magnetic field can be calculated by superimposing the magnetic fields from the EPMs and the coils Liu et al. (2014b). The whole stator magnetic field $\mathbf{B}_s \in \mathbb{R}^{3\times1}$ in Σ_S is formulated as

$$\mathbf{B}_s(\mathbf{P}_s) = \sum_{i=1}^{3} \mathbf{R}_{Ei}\mathbf{B}_e^i + \sum_{j=1}^{2} \mathbf{R}_{Cj}\mathbf{B}_c^u I_{cj}, \tag{5.1}$$

where $\mathbf{B}_e^i \in \mathbb{R}^{3\times1}$ denotes the magnetic flux density of the i^{th} EPM in Σ_{Ei}; $\mathbf{B}_c^u \in \mathbb{R}^{3\times1}$ represents the magnetic flux density of an iron-core coil with unit current in Σ_{Cj}; I_{cj} are the coil current inputs; $\mathbf{P}_s$ represents a spacial point in Σ_S; $\mathbf{R}_{Ei} \in \mathbb{R}^{3\times3}$ and $\mathbf{R}_{Cj} \in \mathbb{R}^{3\times3}$ represent the rotational matrices from Σ_S to Σ_{Ei} and from Σ_S to Σ_{Cj} respectively.

Assume that $\mathbf{P}_s = (0, 0, -h)^T$ is the location of the cIPM in Σ_S and the coils are deactivated with $I_{cj} = 0$. According to (5.1), the objective function that characterizes the optimal vertical displacement Δd can be represented as

$$\mathbf{B}_s(0, 0, -h) = \sum_{i=1}^{2} \mathbf{R}_{Ei}\mathbf{B}_e^i + \mathbf{R}_{E3}\mathbf{B}_e^3(\mathbf{P}_3) = \mathbf{0}, \tag{5.2}$$

where $\mathbf{P}_3 = \mathbf{R}_{C3}^T(0, 0, -h - \Delta d)^T$ is the point $\mathbf{P}_s$ represented in Σ_{E3}; $\mathbf{B}_e^3$ represents the magnetic flux density of the cEPM.

Unified Analytical Model of $\mathbf{B}_e^i$ and $\mathbf{B}_c^u$

The representation of the stator magnetic field in (5.1) and the identification of the relationship between Δd and h in (5.2) both require analytical models of the EPMs and the coils. Inspired by Kok-Meng and Hungsun (2007), $\mathbf{B}_e^i$ and $\mathbf{B}_c^u$ can be represented in a unified multi-pair magnetic dipole model due to the cylinder shape of the EPMs and the coils. Compared with a single-pair magnetic dipole model applied

in Liu et al. (2014b), a multi-pair magnetic dipole model has more abilities to achieve an accurate magnetic field estimation.

The unified magnetic field model is illustrated in Fig. 4.8. The positive and negative magnetic charges are distributed on the top and bottom surfaces of the cylinder in Fig. 4.8(a). Fig. 4.8(b) shows the arrangement of magnetic charges on the positive surface. Because the magnetic charges are symmetrically distributed around Z axis, only a quarter values of the magnetic dipoles need to be estimated by using numerical magnetic field data. By summarizing all the magnetic dipoles, the magnetic flux density $\mathbf{B}_0 \in \mathbb{R}^{3\times 1}$, which can be used as $\mathbf{B}_e^i$ or $\mathbf{B}_c^u$, is expressed by

$$\mathbf{B}_0 = \frac{\mu_0}{4\pi} m_0 \Gamma_{00} + \frac{\mu_0}{4\pi} \sum_{i=1}^{K_m} \sum_{j=1}^{N_m} m_{ij} \Gamma_{ij}, \tag{5.3}$$

$$\Gamma_{ij} = \mathbf{Q}_{ij+}/|\mathbf{Q}_{ij+}|^3 - \mathbf{Q}_{ij-}/|\mathbf{Q}_{ij-}|^3, \tag{5.4}$$

where m_{ij} is the strength of the ij^{th} magnetic dipole, and m_0 is the strength of the magnetic dipole at the center; K_m denotes the number of magnetic dipoles radially, and N_m is the number of magnetic dipoles for a single loop; $\mathbf{Q}_{ij+/-}$ represents a vector from the location of positive/negative magnetic charge $\mathbf{P}_{mij+}/\mathbf{P}_{mij-}$ to a point $\mathbf{P}$ in space. Eleven magnetic changes are evenly sampled starting at (x=0, y=0), along +Y direction. The interval distance Δa between two adjacent charges is calculated as $a/10$. Then the magnetic charge sampling line on +Y axis rotates around Z axis with a sampling interval angle $\Delta\theta$ as $\pi/6$. Because the 121 magnetic charges are symmetrically distributed around Z axis, the parameters needs to be estimated are m_{00}, $m_{i1}, (i = 1, ..., 10)$, and the virtual magnetic length L.

Optimal Displacement $\Delta d = f(h)$

Due to the highly nonlinear property of (5.2), it is difficult to explicitly represent Δd with h as the variable. An alternative way to develop this function is to build a lookup table by giving a range of abdominal wall thickness values h. After searching

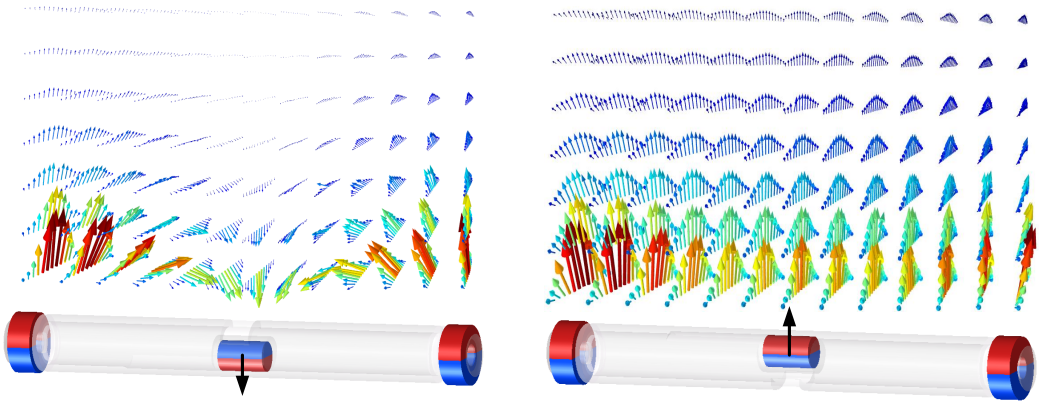

(a) Rotor initial pose 1 (b) Rotor initial pose 2

Figure 5.2: Rotor poses for the pre-built magnetic field map.

for Δd that satisfy (5.2), the optimized Δd values are stored in the lookup table. To this end, the optimal vertical displacement of cEPM Δd can be identified in real time for different abdominal wall thicknesses h.

5.3.2 Abdominal Wall Thickness Estimation

Due to both the rotor (camera robot) and the stator contacting an insufflated abdominal wall internally and externally respectively, the abdominal wall thickness can be estimated by the rotor-to-stator distance. The rotor creates a static magnetic field when its orientation is not actuated by the stator. Benefiting from this fact, the magnetic field of the rotor measured at the stator side varies only according to the rotor-to-stator distance. The main idea of estimating an abdominal wall thickness is to sense the magnetic field from the rotor by using a pre-built rotor magnetic field map which is with respect to the rotor-to-stator distances.

There are three problems to address for estimating an abdominal wall thickness: 1) the rotor orientation which is used for building the magnetic field map; 2) the configuration of the magnetic field sensors in the stator; and 3) the rotor-to-stator distance estimation method by using the sensed magnetic field from the rotor. The sensor configuration should avoid making the sensors inundated by the magnetic field

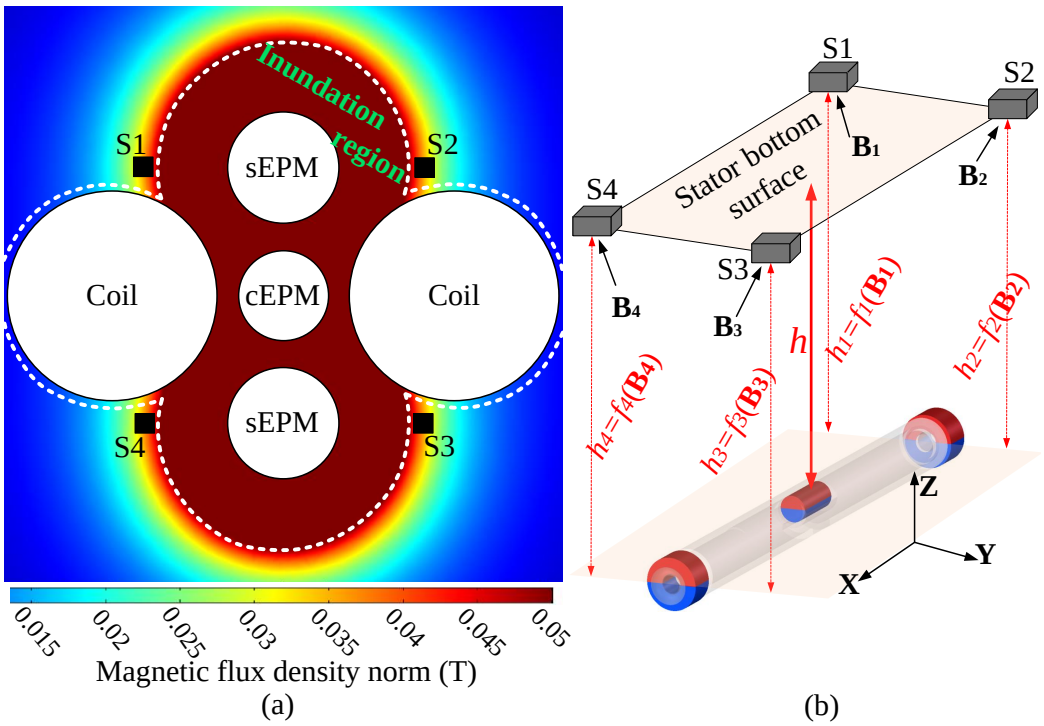

Figure 5.3: Magnetic field sensor configuration at the bottom surface of the stator. The simulation result is generated by COMSOL Multiphysics 5.0.

from the EPMs, and keep the distances between the rotor and the sensors as close as possible, which can make the rotor magnetic field be well recognized by the sensors. The method used to estimate the rotor-to-stator distance should be robust, can be computed in real time, and is capable of providing accurate results.

Rotor pose

The rotor pose determines the magnetic field distribution, which impacts on the difficulty of building up the magnetic field map and the performance of an abdominal wall thickness estimation. Fig. 5.2 shows two desired rotor poses that can generate symmetric magnetic field maps. The two rotor poses can be actuated by deactivating the stator coils and adjusting the cEPM to its minimum and maximum displacements for (a) and (b) respectively. Under the minimum cEPM displacement, the cIPM is dominated by the magnetic field from the cEPM, and aligned with the cEPM

orientation. Under the maximum cEPM displacement, the cIPM is dominated by the magnetic field from the sEPMs, and aligned with the sEPMs orientation. The arrows in Fig. 5.2 (a) and (b) illustrates the magnetic field strength (proportional to the arrow lengths) and magnetic field direction (the arrow directions) in the space between the rotor and the stator. It is obvious that the rotor pose in (b) can generate more recognizable magnetic field than that in (a) to be sensed in the stator. Therefore, the rotor pose in (b) is used to build the magnetic field map and estimate the rotor-to-stator distances.

Sensor configuration

To estimate the rotor-to-stator distance by sensing the symmetric magnetic field from the rotor, four sets of tri-axis hall effect sensors are applied at the bottom the stator. It is important to select appropriate locations for the sensors to prevent being inundated by the magnetic field from the EPMs. Fig. 5.3(a) shows the magnetic flux density norm distribution at the bottom surface of the stator. The inundation region in dark red is determined by the measuring ranges of the applied hall effect sensors (CYL8405, Chenyang-Technologies GmbH& Co. KG, measuring range 64 mT). The symmetrically distributed black squares S_1, S_2, S_3, S_4 represent the sensor installing locations which are out of the inundation region and closest to the rotor aligned with the EPMs. The distances from S_1 to S_2 and S_4 are both 60 mm.

Rotor-to-stator distance estimation

As illustrated in Fig. 5.3(b), the tri-axis hall effect sensors $S_i (i = 1, 2, 3, 4)$ detect magnetic field $\mathbf{B}_i$ from the rotor under the rotor-to-stator distance h. Due to the magnetic coupling of the EPMs and the IPMs, the positions between the sensors and the rotor are relatively fixed in X and Y directions. The magnetic field maps f_i represent the relationship between the rotor magnetic field $\mathbf{B}_i$ as inputs and the rotor-to-stator distances h_i as outputs. The mapping functions f_i represented in lookup

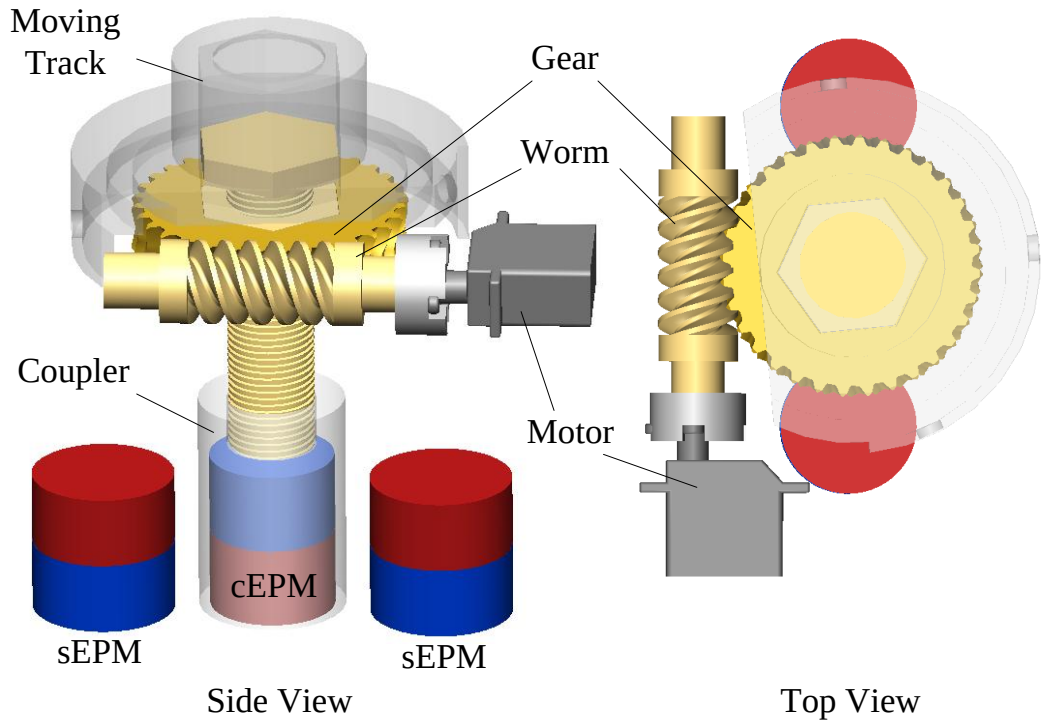

Figure 5.4: cEPM displacement adjusting mechanism in the stator

tables are developed by recording the magnetic fields with the sensors while adjusting the rotor-to-stator distance h.

With the mapping functions f_i and the magnetic fields $\mathbf{B}_i$ sensed by S_i, an abdominal wall thickness can be estimated by

$$h = \frac{1}{N} \sum_{i=1}^{N} f_i(\mathbf{B}_i), \tag{5.5}$$

where $N = 4$ represents the total group number of the hall effect sensors.

5.3.3 cEPM Adjusting Mechanism

According to the estimated abdominal wall thickness h by using (5.5), the optimal displacements of the cEPM $\Delta d = f(h)$ developed in Section 5.3.1 needs to be applied on the cEPM. To enable autonomous control of this process, a displacement adjusting mechanism for the cEPM is required in the stator. Considering the strong magnetic

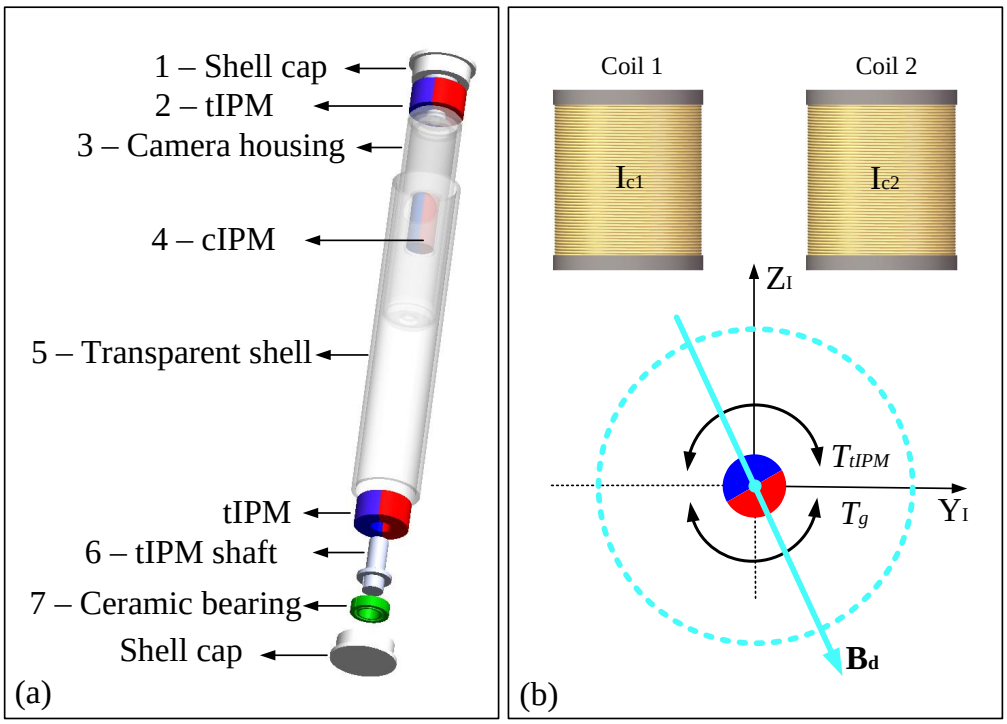

Figure 5.5: (a) Conceptual illustration of the rotor design. (b) Rotor tilt motion control with the coils.

coupling between the cEPM and the sEPMs, the design objective of the adjusting mechanism should be capable of providing sufficient lifting force for the cEPM, and keep the whole stator as compact as possible.

Fig. 5.4 shows the conceptual illustration of the mechanism design which is basically a screw jack driven by a motor. The reason to use such a mechanism is twofold: 1) the lifting force for the cEPM can be efficiently provided by the motor torque through the worm and gear mechanism; 2) the self-locking function of the design enables the cEPM to keep still when the motor is not actuated. The bolt that connects with the cEPM by using a coupler is actuated by the gear rotation. The moving track restricts the bolt rotation, keeps the bolt and the cEPM moving vertically.

5.3.4 Tilt Motion Control

Camera protection shell

According to our original rotor design in Liu et al. (2015), the camera lens can easily get blurred by peritoneal fluid due to the direct contact with an abdominal wall. To address this issue, a transparent shell is applied to prevent the camera lens from contacting with tissue and also to maintain imaging quality, as illustrated in Fig. 5.5(a)-5. Two ceramic bearings (Fig. 5.5(a)-7) and two tIPM shafts, which are fixed in the shell caps (Fig. 5.5(a)-1), are used for hanging the camera housing (Fig. 5.5(a)-3) inside the transparent shell with no contact. This design provides the camera smooth rotation inside the shell when rotational torque is exerted on the cIPM (Fig. 5.5(a)-4). Another benefit of this design is to make the laparoscopic camera reusable by depositing the shell after use, and subsequently reduces a surgery cost.

Control with electromagnetic coils

The robot tilt motion is activated by the magnetic coupling between the coils and the cIPM. I_{c1} and I_{c2} are represented as the current inputs of the coils, and θ is represented as the rotational angle of the robot tilt motion.

The factors that impact on the camera tilt motion need to be considered before developing a tilt motion control method. The camera protection shell insulates the rotor from contacting with an abdominal wall. It makes the camera free of frictional torque from an abdominal wall during tilt motion. After estimating an abdominal wall thickness and adjusting the displacement of the cEPM that were developed in Section 5.3.2 and 5.3.3, the EPMs have ignorable impact on the tilt motion of the cIPM. Beside the control inputs I_{c1} and I_{c2}, the tilt motion of the cIPM is also affected by T_g and T_{tIPM} which are the torque due to the robot gravity along X_I and the magnetic torque on the cIPM from the tIPMs along X_I respectively. As illustrated in Fig. 5.5(b), T_g and T_{tIPM} are always in opposite directions that are canceled by each

other according to our preliminary experimental investigation. Therefore, the camera tilt angle aligns with the direction of the magnetic field generated by the coils. The objective to control the camera tilt motion is to determine I_{c1} and I_{c2} for generating a magnetic field with the direction θ at $\mathbf{P}_s$ in Σ_S that is the location of the cIPM.

The relationship between the current inputs I_{c1}, I_{c2} and a desired magnetic field direction θ at $\mathbf{P}_s$ can be formulated by (5.6) in Σ_S as follows

$$\underbrace{(\mathbf{R}_{C1}\mathbf{B}_c^u)}_{\mathbf{B}_{c1}^S} I_{c1} + \underbrace{(\mathbf{R}_{C2}\mathbf{B}_c^u)}_{\mathbf{B}_{c2}^S} I_{c2} = \underbrace{\mathbf{R}_I^S \mathbf{R}_{Ix}(\theta)\mathbf{B}^{-z}}_{\mathbf{B}_d}, \tag{5.6}$$

where $\mathbf{R}_I^S \in \mathbb{R}^{3\times3}$ represents a rotational matrix from Σ_I to Σ_S. According to the setting of Σ_S and Σ_I in Fig. 4.2(b), $\mathbf{R}_I^S$ is an identity matrix. $\mathbf{R}_{Ix}(\theta) \in \mathbb{R}^{3\times3}$ represents the rotational matrix along X_I with θ as the variable. $\mathbf{B}^{-z} \in \mathbb{R}^{3\times1}$ denotes a unit vector pointing in $-Z_I$. $\mathbf{B}_{c1}^S, \mathbf{B}_{c2}^S \in \mathbb{R}^{3\times1}$ denote the unit current magnetic field of the coils at $\mathbf{P}_s$ in Σ_S. $\mathbf{B}_d \in \mathbb{R}^{3\times1}$ denotes the desired magnetic field direction as shown in Fig. 5.5(b). Benefiting from the analytical magnetic field model in (5.3), $\mathbf{B}_{c1}^S$, $\mathbf{B}_{c2}^S$ can be computed in real time.

Considering the x components in $\mathbf{B}_{c1}^S$, $\mathbf{B}_{c2}^S$, and $\mathbf{B}_d$ are zeros, (5.6) is reformulated as

$$\mathbf{B}_d^{yz} = \mathbf{B}_c^{S_{yz}} \mathbf{I}_c, \tag{5.7}$$

where $\mathbf{B}_c^{S_{yz}} = [\mathbf{B}_{c1}^{S_{yz}}, \mathbf{B}_{c2}^{S_{yz}}] \in \mathbb{R}^{2\times2}$, $\mathbf{B}_d^{yz} \in \mathbb{R}^{2\times2}$, $\mathbf{I}_c = [I_{c1}, I_{c2}]^T \in \mathbb{R}^{2\times1}$. Because $\mathbf{B}_c^{S_{yz}}$ has a full row rank, the current input vector $\mathbf{I}_c$ can be found in (5.8) by applying pseudoinverse to (5.7)

$$\mathbf{I}_c = (\mathbf{B}_c^{S_{yz}})^T (\mathbf{B}_c^{S_{yz}} (\mathbf{B}_c^{S_{yz}})^T)^{-1} \mathbf{B}_d^{yz}. \tag{5.8}$$

To achieve high accuracy tilt motion control, a closed-loop control scheme is developed as illustrated in Fig. 5.6. Given a desired tilt angle θ_d, the current control vector is calculated by $\mathbf{I}_c = \tilde{f}(\mathbf{P}_s, \tilde{\theta})$ which is a representation of (5.8). Because

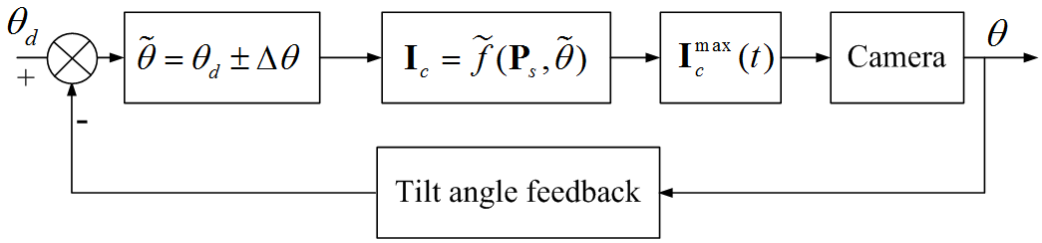

Figure 5.6: Block diagram of the camera tilt motion control.

the solution of (5.8) only provides the ratio of I_{c1} and I_{c2}, the input current vector is amplified by using the limit value of current inputs I_{max} for maximizing the generated magnetic field. A current input trajectory $\mathbf{I}_c^{max}(t)$ can thus be developed within a given time ΔT, and applied to the camera. The arrived tilt angle θ at the end of $\mathbf{I}_c^{max}(t)$ is sensed by a tilt angle sensor for feedback. If $|\theta_d - \theta|$ is smaller than a given threshold δ, the tilt angle control process is complete. Otherwise, an adjusted tilt angle $\tilde{\theta} = \theta_d \pm \Delta\theta$, where $\Delta\theta$ is a small angle, is served as an input to calculate $\mathbf{I}_c$.

5.3.5 Pan Motion Mechanism

The pan motion of the camera robot is actuated by the rotation of the stator due to the magnetic coupling between the EPMs and the tIPMs as conceptually illustrated in Fig. 4.2. To control the pan motion automatically, it is desired to design an actuation mechanism that can generate rotational motion of the stator.

Fig. 5.7 shows the pan motion mechanism in the stator. The design objective is to control the rotation of the stator core which is sitting inside the stator shell. The motor driven spur gear is fixed on the stator core, while an internal gear is attached on the internal surface of the stator shell. The stator core can thus be actuated by the relative motion of the spur gear and the internal gear. To keep smooth relative rotation between the stator core and the stator shell, a thrust bearing is applied at their contact surfaces.

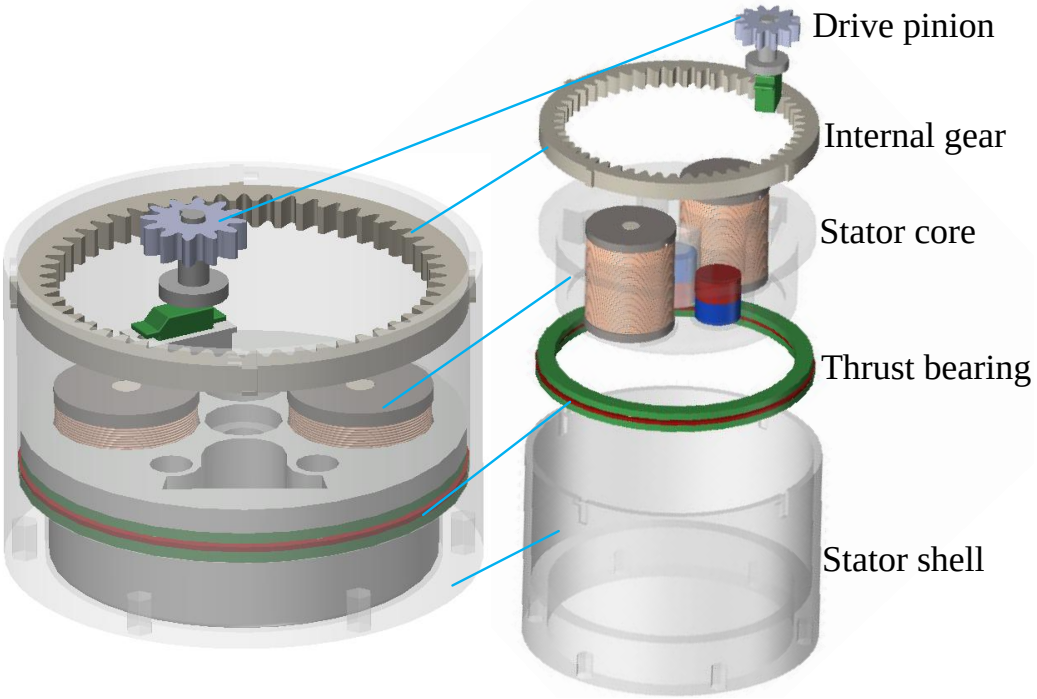

Figure 5.7: Pan motion mechanism.

5.4 Prototype Development and Experimental Investigation

5.4.1 Stator Fabrication

cEPM adjusting mechanism

The function of the cEPM adjusting mechanism that proposed in section 5.3.3 is to position the cEPM to the vertical displacement Δd according to the estimated abdominal wall thickness in (5.5). To make the mechanism function, two issues have to be concerned: (1) the mechanism has to provide sufficient lifting force to overcome the magnetic force between the cEPM and the sEPMs; (2) the cEPM has to be accurately controlled to the desired displacement Δd.

Fig. 5.8 shows the fabrication of the cEPM adjusting mechanism. The worm in Fig. 5.8(a) is with pitch diameter 12.19 mm, outside diameter 15 mm, number of

threads $N = 3$, worm length 25 mm. The gear in Fig. 5.8(a) is with 32 teeth, pitch diameter 45 mm, outer diameter 49.25 mm, face width 10 mm. The nut in Fig. 5.8(a) that fixed at the gear center is used for generating vertical displacements of the bolt by rotating the gear and the nut. The hex nut is with height 13.89 mm, diameter 15.875 mm. The bolt in Fig. 5.8(a) is matching with the nut with thread length 53 mm, screw pitch $p = 2$ mm. According to our experiment, the maximum force used to pull out the cEPM from the magnetic coupling between the cEPM and the sEPMs is about $F = 50$ N. The required motor torque M_T can be estimated by

$$M_T = \frac{F \cdot p}{2\pi \cdot \eta_s \cdot \eta_{wg} \cdot r}, \tag{5.9}$$

where η_s and η_{wg} are the efficiencies of the screw and the worm-gear respectively; $r = 32/3$ is the gear ratio of the worm gear. M_T is estimated as 0.149 Nm by conservatively assuming $\eta_s = 10\%$ and $\eta_{wg} = 10\%$. A servo motor (S3156, Futaba Inc.) in Fig. 5.8(a), which can provide 0.196 Nm at 4.8 V, was modified into continuous rotation for our application. To avoid influencing the magnetic field of the stator, the silicone brass screw and nut (Bolt Depot, Inc.) were selected for the design.

Fig. 5.8(b) shows the assembly of the cEPM adjusting mechanism with the displacement sensing system on the stator core that houses the EPMs and the coils. To sense an actuated displacement of the cEPM, a magnetic encoder is designed by using four tiny cylindrical permanent magnets symmetrically distributed on the gear surface. A single hall effect sensor (CYL8405, Chenyang-Technologies GmbH& Co. KG) is applied to pickup the magnetic field signal from the magnets for estimating the rotational motion of the gear. The screw travels 2 mm when the gear generates a full rotation. Four magnets can thus provide 0.5 mm traveling resolution of the screw.

Abdominal wall thickness sensing system

According to the design in Section 5.3.2, the magnetic field sensing system were implemented at the bottom of the stator core, as illustrated in Fig. 5.9(a). The

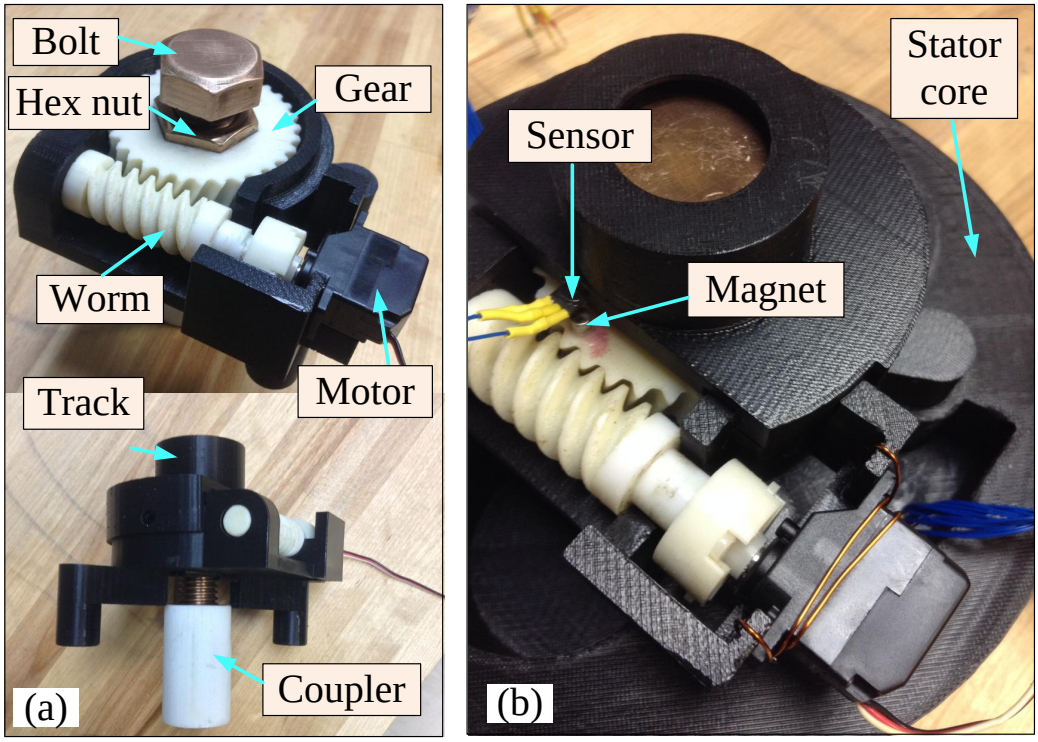

Figure 5.8: Fabrication of the cEPM adjusting mechanism.

bottom of the stator core is carved around the EPMs and the coils with 5 mm depth for installing magnetic field sensors. Four sets of tri-axis hall effect sensors with measuring ranges $0 \sim 64$ mT and sensitivities about 50 mV/mT were symmetrically fixed in the carved bottom. To enable the sensing system to well recognize the tiny change of the magnetic field from the rotor, the measured signals were converted to digital signals with sensing resolution 0.01 mT by using a 16bit ADC (ADS1115, Texas Instruments Inc.).

The estimation function developed in (5.5) was implemented by the data acquired from Fig. 5.9(b). The configuration of the hall effect sensors in Fig. 5.9(b) is the same as the sensor configuration in Fig. 5.9(a). A rotor with the pose in Fig. 5.2(b) was fixed on a vertical positioning stage for adjusting the distance between the rotor and the sensors S_i. Fig. 5.9(c) shows the mapping functions $f_i, (i = 1, 2, 3, 4)$, which record the norms of the magnetic flux densities $|\mathbf{B}_i|$ and the vertical distances h_i between the rotor and the sensors S_i. During the process of an abdominal wall thickness

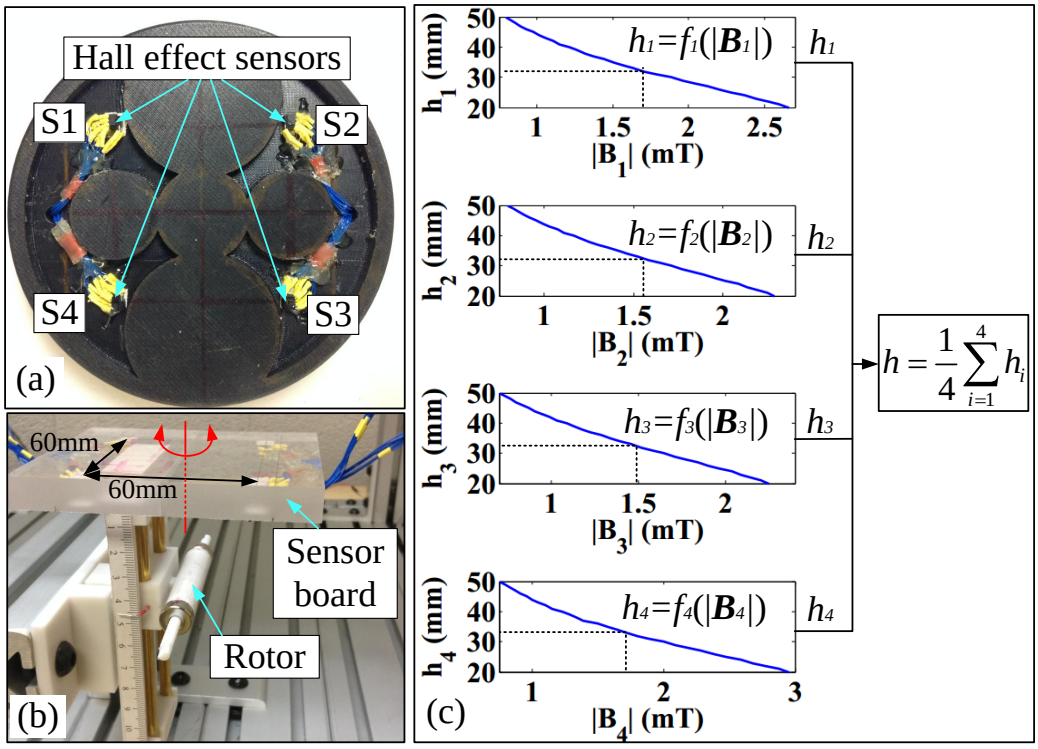

Figure 5.9: Fabrication of abdominal wall thickness sensing system,.

estimation, f_i return the distances h_i by using the detected $\mathbf{B}_i$ in S_i. An average value of h_i was used as the final estimated abdominal wall thickness h for improving the robustness of this method.

Stator core

According to the design in Liu et al. (2015), the stator core consists of two coils, two identical sEPMs and one cEPM. The detailed dimensions and materials are shown in Table 4.2.

Pan motion mechanism

The fabricated parts of the pan motion mechanism is demonstrated in Fig. 5.14(c). The internal gear has 52 teeth with a pitch diameter 132 mm, a major diameter 139.4 mm, and a minor diameter 128 mm. The drive pinion has 12 teeth with a pitch

diameter 30.48 mm, a major diameter 36.56 mm, and a minor diameter 25.13 mm. The face widths of the internal gear and the drive pinion are both 10 mm. The stator shell is with an external diameter 164 mm and a height 109 mm. The thrust bearing with an inner diameter 133.6 mm and an outer diameter 154.6 mm sits inside the stator shell with 30 mm distance to the shell bottom. A modified digital servo motor, which is identical to the motor applied on the cEPM adjusting mechanism, is fixed on the stator core and connected with the drive pinion. To protect the stator core when the stator contacts with an abdominal wall and avoid impacting on the magnetic field interaction between the rotor and the stator, a brass board with diameter 164 mm and thickness 1.64 mm was applied at the bottom of the stator shell.

Coil current control system

A tethered current control system was developed by the PWM technique. The system consists of a micro-controller (STM32F4Discovery, STMicroelectronics Inc.) to generate PWM signals, two PWM amplifiers (L6205 DMOS Full Bridge Driver, STMicroelectronics Inc.) to amplify the signals, a power supply for powering up the amplifiers, and a PC computer to send control command to the micro-controller via a serial communication.

5.4.2 Rotor Fabrication

Fig. 5.10 shows the fabrication of the dummy camera with the disassembled parts. The specifications of the camera is illustrated in Table 5.1. The outer diameter of the transparent shell (MOCAP, Inc.) determines the diameter of the camera which is 14.52 mm. Considering that the diameter of a standard trocar is in the range of 12 mm $\sim$ 15 mm, our camera design can be inserted into an abdominal cavity through a standard trocar. The miniature ceramic ball bearings (NationSkander California Corp.), which have 5 mm inner diameter and 9 mm outer diameter with

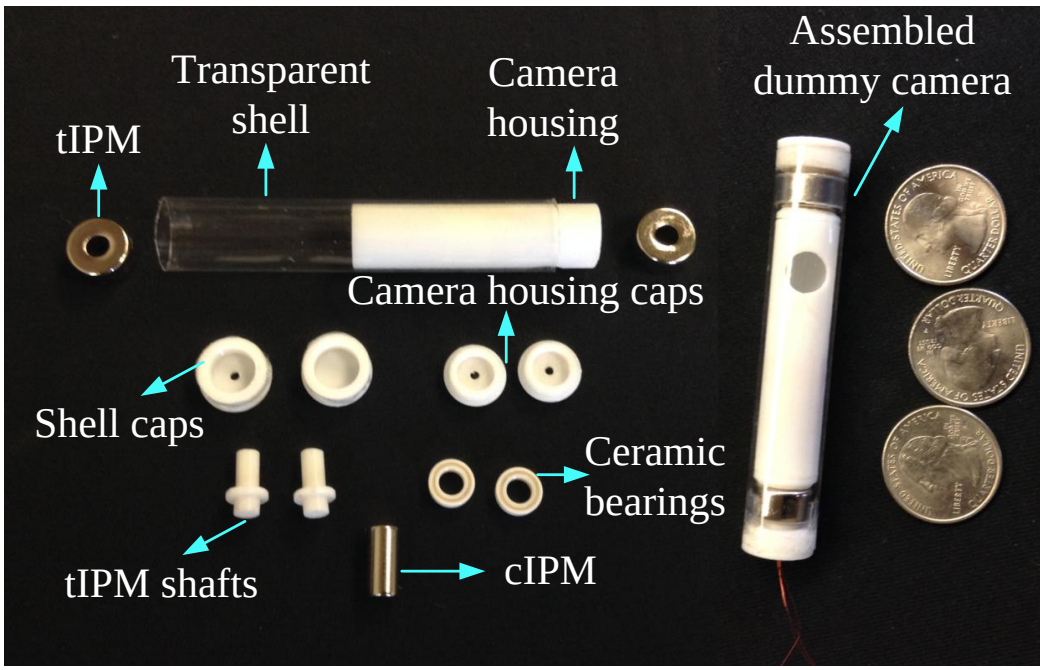

Figure 5.10: The disassembled dummy camera parts and the assembled dummy camera.

3 mm thickness, enable smooth rotation of the camera housing inside the transparent shell.

5.4.3 Calibration of Magnetic Field Models

The models of the stator magnetic field developed in Section 5.3.1 were represented by (5.3) with parameters m_{00}, $m_{i1}, (i = 1, ..., 10)$, and the magnetic length L . Due to the imperfection of the coil wrapping, the iron cores, and the permanent magnets, the model calibration was performed by using experimental data. Fig. 5.11(a) shows the experiment platform for magnetic field calibration which consists of a transparent board to support the EPMs or the coils, a X-Z position stage, and three hall effect sensors for 3-axis sensing. Fig. 5.11(b) and (c) show the magnetic flux density norm comparison results of the experimental data and the magnetic field models.

Fig. 5.11(b) illustrates the calibrated coil magnetic field model (the blue line) with a unit current input based on the experiment data (the blue circles). The red line

Table 5.1: Specifications of The Rotor and Stator Prototype Designs

Part Name	Dimension
Camera total length	79 mm
Transparent shell	OD 14.52 mm, ID 13.92 mm
Camera housing	OD 12.7 mm, ID 10 mm
cIPM:	Diametrically magnetized
Size	Diameter 6.35 mm, Length 12.7 mm
Material	NdFeB Grade N42
tIPM:	Diametrically magnetized
Size	OD 12.7 mm, ID 4.75 mm
	Thickness 6.35 mm
Material	NdFeB Grade N42
Dummy camera weight	21.38 g

and the red circles illustrates the magnetic field comparison result between the coil magnetic field with $I = 0.5$ A and the experiment data. This result validates the linear relationship between the coil input current and the generated magnetic field strength. Fig. 5.11(c) shows the magnetic field comparison result of the EPMs magnetic field model with the vertical displacements of the cEPM as $\Delta d = 1\,\text{mm}, 3\,\text{mm}, 5\,\text{mm}, 7\,\text{mm}$, and the experiment data. The coincidences of the model data and the experiment data at $B_{norm} = 0$ with different Δd validate the optimal displacement function $\Delta d = f(h)$ developed in Section 5.3.1. The average errors of the magnetic field models demonstrated in Fig.5.11(b) and (c) were 1.32% and 1.57% respectively.The calibrated parameters of the EPMs and the coils are illustrated in Table 5.2.

5.4.4 Control of cEPM Displacements

Fig. 5.12 shows the investigation of the control accuracy for the cEPM adjusting mechanism developed in Section 5.4.1. The target cEPM displacements were set from 2 mm to 10 mm with 2 mm intervals. For each test, the cEPM displacement were set at $\Delta d = 0$ initially. The results show that the average errors of all the tests were all within 0.35 mm which provides sufficient control accuracy for the our

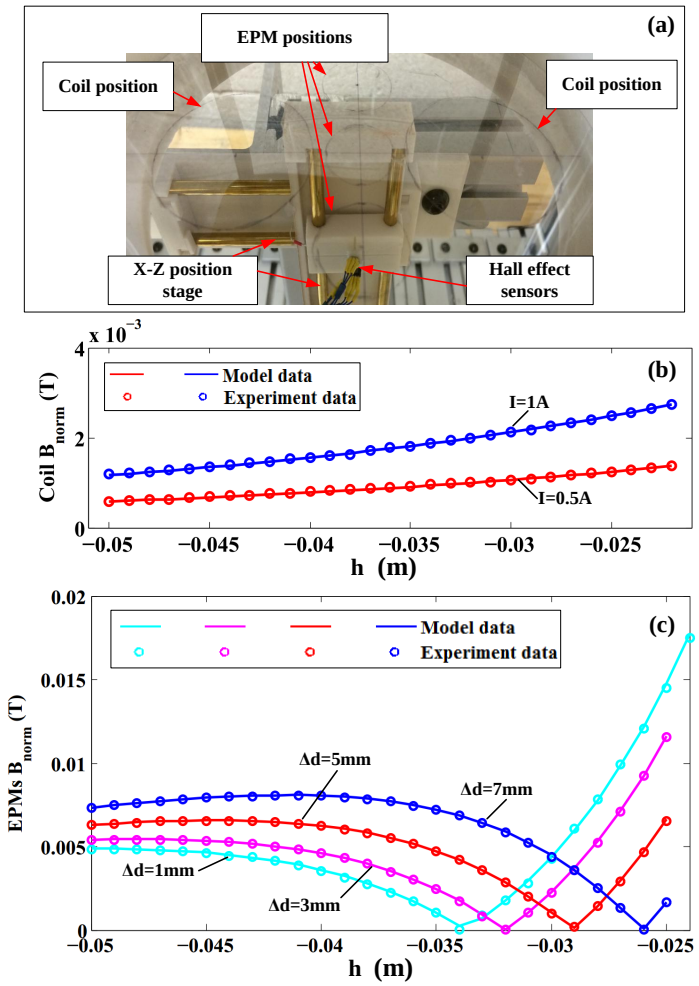

Figure 5.11: Experimental setup to calibration the magnetic field models of the stator.

system. As the cEPM displacements traveled from 2 mm to 10 mm, the errors were accumulated. The accumulated error can be limited within 0.35 mm by reseting the displacement counter when the minimum or the maximum displacements are reached.

5.4.5 Evaluation of Abdominal Wall Thickness Sensing Method

Fig. 5.13 shows the experimental setup (a) and experimental results (b) for evaluating the abdominal wall thickness sensing method developed in Section 5.3.2. To evaluate the sensing accuracy of the proposed method, the experiment was divided into two groups, which were 1) sensing under the impact of the EPMs; and 2) sensing without

Table 5.2: Calibrated parameters of the sEPMs, the cEPM and the coils. The units of m and L are ampere meter square $[Am^2]$ and meter $[m]$ respectively.

	m_{00}	m_{11}	m_{21}	m_{31}	m_{41}	m_{51}	m_{61}	m_{71}	m_{81}	m_{91}	$m_{10,1}$	L
sEPM	2.479	2.676	2.516	2.294	2.063	1.894	1.759	1.536	1.225	1.136	1.252	0.055
cEPM	2.493	2.456	2.436	2.393	2.349	2.305	2.264	2.233	2.209	2.193	2.185	0.038
Coil	2.494	2.401	2.394	2.398	2.394	2.403	2.395	2.398	2.398	2.393	2.401	0.016

the impact of the EPMs. The first group experiment was investigated by using the experimental setup in Fig. 5.13(a). The second group experiment was conducted by using the experimental setup in Fig. 5.9(b), which was used for developing the estimation function (5.5). In both groups, the rotor with the pose demonstrated in Fig. 5.2(b) was positioned under the sensors. To test the reliability and robustness of this method, the stator core in Fig. 5.13(a) and the sensor board in Fig. 5.9(b) were rotated within the range of $\pm 20^\circ$ during each sensing process. Fig. 5.13(b) shows the errors in detecting the rotor-to-stator distances for 25 mm, 30 mm, 35 mm, 40 mm, 45 mm, and 50 mm. The mean absolute errors and the standard deviations of the two groups under different testing distances are shown in Table 5.3. The data show the distance sensing system can provide less than 1 mm accuracy in average. To investigate the differences of the sensing errors between the two experiment groups, two-sample t-tests were applied to compare the MAEs and the SDs. The P values for the MAEs and the SDs were 0.6693 and 0.4210 respectively, which indicate that the differences were considered to be not statistically significant.

5.4.6 Experimental Platform

Fig. 5.14(a) shows the overview of the experimental environment. The robot system was fabricated by a 3D prototyping machine (Fortus 400mc, Stratasys Inc.). To simulate the viscoelastic properties of a real insufflated abdominal wall (average

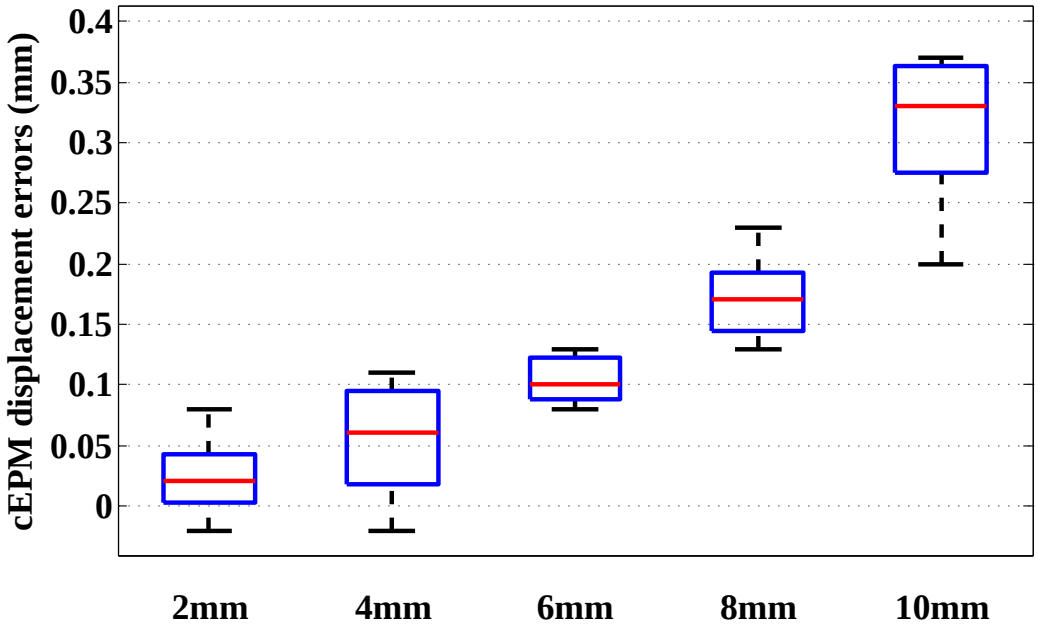

Figure 5.12: Control of cEPM displacement

Young's modulus 32.5 kPa) Song et al. (2006), a viscoelastic material Durometer 40 (Young's modulus 27.57 kPa at 15% deflection, Sorbothane, Inc.) was applied as illustrated in Fig. 5.14(b). The initial abdominal wall thickness was 26 mm (tissue layer 15 mm, support layer 11 mm). To increase the abdominal wall thickness for experimental studies, a vertical stator positioning mechanism in Fig. 5.14(a) was applied. A silicone oil lubricated rotor-tissue contact layer was added to the bottom of the viscoelastic material for mimicking an internal abdominal wall surface.

5.4.7 Camera Motion Control

The closed-loop control of the camera motion requires sensing systems for tilt angle and pan angle. Due to the lack of on-board internal sensing system at the current stage, separate motion feedback systems were designed for pan and tilt motion. The tilt motion sensing system applied a tri-axis accelerometer (LIS331HH, STMicroelectronics Inc.) inside the camera housing with wires for power supply and data transmission. To minimize the impact on the camera tilt motion from the wires,

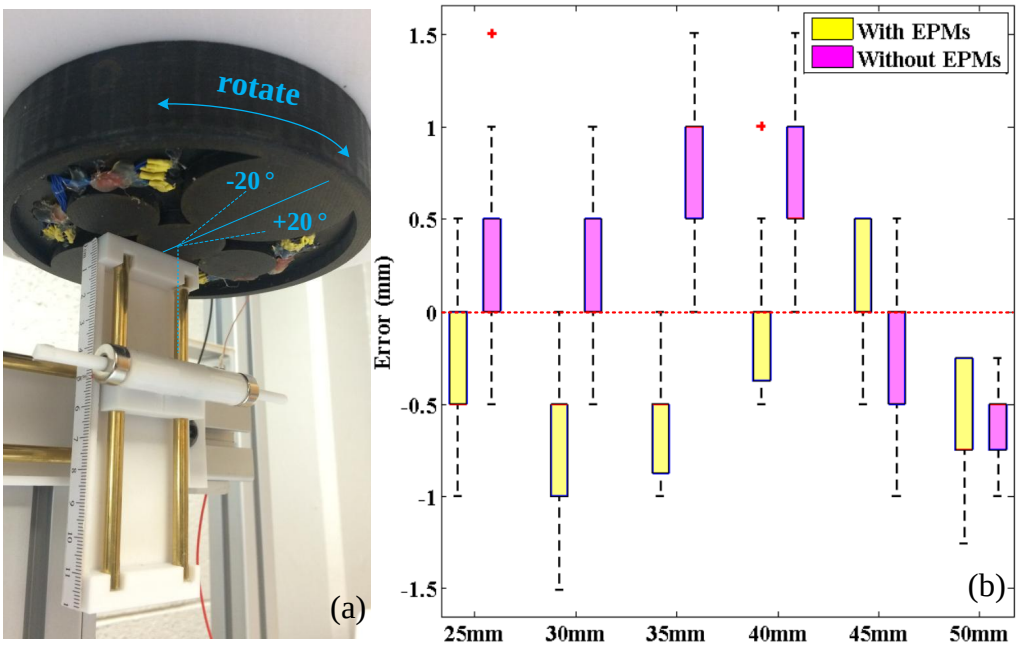

Figure 5.13: Abdominal wall thickness estimation result.

42 AWG enameled copper wires with diameter 0.066 mm were applied, as shown in Fig. 5.14(d). The pan motion sensing system applied a webcam (Logitech Pro 9000) under the rotor to track the positions of two color markers on the transparent shell of the rotor. The simulated abdominal wall thickness was adjusted to 35 mm which is about the average value of an normal abdominal wall thickness Song et al. (2006). The current inputs of the two coils are limited at $|I_{max}| = 1.5\,\mathrm{A}$ to prevent coil overheating.

Control of tilt motion

Fig. 5.15 shows the tilt motion control experiment by setting the desired tilt angles (red arrows) from 75° to −75° with 15° intervals. The green arrows shows the controlled tilt angles by using the control model developed in Section 5.3.4. Fig. 5.16 shows the tilt motion control trajectories for the desired tilt angles 15°, 45°, and 75° which cost 0.93 s, 1.74 s, and 1.99 s to reach to steady states. The average steady-state error of the controlled tilt angles in Fig. 5.15 and Fig. 5.16 was 0.67°.

Table 5.3: Mean Absolute Error (MAE) and Standard Deviation (SD) of The Sensed Distances

	With EPMs		Without EPMs	
Dist. (mm)	MAE (mm)	SD (mm)	MAE (mm)	SD (mm)
25	0.2672	0.3531	0.2368	0.5506
30	0.6118	0.3025	0.1771	0.2989
35	0.5256	0.3431	0.7216	0.3678
40	0.0116	0.3856	0.6910	0.3807
45	0.2	0.2857	0.1684	0.3832
50	0.5682	0.2424	0.5729	0.1943

Control of pan motion

Fig. 5.17 shows the pan motion control experiment which set the desired pan angles from 0° to 315° with 45° intervals. The drive pinion demonstrated in Fig. 5.7 was activated to rotate the stator core clockwise or counterclockwise accordingly for generating pan motion of the rotor, while the pan motion sensing sytem was detecting the current pan angle for feedback. The red and green arrows represent the desired pan angles and controlled pan angles respectively. The average control error was 0.49°.

Control of combined pan and tilt motion

Fig. 5.18 shows the combined control experiment of pan and tilt motion to demonstrate the control capability of our proposed system. By giving some desired orientations (red arrows) of the camera which covered the whole three dimensional space in an abdominal cavity, the orientations of the camera were controlled

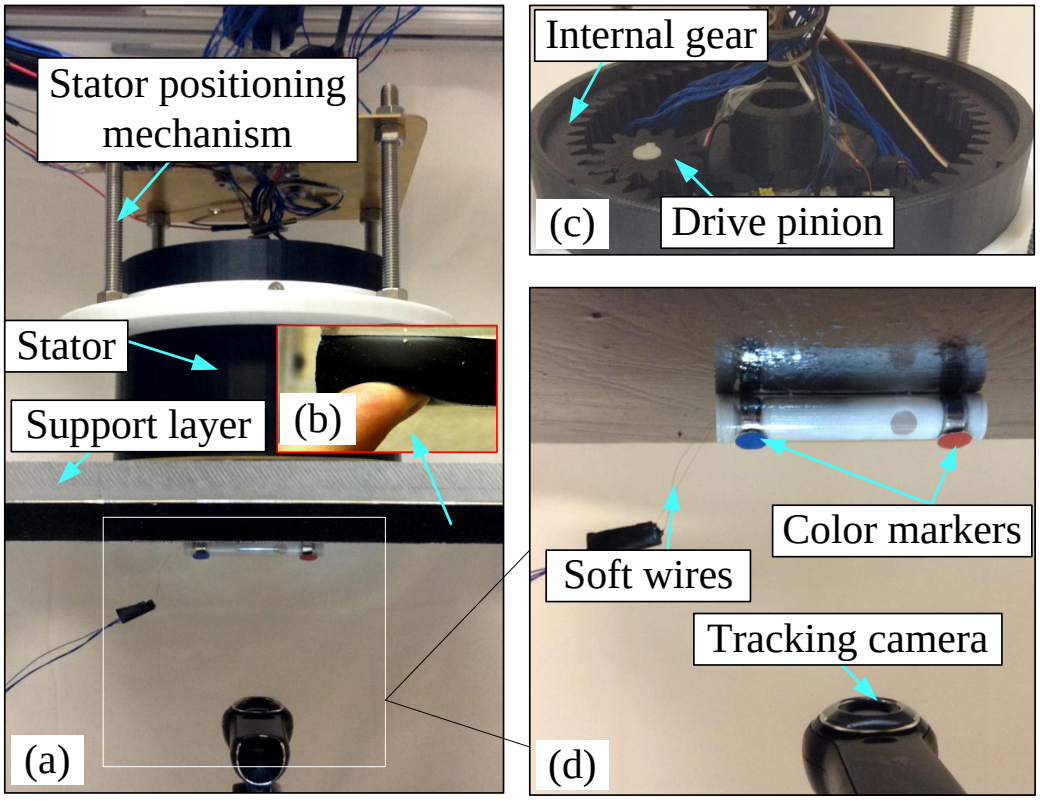

Figure 5.14: Experiment platform.

accordingly as illustrated by the green arrows. In the control tests, the experimental results indicate that the control system can provide the camera with less than 1° control accuracy for all the orientations investigated in the experiment.

5.5 Summary

In this chapter, a closed-loop control system of a novel insertable laparoscopic camera has been presented to enable autonomous fine orientation control of the camera. The experimental results indicate that the camera can achieve 0.67° and 0.49° control accuracies in tilt and pan motions respectively. The combined orientation control in three-dimensional space demonstrated less than 1° control accuracy. In our future work, the camera on-board electronics will be integrated especially an inertial sensor which is used to provide the camera orientation feedback wirelessly. the dimensions

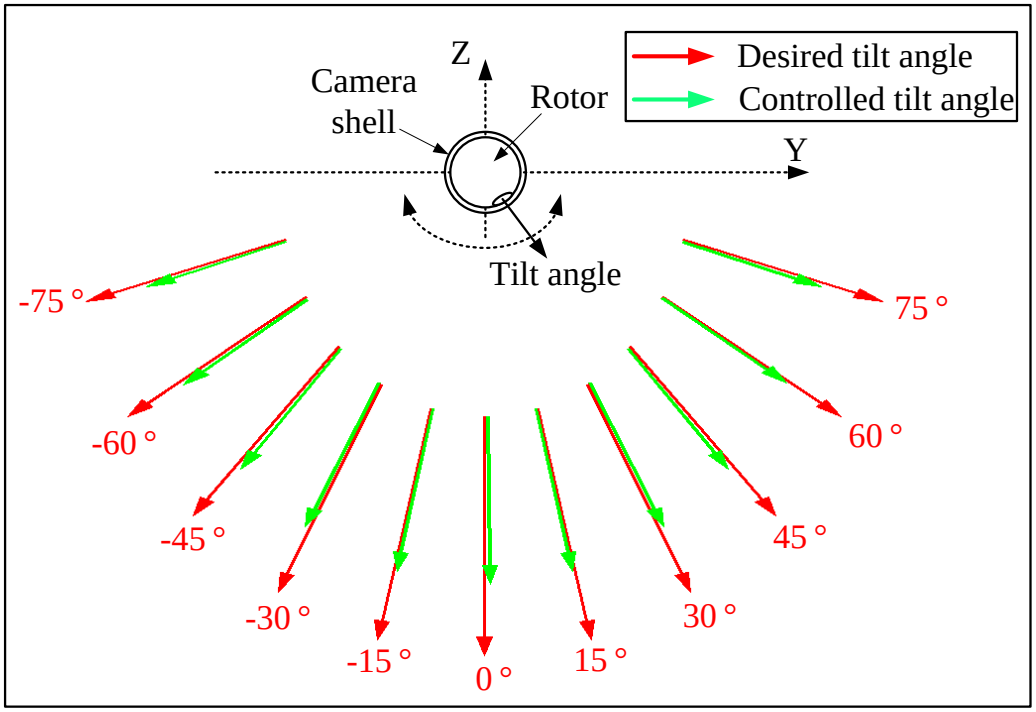

Figure 5.15: Tilt motion control experiment.

and the weight of the stator will be further decreased. The stator cables will be removed by integrating a wireless module, coil drivers, and batteries inside the stator. The camera system will be tested *in vivo* by using a porcine abdominal cavity.

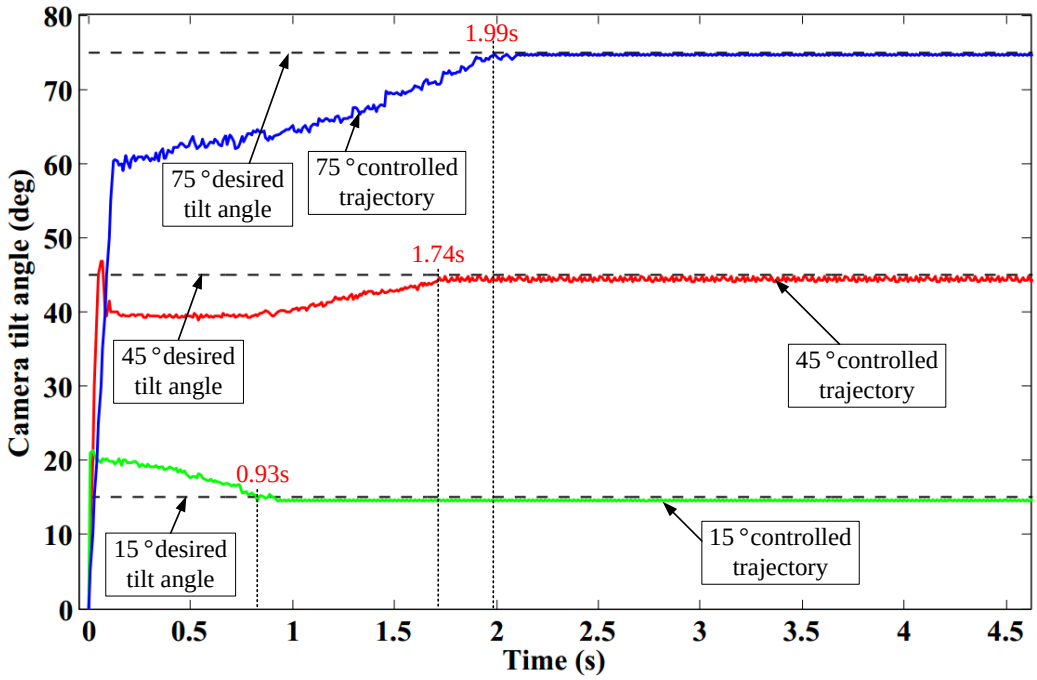

Figure 5.16: Tilt motion control trajectories.

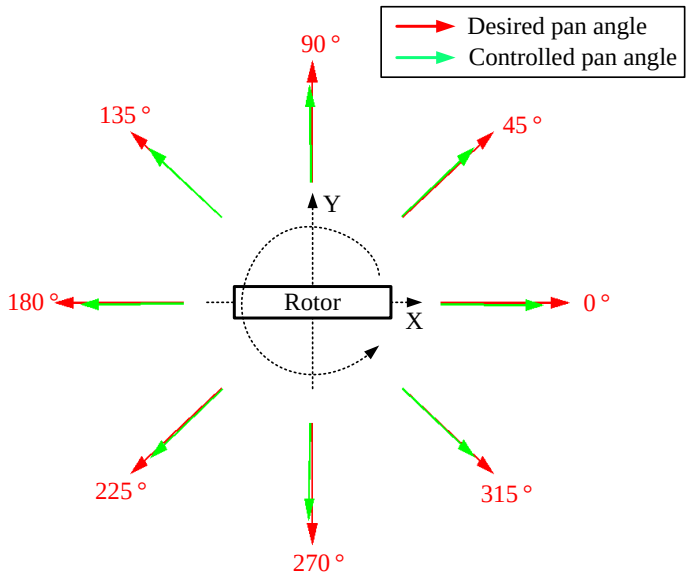

Figure 5.17: Pan motion control experiment.

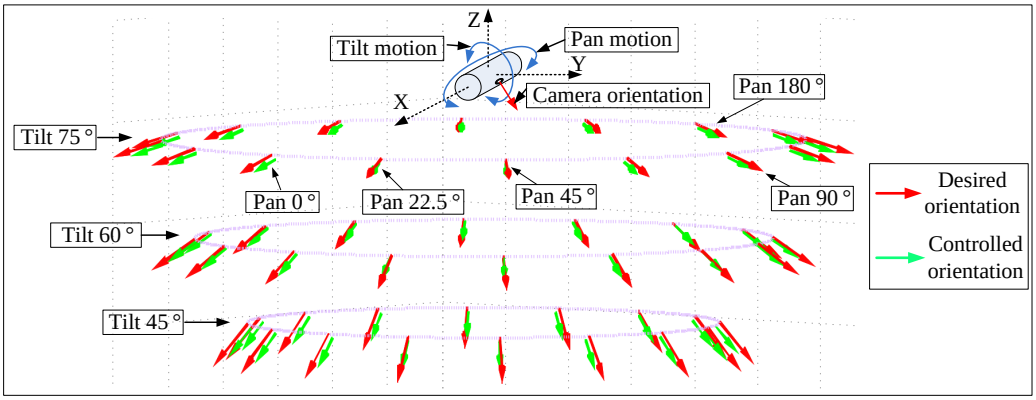

Figure 5.18: Pan and tilt motion control experiment.

Chapter 6

Conclusion and Future Work

This research aims at developing a magnetic actuated fully insertable robotic camera system to enhance procedures of single incision laparoscopic surgery. The design objective is to feature unified fixation, translation, and rotation functions for the camera actuation mechanism by controlling a externally generated magnetic field from a stator. Inspired by a spherical motor concept, a semi-spherical and a line-arranged driving units with pure coil stators were firstly developed and experimentally evaluated. Due to the coil heating problem and the requiring of unreliably complex control algorithm, a hybrid stator with the line-arranged driving unit was proposed as the final design based on the previous two generation prototypes. A closed-loop control system was developed on the final actuation mechanism design for achieving automatic orientation control of the camera. The actuation capabilities of the proposed design were thoroughly evaluated by experiments.

6.1 Conclusion

In the original prototype, a semi-spherical rotor/stator driving system for a wireless laparoscopic camera was proposed. To study reasonable stator and rotor patterns for providing sufficient actuation capabilities, three stator designs that consist of 3, 4, and 5 coils and four rotor designs were proposed. Experimental investigations indicate

that the 3 coils iron-core stator with 20 mm outer radius and the Rotor 1 show the best balance of reasonable dimension and sufficient force and torque for manipulating the camera. However, one major issue of this design is the usage of maximum 5 A current inputs for stable actuation, which results in coil overheating.

In the second prototype, a line-arranged rotor driving unit design was developed to address the problem arose from the original semi-spherical rotor/stator design. This second generation prototype applied a 17 flatly arranged coils as a stator to control the line-arranged rotor with three diametrically magnetized cylindrical magnets. Besides holding the functions of fixation and translation for the camera, the design enables a decoupled pan and tilt activation by controlling the input current of stator's coils. A simulation study was conducted that indicate under the current limit of 2.5 A, the system conservatively has the capability to achieve 360° pan motion with a 22.5° resolution, and the range of 127° $\sim$ 164° tilt motion which depends on tilt motion working modes and the distance between the rotor and the stator. However, a drawback of the second design is that according to the experimental study of the prototype, the current control of the 17 coils needs a complex algorithm, which resulted in unreliable camera motion control.

To design a practical actuation mechanism based on the second prototype, a hybrid stator that consists of three permanent magnets and two coils was developed for reliable camera motion control with a simple control algorithm. Experiment investigations indicated that the hybrid stator with the line-arranged rotor design can provide reliable anchoring, translation, 360° pan motion control, and up to 80° tilt motion control. The pan and tilt motions can be simultaneously controlled in a decoupled way. Therefore, this successful prototype was considered as the final design.

Grounded on the final design of the actuation mechanism, a closed-loop control system was developed for automatic control of the camera. The main components of the control system include the pan motion mechanism in the stator, the central EPM adjusting mechanism, the abdominal wall thickness sensing system, and

pan/tilt motion sensing system. The experimental results indicate that The camera orientation control can achieve 360° continuous pan motion with 0.49° control accuracy, and at least 75° tilt motion with 0.67° control accuracy. The combined orientation control in three-dimensional space demonstrated less than 1° control accuracy.

6.2 Future Work

This dissertation presents a promising magnetic actuated fully insertable surgical camera to help surgeons for improving procedures in single incision laparoscopic surgery. The innovative design features a unified and automatic actuation mechanism which can anchor, navigate, and rotate a laparoscopic camera wirelessly with a capsulated body. The experiment investigations demonstrate reliable, practical, and accurate control of the camera robot. To move a further step towards a real surgical instrument that can be commercialized, the future work includes:

1. Integration of on-board electronics in the dummy camera. There are four main components to be designed for the camera on-board electronics, which are a miniature camera and its illumination system, a battery and the battery management system, an inertial sensing system, and a wireless module. An auto-focus lens will be developed for the miniature imaging device to optimize surgical visualization. The inertial sensing system will provide camera motion feedback for the closed-loop motion control. The wireless module will be in charge of transmitting imaging data and motion feedback.

2. Dimension reduction and electronics integration of the stator. For a clinical application, a light and small size stator for the camera control is preferred. So in the future work, the stator dimension and weight will be further optimized. In the current stage, control commands to the stator for generating rotational magnetic field is transmitted through wires. In our future design, the stator

cables will be removed by integrating a wireless module, coil drivers, and batteries inside the stator.

3. Development of the camera delivery system. To insert the camera into an abdominal cavity and position the camera under the magnetic couping of the stator, a miniature flexible continuum manipulator that can be fitted in a standard trocar will be developed.

4. Development of autonomous surgical device tracking algorithm. During a surgical procedure, a laparoscopic camera has to be continuously adjusted by surgeons in order to achieve high quality visual feedback. In the future work, besides controlling the camera system by a user interface, a surgical device tracking algorithm will be developed that enables our robotic camera system to autonomously adjust the camera orientation and center the surgical instruments in the imaging feedback.

5. *Ex vivo* and *in vivo* tests. In the current stage, the camera system has been tested by simulated abdominal wall environments. To further investigate the actuation capabilities in real application scenarios, *ex vivo* and *in vivo* tests will be conducted by using porcine abdominal cavities.

Bibliography

Best, S., Kabbani, W., Scott, D., Bergs, R., Beardsley, H., Fernandez, R., Mashaud, L., and Cadeddu, J. (2011). Magnetic anchoring and guidance system instrumentation for laparo-endoscopic single-site surgery/natural orifice transluminal endoscopic surgery: lack of histologic damage after prolonged magnetic coupling across the abdominal wall. *Urology*, 77(1):243–7. 64

Cadeddu, J., Fernandez, R., Desai, M., Bergs, R., Tracy, C., Tang, S., Rao, P., Desai, M., and Scott, D. (2009). Novel magnetically guided intra-abdominal camera to facilitate laparoendoscopic single-site surgery: initial human experience. *Surg Endosc.*, 23(8):1894–9. 3

Carpi, F. and Pappone, C. (2009). Magnetic maneuvering of endoscopic capsules by means of a robotic navigation system. *Biomedical Engineering, IEEE Transactions on*, 56(5):1482–1490. xii, 5, 6

Castro, C., Smith, S., Alqassis, A., ketterl, T., Yu, S., Ross, S., Rosemurgy, A., Savage, P., and Gitlin, R. (2013). A wireless robot for networked laparoscopy. *Biomedical Engineering, IEEE Transactions on*, 60(4):930–936. xii, 3, 4

Chirikjian, G. and Stein, D. (1999). Kinematic design and commutation of a spherical stepper motor. *Mechatronics, IEEE/ASME Transactions on*, 4(4):342–353. 7

Ciuti, G., Valdastr, P., Menciassi, A., and Dario, P. (2010). Robotic magnetic steering and locomotion of capsule endoscope for diagnostic and surgical endoluminal procedures. *Robotica*, 28(2):199–207. xii, 5, 6

Cleary, K. and Peters, T. M. (2010). Image-guided interventions: technology review and clinical applications. *Annual Review of Biomedical Engineering*, 12:11942. 1

Desai, M., Berger, A., Brandina, R., Aron, M., Irwin, B., Canes, D., Desai, M., Rao, P., Sotelo, R., Stein, R., and Gill, I. (2009). Laparoendoscopic single-site surgery: Initial hundred patients. *Urology*, 74(4):805 – 812. 2

Fakhry, M., Gallagher, B., Bello, F., and Hanna, G. (2009). Visual exposure using single-handed magnet-driven intra-abdominal wireless camera in minimal access surgery: is better than 30 degrees endoscope. *Surg Endosc.*, 23(3):539–543. 3

Glass, P., Cheung, E., and Sitti, M. (2008). A legged anchoring mechanism for capsule endoscopes using micropatterned adhesives. *Biomedical Engineering, IEEE Transactions on*, 55(12):2759–2767. xii, 4, 5

Groom, N. (1997). Expanded equations for torque and force on a cylindrical permanent magnet core in a large-gap magnetic suspension system. 42

Hu, T., Allen, K., Hogle, J., and Fowler, L. (2009). Insertable surgical imaging device with pan, tilt, zoom, and lighting. *The International Journal of Robotics Research*, 28(10):1373–1386. xii, 3, 4

Hunter, S. (1961). The rolling contact of a rigid cylinder with a viscoelastic half space. *Journal of Applied Mechanics*, 28(4):611–617. 46, 52

Jackson, J. D. (1999). *Classical electrodynamics*. Wiley, New York, NY. 21, 40, 67

Kim, B., Lee, S., Park, J. H., and Park, J.-O. (2005a). Design and fabrication of a locomotive mechanism for capsule-type endoscopes using shape memory alloys (smas). *Mechatronics, IEEE/ASME Transactions on*, 10(1):77–86. xii, 4, 5

Kim, B., Park, S., Jee, C. Y., and Yoon, S.-J. (2005b). An earthworm-like locomotive mechanism for capsule endoscopes. In *Intelligent Robots and Systems, 2005. (IROS 2005). 2005 IEEE/RSJ International Conference on*, pages 2997–3002. xii, 4, 5

Kim, S. H. and Ishiyama, K. (2014). Magnetic robot and manipulation for active-locomotion with targeted drug release. *Mechatronics, IEEE/ASME Transactions on*, 19(5):1651–1659. 6

Kok-Meng, L. and Hungsun, S. (2007). Distributed multipole model for design of permanent-magnet-based actuators. *Magnetics, IEEE Transactions on*, 43(10):3904–3913. 70, 91

Kummer, M., Abbott, J., Kratochvil, B., Borer, R., Sengul, A., and Nelson, B. J. (2010). Octomag: An electromagnetic system for 5-dof wireless micromanipulation. *Robotics, IEEE Transactions on*, 26(6):1006–1017. 6, 22, 41, 72

Liang, Y., I-Ming, C., Guilin, Y., and Kok-Meng, L. (2006). Analytical and experimental investigation on the magnetic field and torque of a permanent magnet spherical actuator. *Mechatronics, IEEE/ASME Transactions on*, 11(4):409–419. 7, 20, 39

Lim, C. K., Yan, L., Chen, I.-M., Yang, G., and Lin, W. (2004). Mechanical design numerical electromagnetic analysis of a dc spherical actuator. In *Robotics, Automation and Mechatronics, 2004 IEEE Conference on*, volume 1, pages 536–541 vol.1. 7

Liu, X., Mancini, G., and Tan, J. (2014a). Design of a unified active locomotion mechanism for a capsule-shaped laparoscopic camera system. In *Robotics and Automation (ICRA), 2014 IEEE International Conference on*, pages 2449–2456. 64

Liu, X., Mancini, G. J., and Tan, J. (2014b). Design of a unified active locomotion mechanism for a wireless laparoscopic camera system. In *Intelligent Robots and Systems (IROS), 2014 IEEE/RSJ International Conference on*, pages 1294–1301. 64, 70, 91, 92

Liu, X., Mancini, G. J., and Tan, J. (2015). Design and analysis of a magnetic actuated capsule camera robot for single incision laparoscopic surgery. In *Intelligent Robots and Systems (IROS), 2015 IEEE/RSJ International Conference on*. 89, 98, 104

Loring, S., Brown, R., Gouldstone, A., and Butler, J. (2005). Lubrication regimes in mesothelial sliding. *Journal of Biomechanics*, 38(12):2390–6. 46

Moglia, A., Menciassi, A., Dario, P., and Cuschieri, A. (2009). Capsule endoscopy: progress update and challenges ahead. *Nat. Rev. Gastroenterol. Hepatol.*, 6(1):353–362. 2, 44

Navarra, G., Malfa, G. L., Lazzara, S., Ullo, G., and Curro, G. (2010). Sils and notes cholecystectomy: a tailored approach. *Journal of Laparoendoscopic and Advanced Surgical Techniques*, 20:511514. 2

Nelson, B. J., Kaliakatsos, I., and Abbott, J. (2010). Microrobots for minimally invasive medicine. *Annu Rev Biomed Eng.*, 12:55–85. 2

Platt, S., Hawks, J., and Rentschler, M. (2009). Vision and task assistance using modular wireless in vivo surgical robots. *Biomedical Engineering, IEEE Transactions on*, 56(6):1700 –1710. xii, 3, 8

Rossini, L., Chetelat, O., Onillon, E., and Perriard, Y. (2011). Analytical and experimental investigation on the force and torque of a reaction sphere for satellite attitude control. In *Advanced Intelligent Mechatronics (AIM), 2011 IEEE/ASME International Conference on*, pages 487–492. 7

Rossini, L., Chetelat, O., Onillon, E., and Perriard, Y. (2013). Force and torque analytical models of a reaction sphere actuator based on spherical harmonic rotation and decomposition. *Mechatronics, IEEE/ASME Transactions on*, 18(3):1006–1018. 20, 39

Saidy, M., Tessier, M., and Tessier, D. (2012a). Single-incision laparoscopic surger–hype or reality: A historical control study. *Perm J.*, 16(1):47–50. 2

Saidy, M. N., Tessier, M., and Tessier., D. (2012b). Single-incision laparoscopic surgery hype or reality: A historical control study. *The Permanente Journal*, 16:4750. 2

Sendoh, M., Ishiyama, K., and Arai, K.-I. (2003). Fabrication of magnetic actuator for use in a capsule endoscope. *Magnetics, IEEE Transactions on*, 39(5):3232–3234. xii, 5, 6

Silvestri, M., Ranzani, T., Argiolas, A., Vatteroni, M., and Menciassi, A. (2013). A multi-point of view 3d camera system for minimally invasive surgery. *Sensors and Actuators A: Physical*, 202(0):204 – 210. 3

Simi, M., Sardi, G., Valdastri, P., Menciassi, A., and Dario, P. (2011). Magnetic levitation camera robot for endoscopic surgery. In *Robotics and Automation (ICRA), 2011 IEEE International Conference on*, pages 5279–5284. xii, 3, 8

Simi, M., Silvestri, M., Cavallotti, C., Vatteroni, M., Valdastri, P., Menciassi, A., and Dario, P. (2013). Magnetically activated stereoscopic vision system for laparoendoscopic single-site surgery. *Mechatronics, IEEE/ASME Transactions on*, 18(3):1140–1151. xii, 3, 8

Song, C., Alijani, A., Frank, T., Hanna, G., and Cuschieri, A. (2006). Mechanical properties of the human abdominal wall measured in vivo during insufflation for laparoscopic surgery. *Surgical Endoscopy And Other Interventional Techniques*, 20(6):987–990. 9, 17, 61, 77, 110, 111

Swain, P., Austin, R., Bally, K., and Trusty, R. (2010). Development and testing of a tethered, independent camera for notes and single-site laparoscopic procedures. *Surg Endosc.*, 24(8):2013–21. 3

Toennies, J., Simi, M., Valdastri, P., and Webster, R. (2010). Swallowable medical devices for diagnosis and surgery: The state of the art. *J. Mech. Eng. Sci*, 224(7):1397–1414. 2

Tortora, G., Valdastri, P., Susilo, E., Menciassi, A., Dario, P., Rieber, F., and Schurr, M. (2009). Propeller-based wireless device for active capsular endoscopy in the gastric district. *Minim. Invasive Therapy Allied Technol.*, 18:280290. xii, 5

Tracy, C., Raman, J., Cadeddu, J. A., and Rane, A. (2008). Laparoendoscopic single-site surgery in urology: where have we been and where are we heading? *Nat Clin Pract Urol.*, 5(10):561–568. 2

Uehara, A. and Hoshina., K. (2003). Capsule endoscope norika system. *Minim Invasive Ther Allied Technol.*, 12(5):227–34. xii, 5, 6

Valdastri, P., Quaglia, C., Buselli, E., Arezzo, A., Lorenzo, N. D., Morino, M., Menciassi, A., and Dario, P. (2010). A magnetic internal mechanism for precise orientation of the camera in wireless endoluminal applications. *Endoscopy*, 42(6):481–6. 8

Valdastri, P., Webster, R., Quaglia, C., Quirini, M., Menciassi, A., and Dario, P. (2009). A new mechanism for mesoscale legged locomotion in compliant tubular environments. *Robotics, IEEE Transactions on*, 25(5):1047–1057. xii, 4, 5

Wang, W., Wang, J., Jewell, G., and Howe, D. (2003). Design and control of a novel spherical permanent magnet actuator with three degrees of freedom. *Mechatronics, IEEE/ASME Transactions on*, 8(4):457–468. 20, 39

Wang, X. and Meng, M. (2006). Dipole modeling of magnetic marker for capsule endoscope localization. In *The 6th World Congress on Intelligent Control and Automation*, volume 2, pages 5382–5386. 23

Wang, X., Sliker, L., Qi, H., and Rentschler, M. (2013). A quasi-static model of wheel–tissue interaction for surgical robotics. *Medical Engineering and Physics*, 35(9):1368 – 1376. 52

Yim, S. and Sitti, M. (2012). Design and rolling locomotion of a magnetically actuated soft capsule endoscope. *Robotics, IEEE Transactions on*, 28(1):183–194. xii, 5, 6

Zabulis, X., Sfakiotakis, M., and Tsakiris, D. (2008). Effects of vibratory actuation on endoscopic capsule vision. In *Engineering in Medicine and Biology Society, 2008.*

EMBS 2008. 30th Annual International Conference of the IEEE, pages 5901–5904. xii, 5

Vita

Xiaolong Liu was born in Shenyang, Liaoning, China in 1985. He received a Bachelor's degree in Electrical Engineering and a Master's degree in Computer Engineering from Northeastern University in Shenyang, China in 2008 and 2010 respectively. In the year 2010, he was admitted in a PhD program advised by Prof. Jindong Tan in Michigan Technological University in Houghton, MI, USA. He worked as a graduate teaching assistant in the Department of Electrical and Computer Engineering from 2010 to 2012. He transferred to the University of Tennessee, Knoxville in September 2012 and continued his research with Prof. Tan. He graduated with a Doctor of Philosophy degree in Biomedical Engineering in August 2015.